I. Excluded Volume Effects in Ising Cluster Distributions and Nuclear Multifragmentation
II. Multiple-Chance Effects in α-Particle Evaporation

by

Dimitry Eugene Breus

Engineer (Moscow Institute of Chemical Technology) 1994

A dissertation submitted in partial satisfaction of the
requirements for the degree of
Doctor of Philosophy

in

Engineering-Nuclear Engineering

in the

GRADUATE DIVISION
of the
UNIVERSITY of CALIFORNIA at BERKELEY

Committee in charge:

Professor Stenley G. Prussin, Chair
Professor Luciano G. Moretto
Professor Jasmina L. Vujic

Spring 2005

The dissertation of Dimitry Eugene Breus is approved:

Chair Date

Date

Date

University of California at Berkeley

Spring 2005

Abstract

I. Excluded Volume Effects in Ising Cluster Distributions and Nuclear Multifragmentation

II. Multiple-Chance Effects in α-Particle Evaporation

by

Dimitry Eugene Breus

Doctor of Philosophy in Engineering-Nuclear Engineering

University of California at Berkeley

Professor Stenley G. Prussin, Chair

In Part I, geometric clusters of the Ising model are studied as possible model clusters for nuclear multifragmentation. These clusters may not be considered as non-interacting (ideal gas) due to excluded volume effect which predominantly is the artifact of the cluster's finite size. Interaction significantly complicates the use of clusters in the analysis of thermodynamic systems. Stillinger's theory is used as a basis for the analysis, which within the RFL (Reiss, Frisch, Lebowitz) fluid-of-spheres approximation produces a prediction for cluster concentrations well obeyed by geometric clusters of the Ising model. If thermodynamic condition of phase coexistence is met, these concentrations can be incorporated into a differential equation procedure of moderate complexity to elucidate the liquid-vapor phase diagram of the system with cluster interaction included. The drawback of increased complexity is outweighted by the reward of greater accuracy of the phase diagram, as it is demonstrated by the Ising model.

A novel nuclear-cluster analysis procedure is developed by modifying Fisher's model to contain cluster interaction and employing the differential equation procedure to obtain thermodynamic variables. With this procedure applied to geometric clusters, the guidelines are developed to look for excluded volume effect in nuclear multifragmentation.

In Part II, an explanation is offered for the recently observed oscillations in the energy spectra of α-particles emitted from hot compound nuclei. Contrary to what was previously expected, the oscillations are assumed to be caused by the multiple-chance nature of α-evaporation. In a semi-empirical fashion this assumption is successfully confirmed by a technique of two-spectra decomposition which treats experimental α-spectra as having contributions from at least two independent emitters.

Building upon the success of the multiple-chance explanation of the oscillations, Moretto's single-chance evaporation theory is augmented to include multiple-chance emission and tested on experimental data to yield positive results.

Professor Stenley G. Prussin
Dissertation Committee Chair

To my family.

Contents

List of Figures

List of Tables

Acknowledgements

This work is a result of many wonderful circumstances that unexpectedly came together and provided an opportunity of which I would never dream of. Certainly, the role of several people who mentored me was key in achieving the goal, which now is embodied in the volume of this writing.

I want to thank Professor Stanley Prussin, for being my campus adviser over the years and agreeing to be the chair of my thesis committee.

I would like to express my profound thankfulness to Professor Darlene Hoffman who graciously invited me to come to Berkeley and provided me with support and guidance so much needed in the early days of my scientific carrier. Even though I was not well advanced in my linguistic and scientific achievements, she did not give up on me and gave me two chances to stay with her group and enter graduate studies at UC Berkeley.

I am greatly indebted to Professor Luciano Moretto. He took me, an inexperienced young man, to his group and offered mentorship and leadership of the highest grade to guide my graduate research. His way of scientific reasoning shaped my thinking when approaching complex tasks. His determination to persevere when facing difficulties inspired me to persist and not to give up when solving the puzzles in my studies. I specifically want to mention the good hope, which he had toward me that I would not fail but succeed. And though I experienced many negative results and stubbornly dwelled on errors, he patiently corrected me, even when my research

went against his opinion, wisely steering me in a right direction. Thank you, Luciano.

I owe special thanks to Dr. Gordon Wozniak, for his support, hospitality and being my LBNL supervisor. His thoroughness, patience, and expertise set a high standard of research quality, which I want to follow in my carrier. I also appreciate the financial support, provided through Moretto/Wozniak group, that facilitated my study in engineering.

My special thanks go to Dr. Larry Phair. For many years of my graduate school he never failed to help on practical everyday routine issues. Whenever I needed an advice on data analysis, computer coding or experiment setup, I went to Larry. I really appreciate his courteousness and patience when I needed explanation of simple things over and over again. He always took time and made an effort.

Last but not least, I want to thank Dr. Jim Elliott for his participation in making this work become a reality. Many hours of fruitful discussion provided an enormous help in putting together the first part of this thesis. Jim's expertise with Fisher's model was especially valuable. I also want to mention Jim's kindness toward me. Whenever I experienced a difficult situation, whether preparing a challenging talk or getting ready for an exam, he has never been indifferent and tried to help as much as he could.

This work was supported by the Director, Office of the Energy Research, Office of High Energy and Nuclear Physics, of the US Department of Energy under Contract No. DE-AC03-76SF00098.

Part I

Excluded Volume Effects in Ising Cluster Distributions and Nuclear Multifragmentation

Chapter 1

Introduction

1.1 Historical Background of the Research

Initiated by the Becquerel's discovery of radioactivity in 1896, the first quarter of the twentieth century featured a series of important findings that showed the existence of the atomic nucleus and its complex structure and behavior. In 1911 Rutherford demonstrated in his famous α-particle scattering experiment that the atom (he used gold) has a small massive dense charged nucleus, that contained the major part of the atomic mass. In 1913 Bohr confirmed these experimental findings, introducing his quantized planetary atomic model, which accurately described the electronic levels in the hydrogen atom. Moseley determined the nuclear charge in 1914, and the same year Rutherford suggested that the nucleus of hydrogen was the fundamental positively charged particle, which he called proton. Later in 1917

Rutherford proved the existence of protons in the nucleus by bombarding nitrogen with α-particles and observing the protons coming out. This was also the first observation of a nuclear reaction. Around the same time Rutherford conjectured the existence of a neutral particle in the nucleus, which was similar to the proton. However, it was not until the 1932 discovery of the neutron by Chadwick that the proton-neutron nuclear model was developed by Heisenberg. Still it was not clear how protons and neutrons (collectively called nucleons) were bound together in the nucleus. Accurate measurements of the proton mass as well as the masses of many nuclei using the methods of mass spectrometry provided the clue. Since the neutron and proton masses were known, it was possible to determine the difference between the mass of the bound nucleus and the total mass of the individual nucleons that formed the nucleus. First of all, it was found that the mass difference (also called the mass defect) was relatively large, almost 1% of the nuclear mass. According to Einstein's mass-energy relation such a mass difference corresponds to a large amount of energy needed to break the nucleus apart into individual nucleons. Secondly, it was also found that the nuclear binding energy divided by the number of nucleons in the nucleus (also called the binding energy per nucleon) did not change much from nucleus to nucleus, and fluctuated around the constant value of 8 MeV. This observation was equivalent to the nuclear binding energies varying approximately linearly with the number of nucleons in the nucleus (the nuclear mass number), and revealed the short-range nature of the nuclear interaction.

Another experimental confirmation of the short-range nature of the nuclear forces came through the measurement of nuclear radii. By 1934 it was already understood that the change of the nuclear radius r with the nuclear size obeyed the cubic root dependence

$$r = r_0 A^{1/3}, \tag{1.1}$$

where $r_0 = 1.2 \times 10^{-13}$ cm was a constant. This dependence was indicative of the constant nuclear density calculated as the ratio of the nuclear mass number A and the volume $4/3\pi r^3$.

These two properties of constant density and constant binding energy per particle are the manifestation of saturating of nuclear forces, characteristic of ordinary liquids, whose molecules also exhibit a short-range interaction.

The short-range force causes a particle in a system to experience interaction only with its nearest neighbors, the number of which is limited by the geometry of close packing. When a particle is completely surrounded by its nearest neighbors, its interaction is said to be saturated, since the second nearest neighbors are already blocked from approaching the particle close enough to interact. Therefore the total binding in the bulk of the liquid B_v grows linearly with the amount of the liquid, and so it is proportional to the volume v of the liquid:

$$B_v \propto v. \tag{1.2}$$

A finite amount of liquid, like a drop, possesses an outer boundary or a surface. The surface molecules are not completely surrounded by nearest neighbors, and do not experience complete binding. As a result, the total binding energy in the drop is less than expected on the basis of bulk binding energy. The reduction in binding energy B_s is proportional to the number of molecules in the surface layer, which in turn is proportional to the surface area s of the drop:

$$B_s \propto s. \tag{1.3}$$

If a drop of liquid is charged, its binding energy decreases even more since the charges repel each other and destabilize the drop. This reduction in binding energy B_C, goes quadratically with the total charge Z on the drop and is inversely proportional to the radius of the drop r_D. The exact calculation for a uniformly charged sphere yields

$$B_C = \frac{3}{5}\frac{Z^2}{r_D}. \tag{1.4}$$

Thus a nucleus may be thought of as a drop of charged liquid obeying the requirements of binding in classical charged fluids. This idea was formally employed by Weizsacker in 1935, when he introduced a semi-empirical formula for the nuclear binding energy B using the analogy with a spherical drop of charged liquid:

$$B = a_v A - a_s A^{2/3} - a_C \frac{Z^2}{A^{1/3}} - a_{sym} \frac{(A-2Z)^2}{A} + \delta, \tag{1.5}$$

where $A^{2/3}$ follows from the relation of the surface of a sphere to its volume, $A^{1/3}$ follows from the relation of the radius of a sphere to its volume, and a_v, a_s, a_C, a_{sym} are proportionality coefficients to be determined experimentally. In addition to

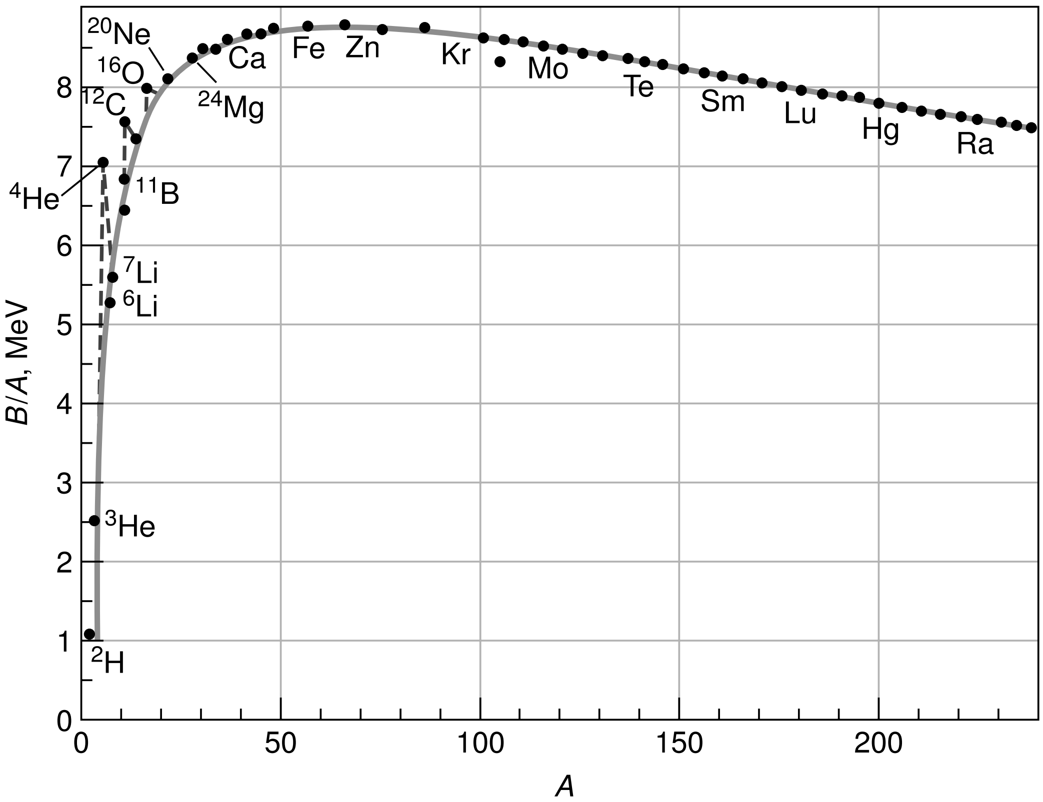

Figure 1.1: Success of the liquid drop model. The solid circles are the experimental data for the stable isotopes. The solid line is the liquid drop model fit. Binding energies are per nucleon.

the classical terms the formula contains two more quantum terms for symmetry and pairing energies. The symmetry term reflects the tendency of nuclei to have equal number of neutrons and protons, and the pairing energy δ arises as a result of like nucleons of opposite spin assuming a lower energy state if they combine to form a pair.

The liquid drop formula, apart from the quantum terms, is a general characteristic feature displayed by finite condensed systems with short-range interaction. Such systems are called leptodermous (thin-skinned) due to the presence of a thin outer layer whose properties alter the properties of the whole system in comparison with the infinite bulk behavior. Each geometric attribute of the finiteness, like volume, surface or curvature, individually contributes to a system's extensive property. For example, the binding energy of the particles in the system can be presented as an expansion in powers of $A^{-1/3}$:

$$B = A(c_1 + c_2 A^{-1/3} + c_3 [A^{-1/3}]^2 + \ldots), \tag{1.6}$$

where A is the system's size (or mass number, which is proportional to the volume of the system), and c_1, c_2, … are energy coefficients. This series is generally referred to as the liquid drop expansion. As seen from Equation 1.6, finite size effects in leptodermous systems become small as A tends to infinity, and the binding becomes proportional to the size A.

The nuclear liquid drop model turned out to be very successful in describing binding energies of atomic nuclei (see Figure 1.1). The average deviation for all the known isotopes is only about 1%. Still there are fluctuations, especially in the region of small masses and for special numbers (magic) of neutrons and protons. These fluctuations are the manifestation of the shell effects in the nucleus, which arise due to quantization of nucleon energies, and their degeneracies. Inside each group (shell) nucleons have similar energies, whereas the energy gaps between the shells are of the order of the shell thickness (difference between the maximum and minimum energies in the shell). As a result, binding energies are also affected by these peculiarities causing fluctuations depicted in Figure 1.1.

Nevertheless, the fluctuations are small, and the nuclei exhibit an almost 99%-smooth liquid-like behavior. This important conclusion means that the study of nuclei may be greatly simplified by considering them as drops of uniform liquid-like matter. In this approach the individual behavior of nucleons in the nucleus becomes irrelevant. What matters are their collective properties in the nucleus as a whole.

1.2 Nuclear Thermodynamics and Phase Transition

The description of the ground-state nuclei in terms of a liquid drop led to several important conclusions. First of all, it became clear that the Equation 1.5 describes finite charged drops of some bulk nuclear matter. The volume term $a_v A$ of the liquid drop expansion, if taken alone, gives the bulk binding energy of the infinite matter, uncharged and symmetric in the sense that the masses of protons and neutrons are equal. This matter possesses some global properties that manifest the nature of the "pure" nuclear binding, undisturbed by Coulomb and quantum effects. Since the matter is infinite, one is naturally led to study its properties thermodynamically using such macroscopic variables as pressure and temperature.

Secondly, a thermodynamic study of infinite nuclear matter is a way to condense the knowledge of its physics into a concise description. Then all the variety of nuclei and nuclear processes may be understood by extrapolation of the properties of the infinite system to the properties of finite charged drops, like individual nuclei. This point can be illustrated using a simple example. Suppose we can only observe tiny charged droplets of water. The properties of water in the droplets depend on the size and charge of the droplets. However, if we know the general properties of the bulk infinite water, we can always predict the properties of each of the small drops using the liquid drop expansion.

Thirdly, nuclear matter may have phases. Depending on the temperature and pressure, thermodynamic systems generally can form different phases. A phase of a system is a homogeneous part of the system that is separated from other parts by a distinct boundary. Phases can transform into each other depending on the state of the system. This transformation is called phase transition. Since nuclei display a liquid-like behavior in their ground state, corresponding to zero temperature, there is the expectation of a nuclear vapor phase at higher temperatures.

The simplest model of liquids in classical thermodynamics is represented by the Van der Waals theory, which describes the properties of fluids encompassing liquid and gas phases. According to this theory, these fluids are composed of particles having a non-zero size and a pairwise attractive force which quickly drops to a negligible value as the interparticle separation increases. It was proposed by Van der Waals in 1873 as a modification to the ideal gas law. This theory describes the behavior of real fluids. In particular, it exhibits a first-order phase transition between a liquid phase and a gas phase, as well as criticality.

First-order phase transitions occur at pressure, temperature and chemical potential common to the two phases involved in the transition. Only the amounts of the phases change, causing the specific volume (volume per unit mass) of the system to undergo a modification, which occurs primarily due to the formation of gas. If the specific volume of the system is intermediate between those of pure phases, the phases are said to be in coexistence. Since thermodynamic states of individual phases are not affected by each other's presence, phase coexistence does not require the contact of the phases.

Van der Waals theory also predicts criticality as a characteristic property of the equilibrium liquid-gas systems. Above a certain temperature, called critical temperature, the Van der Waals fluid cannot exist in the form of a liquid irrespective of the applied pressure. Therefore, liquid and gas cannot coexist above this temperature, and only gas is present in the system. The transformation from the mixed-phase region to the gas-only region, that happens at the critical point, is called second-order phase transition.

The order of the transition has to do with a discontinuity in a derivative of the fluid's free energy with respect to an intensive thermodynamic variable that controls the transition (like temperature). In the liquid-vapor transition the first derivative is discontinuous, at the critical point discontinuity appears in the second derivative.

Nuclear matter is expected to manifest the properties of a Van der Waals fluid.

A nuclear gas phase has been conjectured in the evaporation-like process of decay of excited nuclei, which may be thought of as a hot liquid. Excitation can be imparted to a ground-state nucleus, for example, by colliding it with a nucleon. If the nucleon or another projectile nucleus used for collision unites with the target nucleus, and the collision energy gets evenly distributed over all the internal degrees of freedom (thermalization), a compound nucleus is formed. Irrespective of the way energy gets transferred to a nucleus, the resulting hot nucleus emits protons, neutrons and composite fragments. Protons and light composites, like deuterons, tritons and α-particles, are called light charged particles (LCP). The composites of larger mass, like the isotopes of lithium and heavier fragments, are collectively called intermediate mass fragments (IMFs). The emission of single nucleons, LCPs and IMFs from a hot nucleus suggests the occurrence of the nuclear liquid-vapor phase coexistence, which is identified following the analogy of nuclear and Van der Waals fluids.

However, the thermodynamic condition of phase equilibrium is not clear in nuclear evaporation. First of all, it is not guaranteed that thermalization occurs before fragment emission. Secondly, the nuclear vapor phase does not stay around the nucleus, leading to time dependent cooling of the drop.

1.3 Nuclear Kinetics and Phase Transition

Kinetic considerations are useful in clarifying the equilibrium condition of nuclear evaporation. The rate of drop evaporation is the number of particles (or fragments) per unit volume dn lost by the drop on the average per unit time dt. It is controlled by the liquid drop's average bulk binding energy B and the temperature T of the liquid. If the drop is thermalized, evaporation rates at different temperatures follow the Arrhenius law:

$$Rate = \frac{dn}{dt} = C(T)\exp\left(-\frac{B}{RT}\right), \tag{1.7}$$

where $C(T)$ is a preexponential, which may depend on the temperature, and R is the gas constant. A typical Arrhenius plot looks like a straight line in the ln($Rate$)-1/T coordinates.

With a fully thermalized liquid drop, the phase equilibrium can always be defined by the initial rate of emission from the drop just after it is allowed to evaporate. This interesting fact circumvents the problem of the missing vapor phase in nuclear evaporation. The first vapor particle emitted out of the drop (nucleus) after evaporation begins defines the rate of emission at an equilibrium state of the liquid at some initial temperature. Since at equilibrium there has to be an equal flow of particles from the gas back into the liquid, it is always possible to define a corresponding equilibrium state of the gas around the drop with the relation

$$Rate = \frac{dn}{dt} = n(T)\nu\sigma, \tag{1.8}$$

where here $n(T)$ is the particle (or fragment) concentration in the gas, ν is the particle's (or fragment's) average velocity, and σ is the inverse cross section, characterizing the emission of a particle (or a fragment) from the nuclear interface. Since the condition of phase coexistence does not require the phases to be in contact, the vapor phase does not have to be present, and can be referred to as a "virtual vapor" [More 04]. Of course, the particles coming second can no longer characterize the same equilibrium state, since the temperature of the liquid changes. Therefore, only the first nucleons or fragments emitted from the excited nucleus after its formation, called the first chance emission, can uniquely characterize nuclear equilibrium liquid-vapor coexistence. If these nucleons and fragments are found to obey the Arrhenius law, with proper analysis techniques coexistence thermodynamics may be experimentally extracted and summarized in a phase diagram.

1.4 Phase Diagrams

The nuclear liquid-vapor phase diagram defines the regions of pure phases in the thermodynamic P-v-T-space, and is a goal of experimental nuclear thermodynamics, quite within the reach of modern detector technology and skillful analysis techniques. In fact, the construction of a first nuclear liquid-vapor phase diagram has already been reported by one research group [Elli 02, Elli 03]. When finally accomplished, the experimental phase diagram will provide a reliable check for the much more involved nuclear equation-of-state studies.

Usually a phase diagram is displayed using its projections onto the coordinate planes, like the T-v and P-T projections of water phase diagram shown in Figure 1.2.

In the $T - v$ projection the heavy-bell-shaped curve envelopes the two-phase

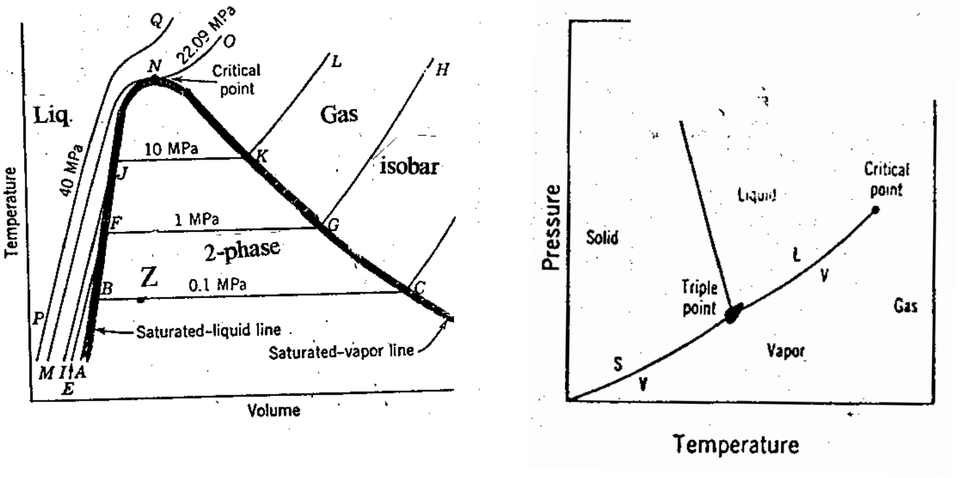

Figure 1.2: Various projections of a phase diagram of water.

liquid-vapor region. To the left of this zone is the compressed-liquid single-phase region, and to the right of the envelope is the superheated vapor region. The left-hand and the right-hand boundaries of the two-state envelope correspond to the states of the saturated liquid and the saturated vapor, respectively. The maximum of the envelope is the critical point, beyond which there is no distinction between liquid and vapor. Several isobars are also shown in the figure.

The $P-T$ projection appears simpler than the $T-v$ diagram since the two-phase envelope is looked at on edge, and so is collapsed onto a curved line. The line labeled L/V gives the temperature dependence of the vapor pressure of the liquid at the liquid-vapor coexistence.

Direct macroscopic measurements of nuclear pressure and specific volume to build diagrams, like those in Figure 1.2, is not a feasible task, since nuclear matter is not available in large bulk quantities. Nevertheless, experimental determination of the nuclear liquid-vapor phase diagram is possible indirectly with a method that employs vapor clusters.

1.5 The Cluster Method in Nuclear Thermodynamics

Vapor clusters are groups of individual vapor atoms or molecules bound together by the short-range attraction. They express the tendency of a non-ideal gas to condense and form liquid. In fact, clusters may be thought of as tiny drops of liquid, that preform in vapor prior to condensation. Far from condensation the formation of clusters is inhibited due to higher vapor pressure of the drops in comparison with the pressure of gas. Any cluster that occasionally forms quickly evaporates. On the opposite, reverse conditions favor the formation of clusters when the gas pressure becomes comparable to the vapor pressure of little clusters. In this case, larger clusters actually have lower vapor pressure, that promotes their further growth. Therefore, every state of a gas is characterized by a temperature and density dependent distribution of clusters according to the number of particles in them, also called cluster size. Away from condensation in the thermodynamic P-v-T space of a gas the distribution is largely dominated by monomers, whereas at condensation clusters of macroscopic size become more probable. The onset of condensation is marked by an intermediate distribution still dominated by monomers, but having significant fraction of other clusters as well.

Clusters may be defined in a variety of ways depending on the distribution of energy over the internal degrees of freedom of a group of particles. Different cluster definitions produce different size distributions for the same state of vapor. Therefore, cluster definition is necessary to determine the state of the system that produced the observed distribution. Since it is a difficult task to distinguish clusters by internal degrees of freedom, usually the internal degrees of freedom are not considered in a hope that they do not contribute very much. Instead, clusters of simple definitions are used, taking into account but a few degrees of freedom, like the aforementioned cluster size and the number of particles that face the outside of the cluster (reminiscent of cluster surface). Such restriction leads to the introduction of the so-called configurational clusters. Once a definition of a cluster is settled upon, the analysis of a thermodynamic system can be carried through with the construction of a cluster theory expressing a formal link between the local properties of vapor, reflected in clusters, and the global properties of vapor, like the pressure P and density ρ (the inverse specific volume $1/v$). Different cluster definitions generally require different cluster theories, though for a particular cluster definition a cluster theory may be developed exactly. The main problem of a cluster theory, however, is matching theoretical cluster distributions with those experimentally observed.

In nuclear physics clusters can be observed directly and counted. They are the nuclear fragments, including single nucleons as a particular case, that are emitted from the hot nucleus. Therefore, a thermodynamic state of nuclear matter may be determined from the experimental cluster size distribution using the mediatory role of a cluster theory. The problem of cluster definition, however, introduces an element of uncertainty in any calculation of this sort.

1.6 Clusters and Cluster Theories

Cluster theories are developed using the machinery of statistical mechanics to calculate the partition function of a fluid [Path 86, Huan 87].

A Van der Waals fluid can be thought of as composed of N structureless particles of mass m, interacting through a short-range two-body potential $u(r_{ij})$, where r_{ij} is the distance between particles i and j. The Hamiltonian of the fluid is the sum of kinetic and interaction energies of the particles:

$$\mathscr{H}(\{\mathbf{r}_i\},\{\mathbf{p}_i\}) = \sum_{i=1}^{N} \frac{\mathbf{p}_i^2}{2m} + \sum_{i<j} u(r_{ij}), \tag{1.9}$$

where $\mathbf{r}_i$ and $\mathbf{p}_i$ are the position and momentum coordinates of the ith particle, $r_{ij} = |\mathbf{r}_i - \mathbf{r}_j|$, and the second sum is over all the particle pairs. In the canonical ensemble, for a given volume V and temperature T, the partition function of the fluid is given by

$$Q_N(T,V) = \frac{1}{N!h^{3N}} \int\limits_{\{\mathbf{r}_i\},\{\mathbf{p}_i\}} \exp(-\beta\mathscr{H}(\{\mathbf{r}_i\},\{\mathbf{p}_i\}))d\mathbf{r}_1\ldots d\mathbf{r}_N d\mathbf{p}_1\ldots d\mathbf{p}_N, \tag{1.10}$$

where $\beta = 1/T$, h is Planck's constant, and the integration runs over the coordinate and momentum space of every particle within V. Integrations over the momentum coordinates can be carried out analytically to yield

$$Q_N(T,V) = \frac{1}{N!\lambda^{3N}} Z_N(T,V), \tag{1.11}$$

where

$$\lambda = \frac{h}{\sqrt{2\pi m T}} \tag{1.12}$$

is the thermal wavelength of a particle, that expresses the reciprocal of the particle's kinetic contribution to the fluid's partition function, and

$$Z_N(T,V) = \int\limits_V \prod_{i<j} \exp(-\beta u(r_{ij})) d\mathbf{r}_1 \ldots d\mathbf{r}_N \tag{1.13}$$

is the configurational integral of the partition function due to the pair potential interaction. If the fluid in V is free to exchange particles with an outside reservoir at a given chemical potential μ per particle, the relative probability of having N particles in V is $Q_N z^N$, where $z = \exp(\beta\mu)$ is a particle's fugacity. The grand partition function for such a system is

$$\mathscr{L}(z,T,V) = \sum_{N \geq 0} z^N Q_N(T,V) \tag{1.14}$$

From the grand partition function, the thermodynamics of the fluid can be computed in a standard way with the following relations:

$$\begin{aligned} \beta P &= \frac{1}{V} \ln \mathscr{L}(z,T,V) \\ \rho = \frac{1}{v} &= \frac{\partial}{\partial \ln z} \frac{1}{V} \ln \mathscr{L}(z,T,V), \end{aligned} \tag{1.15}$$

from which the equation of state may be derived.

Clusters can be introduced into the description of the fluid by rewriting the fluid's grand partition function in terms of individual cluster partition functions. This can be done assuming various degrees of approximation.

1.6.1 Non-interacting Clusters

The simplest approximate way to express the partition function of a fluid through clusters is to assume their independence. Clusters of given size a (number of particles) are characterized by the cluster partition function $q_a(T,V)$, that reflects all the cluster's internal properties, and by a chemical potential $\mu_a = a\mu$, that shows the change in the system's free energy due to the introduction of the cluster. The partition function of the fluid is then factorizable in terms of cluster partition functions [Sato 03]:

$$\mathscr{L}(z,T,V) = \prod_{a=1}^{\infty} \exp(q_a(T,V)z^a) \tag{1.16}$$

This assumption is called the ideal-cluster-gas approximation, in which clusters are assumed to behave like an ideal gas. It can be demonstrated [Sato 03] that within the ideal-cluster-gas approximation the pressure P, the density ρ, and the cluster concentration n_a of the system of the volume V are given by

$$\begin{aligned} \beta P &= \frac{1}{V}\sum_{a=1}^{\infty} q_a z^a, \\ \rho &= \frac{1}{V}\sum_{a=1}^{\infty} a q_a z^a, \end{aligned}$$

$$n_a(\beta, z) = \frac{1}{V} q_a z^a \tag{1.17}$$

Eliminating z between the pressure and density equations leads to the equation of state of the system, which is completely defined by the q_a values. An important consequence of the theory is that the equation of state of a system can be expressed through sums over the cluster concentrations n_a:

$$\begin{aligned} \beta P &= \sum_{a=1}^{\infty} n_a \\ \rho &= \sum_{a=1}^{\infty} a n_a \end{aligned} \tag{1.18}$$

This result is valuable from the standpoint of nuclear physics as it completely bypasses the problem of cluster definition. Experimental cluster distributions n_a can directly yield the thermodynamics within the ideal-cluster-gas approximation.

Since the definition of a cluster as a drop of liquid, also called physical cluster, can mean many things and is not precise, it is not possible to calculate the partition function q_a without specifying the definition of a physical cluster. Such specification leads to ideal-cluster-gas models, that can yield analytic results. The most prominent of them are due to Bijl [Bijl 38], Band [Band 39], Frenkel [Fren 39] (BBF) (who, in fact, introduced the notion of the physical cluster) and Fisher [Fish 67].

1.6.1.1 BBF Model

In 1938-1939 Bijl, Band and Frenkel independently introduced physical clusters, in which they disregarded the internal degrees of freedom of a cluster. In addition to that, the clusters were assumed to be compact, characterized by their size a and surface s. Therefore, the potential energy of the cluster was written as the sum of the bulk and the surface terms:

$$E_{cl} = -e_a a + e_s a^{2/3}, \tag{1.19}$$

where the term with $a^{2/3}$ follows from the relation of the surface of the sphere to its volume, and e_a and e_s are the bulk and surface energy coefficients, respectively.

Since the clusters were assumed to be compact with a shape closest to the spherical (not exactly spherical since they were made up of spherical particles), no surface entropy of the clusters was taken into account. The partition function was derived by integrating the position and momentum coordinates of the center of mass of the cluster over the phase space of the system:

$$q_a = \frac{V}{\lambda^3} a^{3/2} \exp(\beta[e_a a - e_s a^{2/3}]), \tag{1.20}$$

where $\lambda/\sqrt{a}$ is the thermal wavelength of a cluster of size a. The concentration of clusters of size a follows from the partition function according to Equations 1.17:

$$n_a = \frac{q_a z^a}{V} = \frac{a^{3/2}}{\lambda^3} \exp(\beta[e_a a - e_s a^{2/3}]) z^a = \frac{a^{3/2}}{\lambda^3} y^a x^{a^{2/3}}, \tag{1.21}$$

where $y = z \exp(\beta e_a)$ and $x = \exp(-\beta e_s)$.

The function y depends on the temperature and density (through z). The function x is independent of the density and is always less than unity. For a given temperature T, x is fixed, and the cluster size distribution n_a depends on density only through y.

When $y < 1$, n_a decreases exponentially with increasing a: there is no macroscopic cluster, which corresponds to the gas phase. For $y > 1$, n_a increases exponentially with increasing cluster size: a macroscopic cluster appears, indicating the formation of the liquid phase. At the moment when condensation sets in (coexistence) $y = y_{cond} = 1$ so that $\mu_{cond} = -e_a$, where *cond* stands for condensation. Therefore, at coexistence the energy of the cluster formation depends only on the cluster surface, and

$$n_a^{coex} = \frac{a^{3/2}}{\lambda^3} \exp(-\beta e_s a^{2/3}) \tag{1.22}$$

The BBF model was the first phenomenological model that introduced a clear and intuitive interpretation of condensation with physical clusters and gave analytic results, since the sums in Equation 1.17 can be evaluated at any μ and T. However, this model did not allow one to locate the critical point, and was bound to fail at high densities, since the real clusters cannot be regarded as point particles in close-packing configurations of the system.

1.6.1.2 Fisher's Droplet Model

Another very successful cluster model was introduced by Fisher in 1967. As the BBF model, Fisher's droplet model is based on the ideal gas of clusters approximation. However, Fisher writes the partition function of the clusters of size a with the help of additional features. He allows for the entropy of the clusters. Clusters are not assumed to be compact. A drop may deviate from the spherical shape and deform.

Deformation is associated with the cluster's surface entropy due to the fact that a drop of the same volume may possess many possible shapes.

The mean energy and entropy of a Fisher's droplet of size a, with a mean surface s, are written as a sum of the surface and bulk terms:

$$\begin{aligned} E_{cl} &= -e_a a + e_s s \\ S_{cl} &= s'_a a + s'_s s, \end{aligned} \tag{1.23}$$

where e_a and s'_a are the volume energy and entropy coefficients, respectively, and e_s and s'_s are the surface energy and entropy coefficients.

Since the clusters are not compact, Fisher introduces the parameter σ to relate the surface and volume of a cluster:

$$s = a_0 a^{\sigma}, \tag{1.24}$$

where a_0 is a constant. For a perfect sphere $\sigma = 2/3$, for a string $\sigma = 1$, for an average cluster surface σ should be somewhere in between.

Instead of the cluster potential energy, like in BBF model, Fisher writes the free energy of the cluster of size a as

$$\beta F_{cl} = -\beta(e_a + s'_a T)a + \beta a_0(e_s - s'_s T)a^{\sigma} + \tau \ln a - \ln q_0 V, \tag{1.25}$$

in which he introduces an additional correction to the cluster free energy:

$$\beta \Delta F_{cl} = \tau \ln a - \ln q_0 V \tag{1.26}$$

The term $\tau \ln a$ comes from the topological considerations of surfaces that close on themselves with τ being a characteristic constant. The term proportional to $\ln V$ is the result of the integration over the position of the cluster's center of mass (translational motion), in which q_0 is a constant, so that the thermal wavelengths are assumed weakly dependent on the temperature and buried in q_0.

The cluster partition function is

$$q_a = \exp(-\beta F_{cl}) = q_0 V a^{-\tau} \exp(\beta(e_a + s'_a T)a - \beta a_0(e_s - s'_s T)a^{\sigma}), \tag{1.27}$$

from which the pressure, density and cluster concentrations can be inferred using Equations 1.17 if T, μ, and the model-specific constants are known.

In the spirit of BBF model, the cluster concentration can be written as

$$n_a = q_0 a^{-\tau} y^a x^{a^{\sigma}}, \tag{1.28}$$

where $y = z\exp(\beta[e_a + s'_a T])$ and $x = \exp(-\beta a_0[e_s - s'_s T])$. The condensation begins with the appearance of a macroscopic cluster. According to the value of x, two cases are possible. If $x < 1$, as in BBF model, the condensation point (coexistence) is given by $y_{cond} = 1$, so that $\mu_{cond} = -[e_a + s'_a T]$. On the other hand, if $x \geq 1$ the cluster size distribution n_a exponentially increases when $y > 1$ leading to divergence of the pressure and density series in Equations 1.17. Therefore, condensation only happens when $x < 1$, that is for $T < T_c = e_s/s'_s$. This upper limit on the condensation temperature is interpreted as the critical temperature, and Fisher's model is not valid above T_c.

Like in BBF model, at coexistence formation of Fisher's droplets is controlled by their surface energy only. As a result the cluster concentrations simplify:

$$n_a = q_0 a^{-\tau} \exp(-\beta a_0 (e_s - s_s' T) a^\sigma) = q_0 a^{-\tau} \exp(-\beta c_0 \epsilon a^\sigma), \qquad (1.29)$$

where $c_0 = a_0 e_s$, and $\epsilon = 1 - T/T_c$ is a convenient measure of how far away from the critical temperature the system is located.

Fisher's model is a remarkable model. Being simple, it captures all the properties of a Van der Waals vapor. The unknown parameters can be readily determined from a thermodynamic experiment with a real vapor. As a result, a complete description of a system can be obtained using Equations 1.17. In spite of many approximations that enter the model, it possesses much flexibility to hide inconsistencies in the parameters without loss of the general physical-cluster picture. Nevertheless, the complete disregarding of cluster interaction may render the model inaccurate when evaluating thermodynamic variables at high fluid densities, especially in the vicinity of the critical point.

1.6.2 Interacting Clusters

All the ideal-cluster-gas models are fundamentally flawed. Notwithstanding the simplicity, usefulness and clear physical intuition that these models display, they are bound to be imprecise or even wrong under certain conditions, like at the critical point or other high density regimes. The ideal-cluster-gas theory appeals to unrealistic approximations, like the non-interaction of clusters and their point-particle-like behavior, that is never true at close packing. For example, at condensation macroscopic clusters may appear. In the words of Stillinger [Stil 63], since "such large aggregates use up much of the available vessel volume, leaving considerably less for others, it is clear that only by taking cluster noninterpenetration into account can a proper theory of phase transitions be constructed". Unlike the weak attraction that the particles in a Van der Waals fluid exert on each other, the repulsion due to finite volume is very strong. The need to account for the effects of repulsion and attraction between clusters led to the developing of interacting cluster theory in the 1950s. Until then only Band attempted to introduce finite volume effects into his model [Band 39].

If clusters are assumed interacting, their precise definition is important before a theory can be built. In the theories presented below clusters are defined as groups of particles obeying certain geometric rules. Only configurational clusters were studied this way, *i.e.* no internal degrees of freedom of clusters were taken into consideration, thereby restricting the cluster interaction to the effects of noninterpenetration and weak attraction tails of the pair potentials.

Two major cluster theories emerged as a result of this approach: the theory by Lee, Barker and Abraham (LBA) [LBA 73], and Stillinger's theory [Stil 63, Stil 67] with follow-ups [Gill 77]. Their development was inspired by the pioneer work of Reiss, Frisch and Lebowitz (RFL) [RFL 59, RFHL 60, Helf 61, Lebo 65] on the fluid of spheres, who first attempted to systematically address the issues of finite particle volume in thermodynamic systems.

1.6.2.1 RFL Theory

RFL developed their theory without the direct reference to the concept of clusters and methods of statistical mechanics. They considered a mixture of spheres of various diameters numbered from 1 to m with number densities (concentrations) $n_1 \ldots n_m$ characterized by the temperature T. The spheres do not exhibit any attraction and interact only through mutual volume exclusion. Since the spheres in the mixture have finite volume, putting in a new sphere requires some work in order to make enough space for it, which is due to the change in the configurational part of the system's free energy (entropic term). In other words, when a new sphere is inserted, it has to push other spheres aside creating a cavity and causing a change in the free energy of the fluid. RFL calculate the cavity work $W(D, n_1 \ldots n_m, D_1 \ldots D_m)$ of inserting the sphere of diameter D into the m-component mixture by assuming that for all values $D > 0$ the work can be approximated by a cubic polynomial:

$$W = T\Delta S = W_0 + \left.\frac{\partial W}{\partial D}\right|_{D=0} D + \frac{1}{2}\left.\frac{\partial^2 W}{\partial D^2}\right|_{D=0} D^2 + \frac{\pi}{6} D^3 P, \tag{1.30}$$

where W_0 is the work of inserting a point (volumeless) sphere, P is the pressure, and ΔS is the change in the fluid's entropy. This approximation was prompted by the cavity formation work in the two extreme cases of inserting a no volume and a large volume spheres. If a point sphere with $D = 0$ is put in, counter to our intuition, the change in the fluid's free energy is not zero. Even though no cavity is formed, the point sphere restricts the available space for other spheres, since their centers cannot approach the point sphere closer than their radii. In other words, the point sphere cannot exist inside of other spheres in the mixture. Using integral-equation techniques, RFL formally calculate that

$$W_0 = -T \ln \left[1 - \sum_{i=1}^{m} \frac{\pi}{6} D_i^3 n_i \right], \;\; D = 0 \tag{1.31}$$

Since n_i are number densities, *i.e* numbers per unit volume, and $\pi/6D_i^3$ are sphere volumes, the sum represents the total fractional volume which is occupied and is not available to the point sphere. A Boltzmann factor of W_0, namely $\exp(-\beta W_0)$, yields the reduction in probability to observe a point sphere in the container due to finite volume of other spheres.

On the other hand, inserting a very large sphere in the mixture requires the work $P\Delta V$, where ΔV is just the volume of the sphere $\pi/6D^3$. Therefore, the cubic polynomial in Equation 1.30 represents the asymptotic cases plus contributions at intermediate diameters due to the surface and curvature of the sphere expressed as a Taylor expansion up to the second order.

RFL were able to derive all the coefficients in Equation 1.30 and to build the equation of state of the fluid of spheres. They demonstrated the magnitude of the finite volume effects in fluids and introduced [1] the notion of cavity formation, that

---

[1] The basic principles of cavity formation have been known for a long time. They come from general statistical mechanical considerations that if W is the reversible work required for the creation of a cavity of an arbitrary shape, then the probability of observing a fluctuation in which such a cavity forms is given by the Boltzmann factor $\exp(-\beta W)$ [Tolm 38]. However, RFL were the first to apply this notion to account for the excluded volume effects in fluids.

is central to the understanding of the cluster interaction.

1.6.2.2 Stillinger's Theory

Stillinger was the first to rigorously apply the idea of cavity-formation in fluid to physical clusters within the framework of statistical mechanics. Inspired by the work of RFL, he considered BBF clusters as a starting point of his theory neglecting the internal degrees of freedom of the clusters. However, unlike BBF clusters, Stillinger's clusters were exactly defined as configurational groups of particles separated by distances not exceeding a characteristic distance D, defined as a minimum of the pair potential $u(r)$, where r is the interparticle distance (see the left panel of Figure 1.3). If a sphere of radius D is drawn around each particle in a snapshot of the system (see the right panel of Figure 1.3), then only particles with intersecting spheres may form clusters. Otherwise single particles remain unclustered. Such configurational cluster definition allowed Stillinger to improve upon BBF definition eliminating the condition of compactness. Clusters of any shape and surface could form, effectively introducing the surface entropy.

Cavity formation in Stillinger's theory plays the central role. Like for RFL spheres, the appearance of a cluster in the midst of other clusters requires making a space for it, which costs an extra amount of free energy. This free energy is due to the change in the configurational part of the fluid's free energy. Thus forming a cluster in the fluid requires some free energy to put the particles together plus an

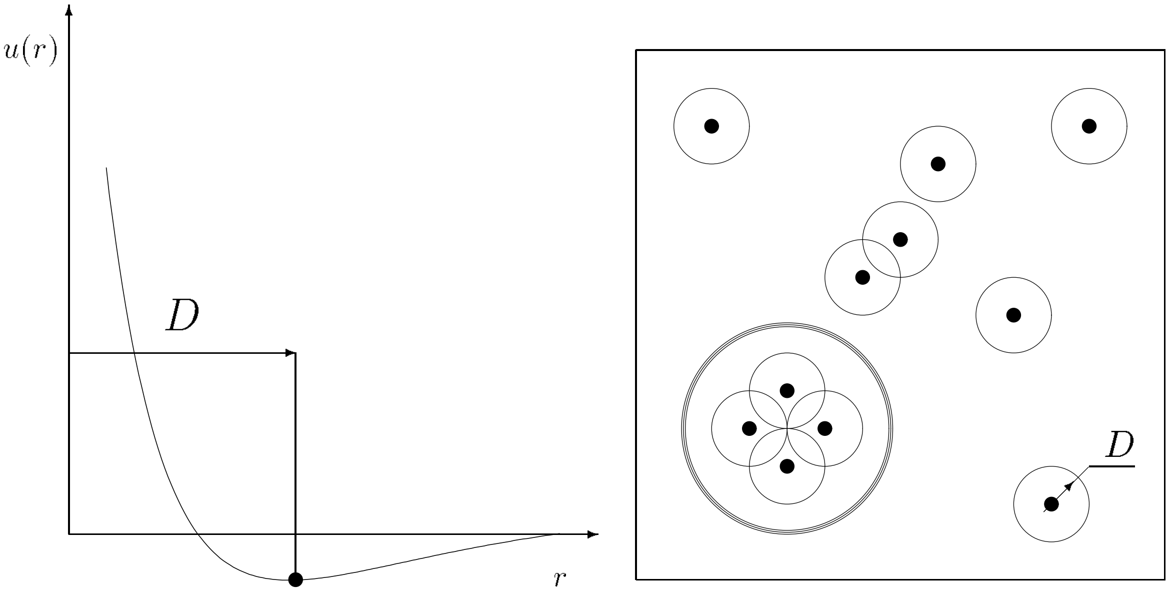

Figure 1.3: Left panel: a schematic of the interparticle pair potential. Right panel: definition of Stillinger's clusters. The large circle visualizes the concept of the cavity.

extra free energy to insert the new cluster in the medium of other clusters pushing them aside. For this reason, clusters interact primarily due to their geometry. The exact mechanics of the interaction, which Stillinger dubbed "geometrical interference", may be viewed loosely as a requirement that two clusters, say of size s and t, not approach too near lest they be counted erroneously as a single cluster of size $s+t$. Therefore every cluster has to have a "protective" shell or cavity around it in order to avoid loosing its identity. See how this idea is illustrated in Figure 1.3). The large circle separates the area around the cluster of size four, which is not accessible by the single particles, unless the cluster of size five is formed. This cavity restricts the configurational space of other clusters in the system, damping their abundances and effectively repelling the particles.

The same cavity can also attract particles due to the tails of pair potentials, a much weaker effect then repulsion.

To describe cluster interference quantitatively, Stillinger rigorously introduced the notion of the cavity formation free energy. A system, like in Figure 1.3, can be characterized by a grand partition function $\exp(-\beta\Omega)$, where the negative grand potential $-\Omega$ can be identified as the pressure of the system P times its volume V: $-\Omega = PV$. If now a cluster of size a and some fixed shape is placed in a fixed position in the container (like the cluster of size four in Figure 1.3), it creates an impenetrable cavity around it that is not accessible by other particles in the volume. The grand partition function of particles in the container excluding the cavity with the fixed cluster is $\exp(-\beta\Omega_a[\mathbf{r}])$, where $\Omega_a[\mathbf{r}]$ again is the grand potential of the system with the excluded cavity, and $\mathbf{r}$ stands for radius-vectors of the particles in the cluster which determine the exact location and shape of the cluster. Stillinger introduced the quantity $p_a[\mathbf{r}]$ to be equal to the probability that the a particles of the same cluster (serially numbered and regarded as distinguishable) simultaneously occupy the fixed cavity volume (cluster formation probability). He rigorously demonstrated that this cluster formation probability can be expressed in terms of the partition functions $\exp(-\beta\Omega)$ and $\exp(-\beta\Omega_a[\mathbf{r}])$ as follows:

$$p_a[\mathbf{r}] = p_a^0 \exp(-\beta[\Omega_a[\mathbf{r}] - \Omega]), \tag{1.32}$$

where p_a^0 is the probability of forming the cluster in an empty container that does not have any other particles except those forming the cluster (ideal cluster gas), and the difference $\Omega_a[\mathbf{r}] - \Omega = W_a[\mathbf{r}]$ is the reversible isothermal work required to create the cavity around the cluster of size a.

Owing to the probability character of $p_a[\mathbf{r}]$, this function may be integrated over all positions inside the container volume V to give $N_a(z)$, the average number of clusters of size a:

$$N_a(z) = \int\limits_V p_a[\mathbf{r}]\mathbf{dr} = q'_a(z)z^a, \tag{1.33}$$

where the cluster partition function $q'_a(z)$ is now fugacity dependent due to the fugacity dependence of $W_a[\mathbf{r}]$, which can be rewritten as $W_a[\mathbf{r}, z]$:

$$q'_a(z) = q_a \int\limits_V \exp(-\beta W_a[\mathbf{r}, z])\mathbf{dr} \tag{1.34}$$

Then the density is

$$\rho(z) = \frac{1}{V}\sum_{a=1}^{\infty} a q'_a(z) z^a = \sum_{a=1}^{\infty} a n_a(z), \tag{1.35}$$

where $n_a(z)$ is the concentration of clusters of size a. The pressure P of the whole system may be obtained integrating Equation 1.35 with respect to z at constant β:

$$\beta P = \int\limits_z \rho(z) d\ln z, \tag{1.36}$$

which requires explicit knowledge of $W_a[\mathbf{r}, z]$. Altogether, the pressure and density equations can be written similarly to Equations 1.17 of the ideal-cluster-gas approximation:

$$\begin{aligned} \rho &= \frac{1}{V}\sum_{a=1}^{\infty} a q_a z^a \int\limits_V \exp(-\beta W_a[\mathbf{r}, z])\mathbf{dr} \\ \beta P &= \frac{1}{V}\sum_{a=1}^{\infty} q_a z^a \int\limits_V \frac{a}{z^a} \int\limits_z (z')^{a-1} \exp(-\beta W_a[\mathbf{r}, z'])dz'\mathbf{dr} \end{aligned}$$

$$n_a = \frac{1}{V} q_a z^a \int\limits_V \exp(-\beta W_a[\mathbf{r}, z])\mathbf{dr}, \tag{1.37}$$

from which the equation of state could be found by eliminating z, if it were possible. Unlike the ideal-cluster-gas approximation, additional complex position and fugacity dependent manipulations appear due to cluster interaction.

Stillinger derived a Mayer cluster expansion [2] for the quantities $W_a[\mathbf{r}, z]$ and explicitly demonstrated their dependence on the global thermodynamic variables of pressure and density. Schematically this expression can be written as follows:

$$\beta W_a[\mathbf{r}, z] = \beta P v_a + f[\mathbf{r}, \rho] \tag{1.38}$$

where v_a is the volume of a cavity around the cluster of size a, and f is a position and cluster size dependent function of density ρ. Equation 1.38 demonstrates that the pressure and density contributions to $W_a[\mathbf{r}, z]$ are always separable, and that only the density contribution is position dependent. Since $W_a[\mathbf{r}, z]$ depends on the global system properties, equilibrium cluster abundances in fluid are not independent, like in the ideal cluster gas. The pressure and density can no longer be found through simple summations in Equations 1.17, but rather require a search for a self-consistent solution of Equations 1.37.

---

[2] Mayer's clusters and expansions employing them were first introduced by Mayer in 1937 [Maye 40]. These clusters have nothing to do with physical clusters in fluids, and should rather be called graphs that constitute a convenient mathematical abstraction that allows expression of the fluid's partition function as an infinite sum of independent components. Mayer's N-particle graphs are exactly defined as collections of N distinct circles numbered $1, 2, 3, \ldots, N$, with any number of lines joining the same number of distinct pairs of circles. Thus every circle in a graph is attached to at least one line, and every circle is joined directly or indirectly to all other circles in the graph.

1.6.2.3 LBA Theory

LBA presented a formal theory of physical clusters which accounted for both intercluster forces and geometrical interference. Their formal theory is exact for any reasonable definition of configurational physical cluster, like Stillinger's cluster. As an example in their work they adopted a definition of physical cluster, introduced by Reiss, Katz, and Cohen [Reis 68, Reis 70], which requires that each member molecule lie within a spherical volume of prescribed radius R_a whose center is the center of mass of the group of a particles.

LBA used their theory only for Monte Carlo studies of individual clusters. They did not attempt to calculate the equation of state of the fluid, as Stillinger did. Therefore, LBA theory is not fitting as a tool for thermodynamic analysis of a system through clusters. Rather it explores properties of individual clusters as they change with temperature and definition.

The main reason for mentioning LBA theory here is due to the important conclusion that they arrived at studying various configurational cluster definitions. They found that a cluster's free energy is almost independent of its definition provided that the definition is reasonable and the temperature is sufficiently low. Using this conclusion, LBA stressed that Stillinger's theory, being a complete theory for a particular type of physical clusters, would be approximately valid for any cluster definition.

This conclusion is very important for the research presented in this thesis, since nuclear clusters are not exactly defined. On the basis of LBA work, one may hope that nuclear cluster distributions possess signatures of geometric interference which can be identified within the scope of Stillinger's theory.

1.7 Building a Nuclear Phase Diagram Using Clusters

In macroscopic systems, like water or argon, the use of cluster theories as a means to build a phase diagram is not of primary importance, since other more direct techniques can be used. Cluster models, like Fisher's model, are rather of theoretical value and are employed to explore and identify the formation of clusters in real fluids using thermodynamic data obtained elsewhere.

In nuclear physics the situation is reversed, since clusters can be readily detected, but no direct measurement of nuclear vapor pressure is feasible. Here cluster models become handy as mediators providing recipes to analyze experimental nuclear fragment abundances and to draw conclusions about the state of the system that produced these fragments.

It has been found experimentally that the first-chance emission yields of nuclear fragments obey the Arrhenius law [More 97, Elli 02]. First-chance fragment yields are obtained event by event from hot nuclei in nuclear evaporation experiments. Yields are rates multiplied by the characteristic time of emission, and are proportional to concentrations through Equation 1.8. Figure 1.4 demonstrates an example of

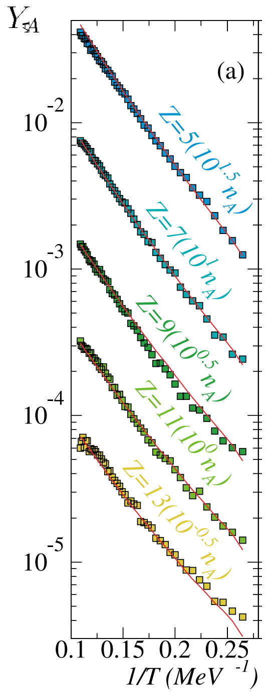

Figure 1.4: Experimental yields of nuclear fragments from the reaction of 8 GeV/c π on gold. Lines represent fits with Fisher's model.

yields per nucleon of the parent nucleus Y_A for several nuclear fragments at various temperatures using the $\ln Y_A$-$1/T$-coordinates [Elli 02]. Clearly, the plots are very linear. On the basis of the initial rate picture, linearity of the first-chance nuclear Arrhenius plots experimentally validates the thermodynamic approach to the analysis of nuclear evaporation. First-chance nuclear fragment yields bear direct experimental information about the equilibrium liquid-vapor coexistence of nuclear matter.

The simplest way to build a liquid-vapor phase diagram from clusters is to use the ideal-gas-of-clusters approximation at coexistence. This approximation disregards the problem of detailed cluster definition, and can be applied to nuclear clusters directly if they are assumed not to interact. Looking at Equations 1.18, it becomes clear that the pressure and density can easily be obtained by summing the concentrations and size-weighted concentrations of clusters, respectively. However, in the case of nuclear clusters there are complications that require additional manipulations to disentangle relevant and non-relevant contributions to the cluster yields.

Nuclear cluster distributions suffer from the effects of Coulomb interaction. When a compound nucleus readies itself to emit a fragment, the formation free energy of the fragment is not only due to its surface but also to the Coulomb interaction between the fragment and the residual nucleus, as well as to the Coulomb self-energy of the fragments. In fact, Coulomb interaction is ruinous to the whole picture of equilibrium phase transition. More detailed discussion on this subject will be presented later in this chapter. For now it is important to realize that the goal of nuclear thermodynamics is the study of uncharged matter, undisturbed by Coulomb effects. To this end, complete removal of Coulomb interaction from the picture can remedy the problem and lead to the achievement of the goal. Therefore, nuclear cluster distributions need to be adjusted accordingly by dividing out the part of the free energy which is due to the Coulomb interaction. Since the behavior of the Coulomb force is well known analytically, this procedure presents no fundamental difficulty. "Filtered" cluster distributions can be summed up using appropriate relations for P and ρ to obtain the phase diagram [More 03].

The ideal-cluster-gas-based phase diagram could have been obtained just using Equations 1.18, if it were not for the fact that experimental fragment distributions are incomplete. They are incomplete in terms of the cluster size and in terms of the temperature. Insufficiency of temperature points is not a fundamental problem. It can be solved by improving upon the experimental techniques. The insufficiency of cluster sizes in a data set, however, presents an insurmountable restriction. The rate picture, described earlier in the text, cannot be applied to single nucleons and light charged particles for the reason of multiple chance emission. Unlike heavy fragments, nucleons and LCPs have a high probability to be emitted from the residual nucleus after the emission of the primary fragment, as well as from the primary fragment itself before it reaches a detector. As a result, nucleon and LCP distributions represent a mixture of the system's states, among which only one state is equilibrium (first-chance) at the initial temperature, while others are due to lower temperatures. Heavy fragments, on the other hand, are mostly emitted first-chance. Their multiple-chance probabilities are extremely low, so that their effects on the fragment's distributions are less then statistical error of the experiment itself. Therefore, use of Equations 1.18 is frustrated owing to the loss of the most important contribution from the light fragments.

To overcome the insufficiency of data, missing light-fragment distributions have to be reconstructed. To achieve this reconstruction, however, detailed knowledge of the fragment's free energy is a must. Such knowledge can be obtained from a model. Fisher's droplet model has been recognized as the most elaborate and elegant among cluster models. It also allows simple estimation of the critical temperature. To

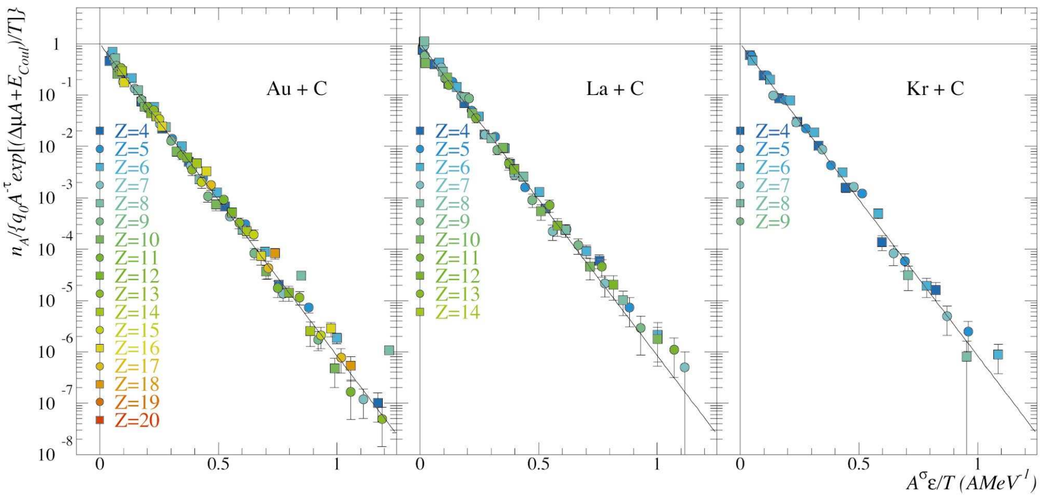

Figure 1.5: Application of Fisher's model to nuclear fragment distributions.

employ Fisher's model, experimental fragment distributions must be fitted with the coexistence expression using Equation 1.29 to determine unknown model parameters for the system. In addition corrections should be included to filter out the Coulomb effects. Uniqueness of the Fisher's parameters for the whole system can be achieved by fitting all the available distributions simultaneously [Elli 05]. Therefore, the overall technique should consist of using the expression

$$n_a = q_0 a^{-\tau} \exp(-\beta c_0 \epsilon a^{\sigma}) \exp(-\beta \Delta F_{Coul}) \tag{1.39}$$

to find the best set of Fisher's parameters, which simultaneously minimize the residual sum of all the available experimental distributions. The Coulomb free energy correction ΔF_{Coul} can be estimated analytically:

$$\Delta F_{Coul} = F^{Res}_{Coul.-Self} + F^{Frag}_{Coul.-Self} + F^{Frag.-Res.}_{Coul} - F^{Comp}_{Coul.-Self}, \tag{1.40}$$

where $F^{Comp}_{Coul.-Self}$ is the initial compound-nucleus Coulomb self-energy, $F^{Res}_{Coul.-Self}$ is the final residual-nucleus Coulomb self-energy, $F^{Frag}_{Coul.-Self}$ is the fragment Coulomb self-energy, and $F^{Frag.-Res.}_{Coul}$ is the fragment-residual Coulomb interaction energy. The self-energy contributions can be estimated assuming sphericity. To calculate the interaction energy contribution the touching-spheres approximation can be used [More 03].

If the system obeys the conditions of the Fisher's model (short-range interaction, thermal emission, fragment independence, distinctiveness of the liquid and vapor phases), the minimization converges, and the scaled fragment distributions should collapse on the same line, as shown in Figure 1.5 for the fragment yields in three different experiments [Elli 03]. This collapse of the scaled distributions is the characteristic feature of the model's applicability.

The liquid-vapor phase diagram is obtained using Equations 1.18 with Fisher's expressions for the concentrations:

$$\begin{aligned} \beta P &= \sum_{a=1}^{\infty} q_0 a^{-\tau} \exp(-\beta c_0 \epsilon a^{\sigma}) \\ \rho &= \sum_{a=1}^{\infty} a q_0 a^{-\tau} \exp(-\beta c_0 \epsilon a^{\sigma}), \end{aligned} \tag{1.41}$$

where the model parameters are those extracted from the fit. It should be noticed, however, that the Coulomb correction has been removed from consideration when calculating the coexistence thermodynamic variables thereby guaranteeing the validity of the obtained phase diagram for the uncharged nuclear matter.

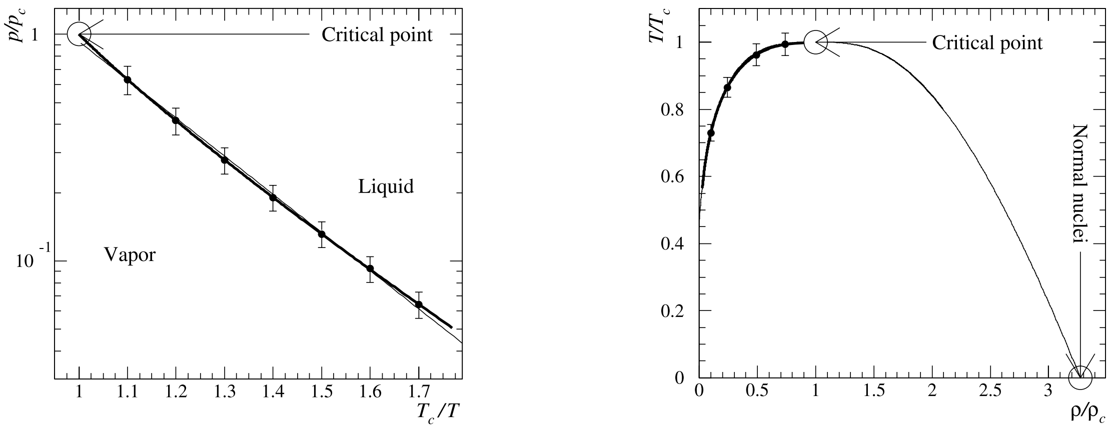

Figure 1.6: (Left panel): The reduced pressure-temperature phase diagram: the thick line shows the calculated co-existence line, the points show selected calculated errors, and the thin line shows a fit to the Clausius-Clapeyron equation. (Right panel): The reduced temperature-density phase diagram: the thick line is the calculated low density branch of the co-existence curve, the points are selected calculated errors, and the thin lines are a fit to and reflection of Guggenheim's equation.

The procedure outlined above has been used by Elliott *et al.* [Elli 02] to construct the first estimation of the nuclear liquid-vapor phase diagram. They used nuclear fragment distributions from the Indiana Silicone Sphere (ISiS) experiment to yield the results shown in Figure 1.6. The projections are presented in reduced form, so that the pressure, density and temperature are divided by their critical values. Only the gas part of the phase diagram is directly extractable from the experiment. The $P-T$ projection does not suffer from this restriction, since the vapor and liquid branches coincide. Using the integral form of Clapeyron-Clausius equation for an ideal gas

$$\frac{P}{P_c} = \exp\left[\frac{\Delta H_{vap}}{T_c}\left(1 - \frac{T_c}{T}\right)\right], \tag{1.42}$$

nuclear heat of vaporization ΔH_{vap} has been evaluated from this projection.

The bell-like $T-\rho$ projection can only be completed using additional information about the liquid branch. Such additional information comes from Guggenheim's equation [Gugg 45, Gugg 93]

$$\frac{\rho_{liq.,vap.}}{\rho_c} = 1 + b_1\left(1-\frac{T}{T_c}\right) \pm b_2\left(1-\frac{T}{T_c}\right)^{\beta} \tag{1.43}$$

where b_1 and b_2 are empirical parameters, and β here represents a parameter, which within Fisher's model can be calculated as

$$\beta = \frac{\tau - 2}{\sigma} \tag{1.44}$$

Using the Guggenheim equation to fit the vapor branch of the phase diagram, the liquid branch has been obtained by changing sign in front of b_2 as shown in Figure 1.6.

More complex cluster techniques involving interacting-cluster theories have never been employed to build a nuclear phase diagram. Therefore, it remains to be seen if such techniques can effectively be used to augment the existing Fisher's formalism. This thesis will make an attempt to shed some light on the issue and to introduce a technique that accounts for cluster interference according to Stillinger's and RFL methodology with some modifications specific to coexistence.

1.8 Applicability of Equilibrium Thermodynamics to Nuclear Evaporation

There are several criticisms of the attempt to use equilibrium thermodynamics as a tool in nuclear physics.

First of all, there is a doubt that a hot-nucleus liquid has enough time to reach thermal equilibrium before it emits the first gas fragment. If liquid itself is not in the state of thermal equilibrium, the first vapor fragment does not point to the equilibrated liquid-vapor coexistence, and the whole thermodynamic picture is lost. Formation of a hot nucleus happens in a dynamic process of collision between the nucleus and a projectile particle. The collision may be strong enough that prompt nucleons are knocked out. Clearly, dynamics should play an important part in this process, hardly leaving any place for static equilibrium.

There is no absolute answer to this criticism at the present time. The important clue comes from the timing of the emission. Prompt fragments, which come out shortly after the moment of collision and are mostly single nucleons and LCPs, are not taken into consideration. On the other hand, IMFs are very rare to appear as prompt. They are mostly emitted later after the process of thermalization when the initial energy of collision is equally distributed over all the internal degrees of freedom. There is no absolute guarantee that IMFs are emitted from a completely thermalized nucleus. However, there is much experimental evidence that this is so

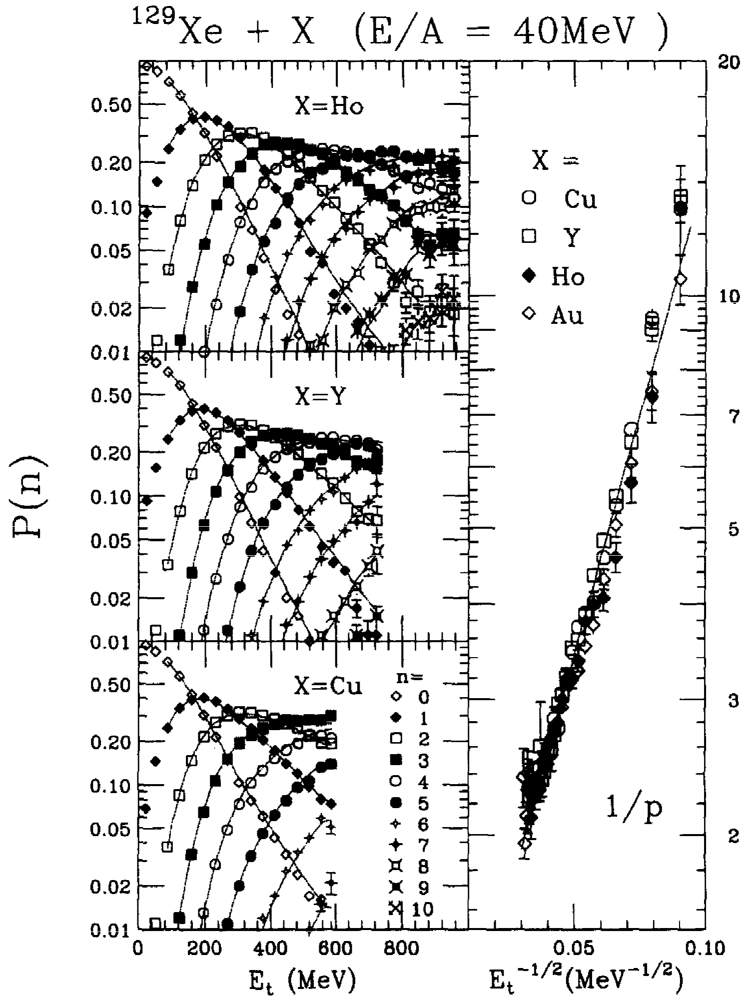

Figure 1.7: (Left column): The probability $P(n)$ for emitting n IMFs is shown as a function of E_t for ^{129}Xe-induced reaction on different targets: ^{nat}Cu, ^{89}Y and ^{165}Ho. Transverse energy $E_t = aT^2$ is a measure of temperature, where a is a constant. The solid curves are binomial calculations of $P(n)$. (Right column):The reciprocal of the single fragment emission probability $1/p$ is shown as function of $1/\sqrt{E_t}$ for different targets (^{nat}Cu, ^{89}Y, ^{165}Ho, ^{197}Au). The line is a linear fit to the data.

[More 97]. The thermal scaling of fragment distributions (their change with the temperature) is such that it is characteristic of thermalized systems (Arrhenius law). In addition to that, reducibility of fragment number distributions presents another proof of thermalization. Reducibility is the property of the IMF number distribution $P(n)$, with n being a number of IMFs, to be a function of the elementary probability p of emitting one fragment according to a statistical law, like binomial or Poissonian. Figure 1.7 demonstrates how knowledge of p can account for all observed fragment number distributions. Such reducibility is only possible if the fragments are formed completely independent of each other. Fragment independence is indicative of the lack of dynamical effects and confirms setting in of thermal equilibrium. In addition to that, the thermal scaling of the elementary probability p points to the barrier-controlled statistical emission.

As an aside it is important to mention that independence of fragment emission also validates the use of Fisher's model, which requires that the clusters lack interaction.

Secondly, there is a complication with the presence of the Coulomb force between the nucleons in the nucleus. The Coulomb force is long-range and hurts the equilibrium emission picture. This issue has already been touched upon in the discussion of the methodology of filtering the Coulomb effects from the data. Here, however, a justification for the methodology will be presented in more detail [More 03].

For an excited thermalized nucleus (a hot droplet), there may be two possible

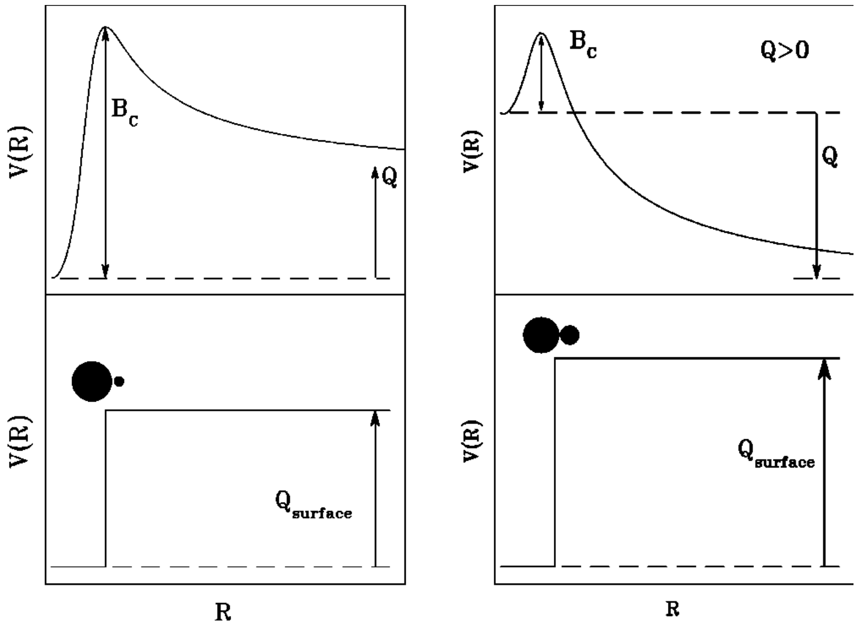

Figure 1.8: A schematic representation of the Coulomb correction when the emitted fragment is bound (left panels) and unbound (right panels).

scenarios of emitting a fragment (vapor): the fragment may be bound (Q-value is negative) or unbound (Q-value is positive). If the fragment is bound and has zero charge (neutron), a step is observed at the droplet radius equal to the fragment binding energy. For non-zero charges, a maximum B_C is observed at the approximate distance of the droplet and fragment in contact. From there the potential decreases according to the Coulomb law and settles down at infinity to a value equal to the binding energy of the fragment, as depicted in the left panel of Figure 1.8. In this case there is no difficulty in defining a gas phase in equilibrium with the liquid droplet. The Coulomb barrier B_C does not alter the equilibrium. Only kinetically it may slow down its achievement. The standard cluster techniques of the previous section can be used to obtain the phase diagram of the uncharged matter, filtering out the Coulomb effects simply as an unnecessary information.

A more problematic situation is shown in the right panel of Figure 1.8 that arises if the emitted fragment is unbound due to the Coulomb interaction. In this case the droplet is metastable, and the ground state of the system consists of two or more pieces of the original drop at infinity. Thus it is not possible to speak properly of this drop in statistical equilibrium with its vapor. For a nucleus such as gold the ground state consists of three fragments of charge about 30 and is more than a hundred MeV below the mass of the gold nucleus. Therefore, in equilibrium of a gold-like drop with its vapor, the most probable configuration for the liquid would be the three fragments of the true ground state, and not the metastable configuration of the whole gold nucleus. This situation is prohibitive to define phase coexistence for droplets larger than $A \approx 30$. However, there is a way to avoid this difficulty from the experimental point of view. The phase coexistence can be defined approximately. Again the solution comes from the consideration of the timing. On a sufficiently short time scale the fact that the droplet has unbound channels does not play a significant role. The fragment still has to jump over a barrier (combined surface and Coulomb) to leave the nucleus. If so, the first-chance emission rates from the metastable state still qualify as equilibrium as long as the droplet is thermalized. The rates then can be corrected for the Coulomb effects, leading to the rates of decay of an uncharged drop, for which all channels are bound: a situation identical to the case of filtering out Coulomb interaction in low-mass nuclei that do not have unbound channels.

Thus the technique of Coulomb filtering is universally applicable to any experimental cluster data without violating the condition of phase equilibrium in uncharged nuclear matter.

Thirdly, the nuclear droplets are of finite size as compared to the infinite nuclear matter. Therefore, the nuclear cluster distributions have the finite-droplet-size effects buried in them, which may lead to recovering the unwanted pressure of a finite system. For example, simple classical considerations show that the vapor pressure of a finite-size liquid drop is higher than that of a bulk liquid [More 02]. It follows from the liquid drop expansion of the molar evaporation enthalpy:

$$H_m = H_m^0 + c\frac{A^{2/3}}{A}, \tag{1.45}$$

where H_m^0 is the molar evaporation enthalpy of the infinite system, A is the size of the drop, and c is a coefficient proportional to the surface tension. The Clapeyron-Clausius equation for an ideal gas then gives:

$$P = P_\infty \exp\left(\frac{c}{A^{1/3}T}\right), \tag{1.46}$$

where P_∞ is the vapor pressure of the infinitely large amount of liquid. Unless these effects are accounted for, the resulting phase diagram is bound to represent the finite matter.

An answer to this criticism has been worked out by Moretto using the complement method [More 05]. It consists of evaluating the change in free energy occurring when a cluster is moved from one phase to another. In the case of a finite liquid drop in equilibrium with its vapor, this is done by transferring a cluster of any given size from the liquid drop to its vapor and by evaluating the energy and entropy changes associated with both the vapor cluster and the residual liquid drop (complement). This accounting can be generalized to incorporate other energy terms, as it has already been shown for Coulomb energy. Fisher's formula in Equation 1.29 has to be modified in the following way:

$$n_a = q_0 \left[\frac{a(a_d - a)}{a_d} \right]^{-\tau} \exp(-\beta c_0 \epsilon [a^\sigma + (a_d - a)^\sigma - a_d^\sigma]), \qquad (1.47)$$

where a_d is the size of the residual complement drop. Then, nuclear cluster distributions are analyzed with the complement included, whereas the phase diagram of the infinite matter is constructed with the finite-size effects taken out. Therefore, the finite-size "filtering" is accomplished in the same spirit as Coulomb filtering.

1.9 Simple Models to Test Cluster Techniques

The successful use of cluster techniques to recover the thermodynamics of the nuclear phase transition is impossible without the assurance that these techniques are at least valid for simple test models that mimic phase coexistence. If a certain cluster analysis technique produces an accurate liquid-vapor phase diagram for a model, there is a hope it might work for the nuclear data as well. Reliance on a test model is an inescapable weakness of the cluster method in nuclear physics, since it is hardly possible to have an exact nuclear cluster definition uniquely corresponding to the experimental distributions. If it were possible, an exact theory could be built to analyze the distributions, and the assurance would be presented by the theory itself. Since such theory does not exist, different cluster definitions must be tested on a simulated thermodynamic system with a known equation of state to come up with a definition that best reproduces the system's thermodynamics.

1.9.1 The Lattice Gas Model

Among such test models the lattice gas model is the simplest and most illustrative [Path 86, Huan 87]. It is a model of a simple fluid, in which atoms of the fluid are assumed to take on only discrete positions in space. These discrete positions form a lattice of given geometry with a fixed number γ of nearest neighbors to each lattice site. Each lattice site can be occupied by at most one atom. Figure 1.9 illustrates a configuration of a two-dimensional lattice gas in which the atoms are represented

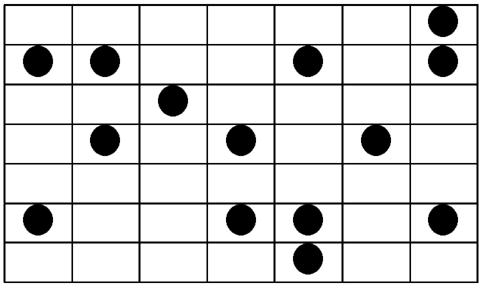

Figure 1.9: A sample realization of the lattice gas.

by solid circles. The kinetic energy of an atom is neglected, and it is assumed that only nearest neighbors interact with a constant interaction energy $-J_0$ of a pair. The lattice is usually assumed to be periodic to avoid the effects of the boundary, so that particles in one row or a column (a two-dimensional case) on the opposite sides of the lattice are considered nearest neighbors. The potential energy of the system is equivalent to that of a fluid in which atoms are located only on lattice sites and interact through a two-body potential $\mathtt{v}$ which can assume three possible values:

$$\mathtt{v} = \begin{cases} \infty & \text{if atoms are in the same site} \\ -J_0 & \text{if atoms are in nearest-neighbor sites} \\ 0 & \text{otherwise.} \end{cases} \tag{1.48}$$

Suppose a lattice gas container has N sites (49 in the example), and the number of atoms in the system is N_a (14 in the example). Also let N_{aa} be the total number of nearest-neighbor pairs (6 in the example). The total energy of the lattice gas is

$$E_{LG} = -J_0 N_{aa}, \tag{1.49}$$

and the partition function

$$Q_{LG}(N_a, T) = \frac{1}{N_a!} \sum_{\{a\}} \exp(\beta J_0 N_{aa}), \tag{1.50}$$

where T is the temperature in energy units (no Boltzmann constant k), $\beta = 1/T$, and the summation extends over all ways $\{a\}$ of distributing N_a distinguishable atoms over N lattice sites. The grand partition function of the gas on N sites (acts like the total volume V if one site is equated to a unit volume) is

$$\mathscr{L}_{LG}(z, N, T) = \sum_{N_a=0}^{N_a=N} z^{N_a} Q_{LG}(N_a, T), \tag{1.51}$$

where the fugacity is

$$z = \frac{1}{\lambda^3} \exp(\beta\mu) \tag{1.52}$$

with μ being the chemical potential per atom. Notice how the kinetic motion is inserted into the grand partition function of the lattice gas by making thermal wavelengths a part of the fugacity. The equation of state can be inferred from the grand partition function in a standard way:

$$\begin{aligned} \beta P_{LG} &= \frac{1}{N} \ln \mathscr{L}_{LG}(z, N, T) \\ \rho_{LG} &= \frac{1}{N} z \frac{\partial}{\partial z} \ln \mathscr{L}_{LG}(z, N, T) \end{aligned} \tag{1.53}$$

The lattice gas model is non-trivial, and qualitatively reproduces all the properties of a fluid. It displays the first-order phase transition and criticality. The thermodynamics of the lattice gas at coexistence in two dimensions have been found

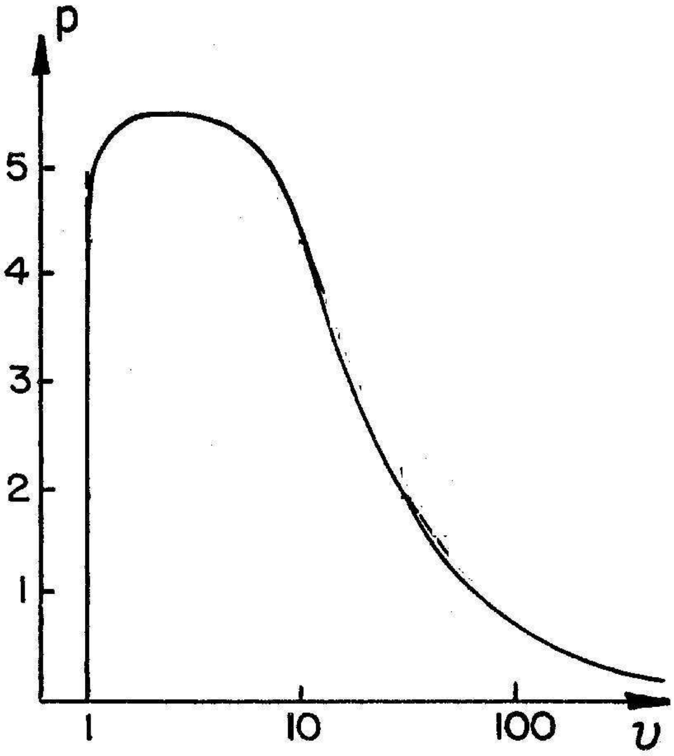

Figure 1.10: P-v-diagram for a two-dimensional lattice gas. The solid curve is the exact boundary of the two-phase region.

exactly, thus making the model an excellent tool to study liquid-vapor phase diagrams. Figure 1.10 demonstrates as an example a P-v-projection (v stands for the specific volume) of the lattice gas phase diagram in which the transition region is completely mapped out.

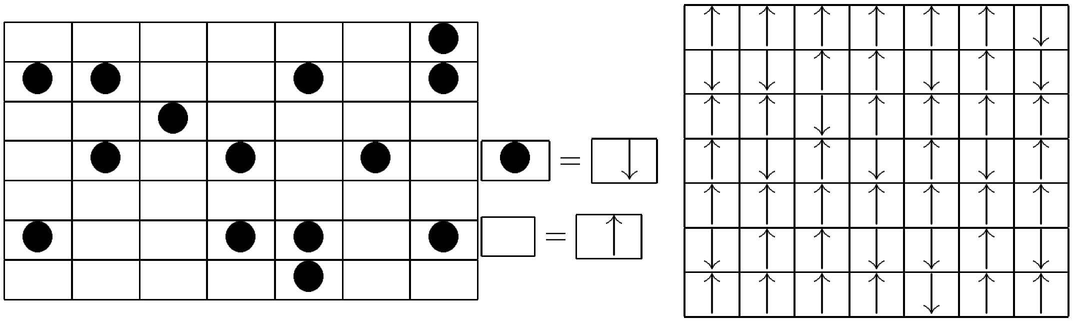

Figure 1.11: Equivalence of the lattice gas and the Ising model.

1.9.2 The Ising Model

The lattice gas model has an equivalent model coming from a different realm of physics. It is the Ising model, which was introduced in 1925 by Ernst Ising [Isin 25, Path 86, Huan 87] to study ferromagnetism, or the ability of some metals, like Fe and Ni, to sustain a macroscopic magnetic field as a result of spontaneous spin polarization of some atoms. In the model the system considered is a periodic lattice of N sites, like is shown in the right panel of Figure 1.11. Associated with each lattice site is a spin variable s_i $(i = 1 \ldots N)$ which is a number that is either +1 or -1. If $s_i = +1$, the ith site is said to have spin up, and if $s_i = -1$, it is said to have spin down. A given set of numbers $\{s_i\}$ specifies a configuration of the whole system with N_+ spins up and N_- spins down. Figure 1.11 shows how the equivalence between the lattice gas and the Ising model can readily be illustrated. The two identical lattices simply use different lattice variables to represent interaction. While the Ising lattice spin variables are ±1, the lattice gas uses the "atomic" variables 0 and 1.

The energy of the Ising system in the configuration specified by $\{s_i\}$ is defined to be

$$E_I\{s_i\} = -J \sum_{<ij>} s_i s_j - H \sum_{i=1}^{N} s_i, \tag{1.54}$$

where the first sum runs over all the spin pairs $< ij >$ in the configuration, of which there are $\gamma N/2$ with γ being the number of nearest neighbors of any given site. The interaction energy J and the external magnetic field H are given constants. The partition function is

$$Q_I(H,T) = \sum_{\{s_i\}} \exp(-\beta E_I\{s_i\}), \tag{1.55}$$

where the sum runs over all 2^N possible lattice spin configurations. The thermodynamic functions are obtained in a standard manner from the Helmholtz free energy:

$$F_I(H,T) = -T \ln Q_I(H,T) \tag{1.56}$$

An important function to mention is magnetization:

$$M_I(H,T) = -\frac{\partial}{\partial H}\left(\frac{F_I}{T}\right) \tag{1.57}$$

If $H = 0$ the quantity $M_I(0,T)$ is called the spontaneous magnetization.

In two dimensions at zero magnetic field the Ising model was solved exactly by Onsager [Onsa 44, Newe 53] for an infinite system, and then extended to finite systems by Kaufman [Kauf 49]. Yang found the exact expression for the spontaneous

Ising Model	Lattice Gas
N_+	N_a
N_-	$N - N_a$
$4J$	J_0
$\exp(2\beta(J\gamma - H))$	z
$-\left(\frac{F_I}{N} + \frac{1}{2}\gamma J - H\right)$	P_{LG}
$\frac{1}{2}\left(\frac{M_I}{N} + 1\right)$	ρ_{LG}

Figure 1.12: Some of the quantities in the lattice gas and their equivalents in the Ising model.

magnetization [Yang 52] [3].

The equivalence of the lattice gas and the Ising models means that the thermodynamics of the two models are equivalent, and exact ties can be found [YLee 52]. For example, the magnetic field variable is equivalent to the chemical potential variable in the lattice gas, the magnetization is equivalent to the density, and the sum of the free energy and the field strength (in proper units) is equivalent to the pressure. It can be shown that the zero field Ising model is equivalent to the lattice gas in the transition region below the critical temperature [YLee 52, Path 86], so that the Onsager solution can be used to characterize the phase boundary curve on the phase diagram of the lattice gas. The equivalence of the two models is summarized in Table 1.12.

---

[3] Historically it was Onsager who first found this expression in 1948 and demonstrated it during a conference on phase transitions as a challenge to the audience to find the derivation. However, he never published the derivation himself. Later Yang took the challenge and found the derivation in 1952. See [Brus 67]. This historical review has many useful references on the subject.

1.10 Model Clusters

The lattice gas and Ising models naturally allow clusters as groups of particles or spins. For example, in Figure 1.11 the lattice gas configuration of particles creates five clusters of size one, one cluster of size two, one cluster of size three, and one cluster of size four. The equivalent Ising configuration has the same clusters, which are formed by the spins of the same orientation.

These clusters are the simplest that can be created on the lattice, and are called geometric clusters. The only requirement necessary to define a geometric cluster is the requirement of proximity of particles in space. Any two particles are considered to belong to the same cluster if they are located next to each other, or there is an uninterrupted chain of nearest-neighbor particles in between them. Single particles are also considered as geometric clusters in which the only particle has no neighbors.

Geometric clusters can be characterized by their size and outer surface. The size is the number of lattice sites that fit inside a cluster, and the surface is the number of links a cluster has with neighboring empty sites (the lattice gas) or with spins of opposite direction (the Ising model).

In regard to their shape on the lattice geometric clusters are exactly equivalent to self-avoiding polygons or polyhedra (SAP) (also called polyominoes) depending on dimensionality [Gutt 00, Jens 00, Gutt 01], which can be punctured and non-punctured. For example, if a cluster in the two-dimensional Ising model is equivalent to a non-punctured polygon, it is possible to draw a curve around a group of like

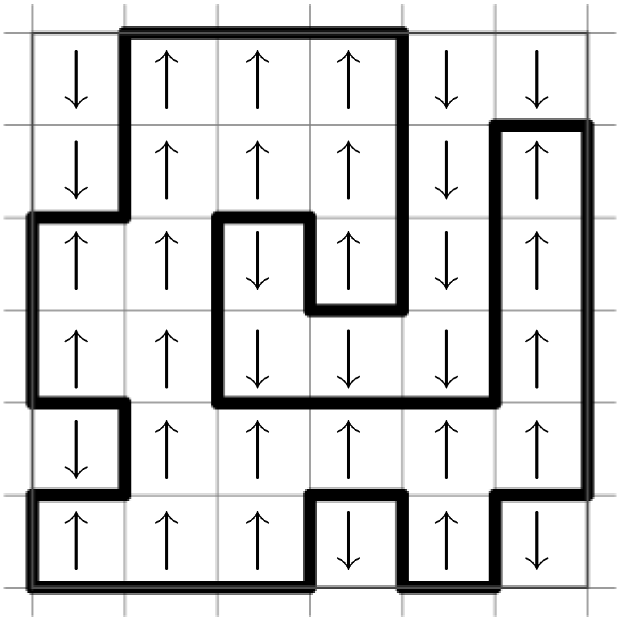

Figure 1.13: Equivalence of a geometric cluster of the two-dimensional Ising model to a non-punctured self-avoiding polygons (SAP).

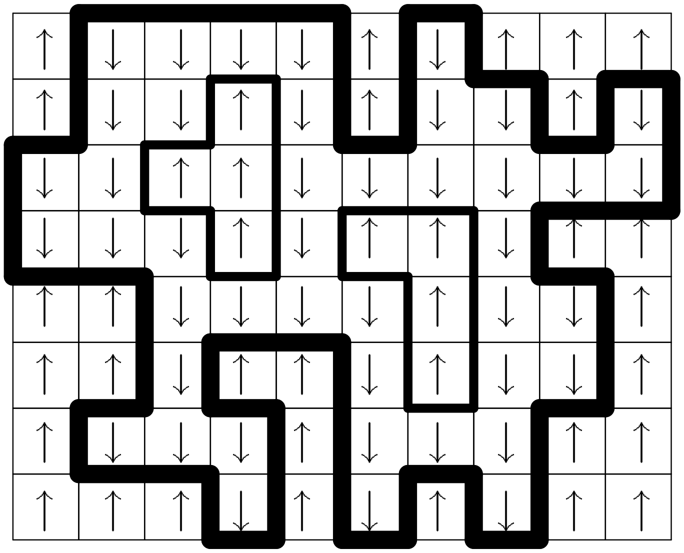

Figure 1.14: Equivalence of a geometric cluster of the two-dimensional Ising model to a punctured self-avoiding polygons.

spins in such a way that it passes along the border separating sites of opposite spins, and the resulting contour forms a polygon whose facets do not intersect (Figure 1.13). Punctured polygons by definition have internal voids in the shape of non-punctured polygons and correspond to those clusters that embed spins of opposite direction inside their bulk. These spins are like "holes" in the body of the cluster that create additional surface. Thus in addition to the outer contour, the equivalence is enabled by drawing internal non-intersecting contours around the holes of the cluster (Figure 1.14).

SAP are also characterized by their size and outer surface (including holes). The size is the number of unit volumes that fit inside SAP's volume, and the surface is the number of sides. Within each SAP size a the surfaces s vary from a minimum, corresponding to a compact non-punctured shape, to a maximum, which represents a string. The minimum perimeters do not have a clear dependence on the polygon size. For example, in two dimensions they roughly follow the square-root dependence $s_{min} = 4\sqrt{a}$, which is exact only for the square SAP of size $a = 1, 4, 9, 16, 25, \ldots$. The maximum surfaces are always exactly determined as linear functions of the SAP size: in two dimensions $s_{max} = 2a + 2$ and in three dimensions $s_{max} = 4a + 2$. Between the minimum and the maximum the surfaces vary as even numbers.

The equivalence of geometric clusters to SAP is very useful. It allows the exact counting of geometric clusters by size and surface to obtain the numbers $g_{SAP}(a, s)$. Knowledge of these numbers is very important for testing cluster analysis techniques.

Obtaining $g_{SAP}(a,s)$ analytically is an unsolved combinatorial problem which is being worked on by several research groups [Brak 90, Lin 91, Bous 96]. In the mean time numbers of SAPs can be obtained numerically [Jens 03] up to the size $a = 50$ in two dimensions and up to the size $a = 17$ (only $g_{SAP}(a)$ and non-punctured) [Flam 03] in three dimensions. It should be emphasized, however, that the subclass of punctured polygons is relatively small compared to the class of non-punctured shapes. For instance, polygons of size $a = 20$ are only about 1% punctured. As the cluster size grows, the relative number of the punctured clusters increases to reach about 50% at $a = 50$. Lattice configurations containing large clusters do not significantly contribute to the overall behavior of the Ising model. As a result, accurate representation of geometric clusters can be accomplished by considering them to be equivalent to the non-punctured polygons only, disregarding the effects of punctures.

Geometric clusters are of primary attention in this work due to their simplicity and a clear physical picture of cluster formation, which they portray.

1.11 Computer Simulations

The use of the lattice gas model as a test ground for the cluster techniques is accomplished through simulating it on a computer with Monte Carlo methods. Many configurations, like in Figure 1.9, should be stepped through in a random order simulating the behavior of the gas. Of course, only a limited number of most probable configurations can be realized this way, since their total number even for a relatively small system is astronomically large. Clusters in the reproduced configurations can be identified and counted to build the distributions, which then can be used to reconstruct thermodynamics of the model and compared to the accurately known values. However, numerical implementation of the lattice gas in a state on the phase boundary, or in other locations of the phase diagram requires the control over the chemical potential. Technically, it is much easier to deal with the Ising lattice, and change the magnetic field to simulate a particular state of the lattice gas. Therefore, numerical simulations of the lattice gas are usually done using the Ising model, and calculations for the phase boundary region are accomplished with the Ising model at zero magnetic field.

Numerical Monte Carlo (MC) simulation of the Ising lattice at a fixed temperature is accomplished using clustering algorithms. Clustering algorithms are rigorous instructions, programmable on a computer, of updating lattice realizations in an unbiased random order. Clusters here are portions of the lattice that are subject to change from realization to realization, and are not to be mixed with the model clusters. The larger the difference between successive configurations, the more stable the algorithm is in the vicinity of the critical temperature with respect to critical slowing down. Critical slowing down is the time necessary to achieve thermal equilibrium (lattice energy on the average does not change in time) on the lattice starting with an initial non-equilibrated state, say all spins up. Three major clustering algorithms have been developed to date [Land 00].

1.11.1 Metropolis Algorithm

This procedure was invented by Metropolis *et al.* in 1953 for sampling an arbitrary probability distribution. In the Metropolis algorithm, new configurations of the system are found by moving through all the lattice sites and updating the spin variables. A new configuration is generated by updating a single variable in the old configuration and calculating the change in energy of the lattice ΔE. If $\Delta E \leq 0$, the change is accepted. Otherwise, the change is accepted with probability $\exp(-\beta\Delta E)$. This represents a complete Metropolis MC cycle. Therefore, the Metropolis algorithm is considered a local method for reasons that it does not involve multispin clusters. As a result it is found to be very inefficient around the critical point due to critical slowing down.

1.11.2 Swendsen-Wang Algorithm

Swendsen-Wang is a true cluster algorithm, where clusters are identified by establishing bonds between pairs of neighboring spins. Building the appropriate cluster configurations and updating whole multispin clusters at a time, this algorithm appears to be much less sensitive to critical slowing down as compared to the Metropolis algorithm.

The steps of the Swendsen-Wang algorithm are the following:

1. Initialize the lattice to the first realization.

2. Examine every pair of neighboring spins in the system. If they are not parallel, do nothing. Otherwise, establish a bond between the two spins with probability $p = 1 - \exp(-2\beta J)$. In this way a bond configuration is obtained. Two spins belong to the same cluster if they are connected through a sequence of bonds. If a spin has no bond with any of its neighbors, it forms a cluster by itself.

3. Identify all clusters in the system. For each cluster. flip all its spins with probability 1/2. In this way a new configuration is obtained.

4. Repeat steps 2 and 3 (complete Swendsen-Wang MC cycle) until the desired number of configurations have been obtained.

1.11.3 Wolff Algorithm

The Wolff algorithm is similar to the Swendsen-Wang algorithm. The major difference is that the Wolff algorithm flips the spins of one particular cluster with probability 1 in every Wolff MC cycle, as compared to flipping all clusters with the probability 1/2 in the Swendsen-Wang algorithm.

The steps of the Wolff algorithm are:

1. Initialize the lattice to the first realization.

2. Chose a spin at random to be the seed of a cluster. Examine all its neighbors, and add the parallel ones to a list called a perimeter list.

3. Remove a spin from the perimeter list. For each of the neighbors that already belong to the cluster, a bond is established between the perimeter spin and the neighbor (effectively adding the perimeter spin to the cluster) with a probability $p = 1 - \exp(-2\beta J)$. If within the same Wolff MC cycle an earlier attempt was made to establish a bond between the perimeter spin and a neighbor, the neighbor is skipped in this step.

4. If the perimeter spin is not added to the cluster, repeat step 3. Otherwise, inspect its neighbors with parallel spins. If a parallel neighboring spin is neither in the cluster nor in the perimeter list, add it to the perimeter list. If it is already in the perimeter list or in the cluster, do nothing.

5. Repeat steps 3 and 4 until no spin remains in the perimeter list, then flip all the spins in the cluster.

6. Repeat steps 3 through 5 until the desired number of configurations have been obtained.

The Wolff algorithm eliminates the problem of critical slowing down completely, which makes it the most preferred method to implement Ising MC simulations.

1.11.4 Accumulation of Cluster Concentrations

Clusters are accumulated after the system is allowed to equilibrate. Cluster identification on the lattice realizations can be done with various methods, like the standard Hoshen-Kopelman technique found in textbooks [Land 00]. As a computer steps through lattice realizations, clusters are identified, sorted by their size and surface, and counted. After a desired number of lattice realizations have been reached, cluster numbers in every size and surface bin are divided by the total number of lattice realizations and the total lattice size N to get the concentrations. This way repeating the MC Ising simulation at various temperatures (the magnetic field is zero), cluster concentrations $n(a, s, T)$, which correspond to the phase boundary region of the lattice gas, can be found and used for testing purposes.

1.12 Goals of Project

When modeling physical cluster behavior on the lattice, the obvious question arises regarding the choice of a model cluster that best reflects the properties of a physical cluster in a Van der Waals fluid. In this study geometric clusters are chosen as model clusters in an attempt to demonstrate their elegance, simplicity and direct analogy to Stillinger's clusters. Therefore, this thesis deals with one model cluster definition and sets as one of its goals to show applicability of Stillinger's theory to geometric clusters using MC Ising simulations at zero magnetic field. In contrast, inadequacy of the ideal-cluster-gas approximation to describe geometric clusters is clearly shown.

In no way claims are being made that Stillinger's clusters are the only "good" clusters to study nuclear fluid. They are configurational clusters with no internal degrees of freedom that cannot fully reflect properties of nuclear liquid droplets. These properties have to be fully known in order to completely understand observed nuclear cluster distributions. However, Stillinger's clusters point to an opportunity of developing a new analysis technique on the basis of interacting-cluster gas. This opportunity can be justified referring to the work of LBA, who found little effect of precise physical cluster definition on the free energy of a cluster. Therefore, the second goal of this study is to develop a cluster analysis technique using Stillinger's theory in hopes that it may better describe nuclear clusters and account for their interference primarily due to the excluded volume. To gain more confidence in the technique, its testing is planned with SAP combinatorics, which is equivalent to the combinatorics of geometric clusters. In addition, systematic failure of the ideal-cluster-gas approximation is presented to contrast the results of the new method.

Analysis of incomplete nuclear cluster distributions is impossible without a cluster model, like Fisher's, that analytically parameterizes the distributions. Therefore, the new interacting-cluster technique should also be merged with Fisher's model, introducing a modified version of it. Design of a computer code that implements a least-squares fitting procedure for the analysis of cluster distributions using modified Fisher's model is the third goal of this work.

By itself the new cluster analysis technique cannot manifest any improvement. It has to be compared with the results of the ideal-cluster-gas analysis. Using geometric clusters, it is possible to observe certain specific signatures distinguishing the two analyses. On the other hand, it is possible to generate mockup distributions of geometric clusters using SAP combinatorics as if they were not interacting. Characteristic signatures can also be observed in this case. Overall, the hope is to find these signatures in the future analysis of nuclear cluster distributions. Therefore, the forth goal is to develop strategies to look for cluster interaction effects in nuclear cluster gas, which are mostly due to the excluded volume, which may manifest if nuclear clusters are similar to Stillinger's clusters.

If Stillinger's clusters are similar to nuclear clusters, then there is an expectation to substantially improve the nuclear liquid-vapor phase diagram obtained by Moretto's group using the ideal-cluster-gas methodology.

Chapter 2

Geometric Clusters of the Ising Model as Model Clusters

In this chapter, the properties of geometric clusters are studied from the point of view of Stillinger's theory, and the results are compared to the predictions of the ideal-cluster-gas approximation. In Section 2.1 geometric-cluster concentrations are studied exactly using the Ising model, and then the ideal-cluster-gas and Stillinger-based approximations are introduced. Section 2.2 shows how to obtain the lattice gas thermodynamics using geometric clusters according to various approximations. An alternative approach to connect cluster concentrations with the pressure at coexistence, not used previously in cluster analyses, is presented for the case of the Stillinger-based approximation. Numerical Monte Carlo Ising simulations and their use to obtain cluster concentrations are discussed in Section 2.3, while Section 2.4

presents a detailed comparison of simulated geometric-cluster concentrations and the lattice gas thermodynamics obtained from them with the corresponding predictions of the theoretical approximations.

2.1 Geometric-Cluster Concentrations

Geometric clusters were discussed at length in the introductory part of this thesis. They are configurational clusters that are defined according to the condition of proximity in space: two or more spins (or atoms) form a cluster if they occupy nearest neighbor lattice sites in an uninterrupted order so that every spin of the cluster is a nearest neighbor to at least one other spin of the same cluster.

The Ising model provides an unprecedented opportunity to study geometric clusters. Within the model, geometric-cluster concentration, *i.e* the average number of clusters per lattice site, can be related to the lattice gas thermodynamics in a clear and rigorous way [YLee 52]. At zero magnetic field the Ising model is equivalent to the lattice gas at the liquid-vapor phase boundary as a result of the one-to-one correspondence between the Ising field strength and the lattice gas chemical potential. Only at zero field reversing the direction of spins in the Ising lattice realizations does not change the energy of these realizations. On the other hand, the equivalent procedure of reversing the lattice gas realizations at constant chemical potential corresponds to a change of phases. The condition of two phases having the same energy and chemical potential below the critical temperature unambiguously points to phase coexistence, *i.e.* a region in the thermodynamic P-v-T-space, in which pressure, temperature and chemical potential of the liquid phase are equal to those of the gas phase.

In what follows below, geometric-cluster concentrations on the zero-field Ising lattice are obtained as an example of cluster production at liquid-gas phase coexistence. Adopting Stillinger's approach to a lattice [Stil 63], a probability p can be introduced that a geometric cluster of size a (the number of spins in the cluster), surface s (the number of links with the neighboring spins of opposite direction) and shape k (relative arrangement of spins within the cluster) can form in a particular location j of the lattice. The shapes of geometric clusters are equivalent to those of self-avoiding polygons or polyhedra (SAP) depending on the dimensionality (see Introduction for more details). For every particular size a and surface s of SAP, there may be many possible shapes, which can be counted and are denoted by $g_{SAP}(a, s)$, so that the counter k varies between unity and $g_{SAP}(a, s)$. All the cluster locations j on the lattice are distinct and also can be numbered. When moving from location j to a location $j + 1$, say to the right, every spin of the cluster moves to its nearest-neighbor position to the right. Depending on the lattice boundary conditions, the total number of locations may differ. Two types of boundary conditions are distinguished: open and periodic. In the case of open boundary conditions, the lattice has finite boundaries and is not closed on itself. The spins on the edge are not completely surrounded by nearest neighbors. As a result, the number of cluster locations depends on the cluster size and shape. On the other hand, periodic boundary conditions correspond to a lattice which is closed on itself, *e.g* in two dimensions a rectangular (or square as a particular case) lattice forms a torus. All the spins in such a lattice have the same number of nearest neighbors, and, as a result, the number of cluster locations is independent of cluster characteristics. In this case, if a lattice is of total size $\mathbb{N}$, there are $\mathbb{N}$ of such locations to place a cluster, so that the counter j goes from one to $\mathbb{N}$. Thus periodic boundary conditions help to eliminate the unimportant edge effects on a finite lattice and to simplify its geometry. Onsager used periodic boundary conditions in his solution of the two-dimensional Ising model. This thesis will also adhere to them. Therefore, recalling that the total number of possible lattice realizations is $2^{\mathbb{N}}$, the probability is

$$p(a, s, k, j, \beta, \mathbb{N}) = \frac{\sum\limits_{i=1}^{2^{\mathbb{N}}} \delta_{a,s,k,j}(i) \exp[-\beta E_i]}{\sum\limits_{i=1}^{2^{\mathbb{N}}} \exp[-\beta E_i]} \tag{2.1}$$

where the index i is the lattice realization counter. In Equation 2.1 $\delta_{a,s,k,j}(i)$ is the variable indicating the presence or the absence of the cluster of size a, surface s, and the shape k in the location j of the lattice realization i, and it can only take the values 0 or 1; E_i is the total energy of the realization i. The energy E_i consists of all the energies of clusters present in the particular realization i plus the energy of the ground state (all spins are parallel), since the total interface between the up and down spins is the sum of cluster surfaces. This property of the zero-field Ising model can be easily understood looking at the following mental exercise. The energy of the ground state of the lattice is $-1/2\gamma J\mathbb{N}$ (it can be readily checked using Equation 1.54 for the Ising lattice energy, which is the sum over all the spin pairs), where J is the interaction strength, and γ is the number of nearest neighbors. Suppose a cluster of spins is flipped in the middle of a two-dimensional square lattice, say a square cluster of size $a = 4$ (two by two). The energy of this new lattice state will consist of three components: the energy of four parallel spin pairs inside the cluster, the energy of eight antiparallel spin pairs on the surface of the cluster, and the energy of $2\mathbb{N} - 4 - 8$ parallel spin pairs outside the cluster. Clearly, the energy of parallel spin pairs inside and outside the cluster are of the same negative sign totaling $-2J\mathbb{N}+8J$, whereas the interface energy $8J$ is positive. Therefore, the total energy of the new lattice realization is $-2J\mathbb{N} + 16J$, which is $16J$ above the ground state. As it can be seen, this energy above the ground state is interface-only dependent, and flipping more spins to create other clusters will increase the energy above the ground state in proportion to the increasing interface. This dependence of the lattice energy on the surface of geometric clusters at coexistence is possible because geometric clusters do not share their surface between each other. They are clearly separated one from another and cannot touch, for otherwise a larger cluster is formed.

Notice also that the energy above the ground state is always $2J$ times the total surface (number of antiparallel spin pairs) irrespective of dimensionality. The quantity $2J$, denoted as c, is the surface energy coefficient (surface tension). Therefore, in the zero-field Ising model the cluster energy $E(a, s)$ (energy above the ground state to form a cluster) is proportional to the surface s of a cluster:

$$E(a,s) = cs = 2Js. \tag{2.2}$$

For those realizations where a cluster of size a, surface s and shape k is present, it is always possible to separate the energy of the cluster $E(a,s)$ from the energy of the remaining clusters E'_i, which also includes the ground state energy:

$$E_i = E(a,s) + E'_i \tag{2.3}$$

Then the probability p can be written in the following form:

$$p(a,s,k,j,\beta,\mathbb{N}) = \exp[-\beta E(a,s)] \frac{\sum_{i=1}^{2^{\mathbb{N}}} \delta_{a,s,k,j}(i) \exp[-\beta E'_i]}{\sum_{i=1}^{2^{\mathbb{N}}} \exp[-\beta E_i]}, \tag{2.4}$$

where the Boltzmann factor of the cluster energy can be factored out because of δ, which automatically eliminates all the terms in the sum not satisfying the required condition. The quantity

$$w(a,s,k,j,\beta,\mathbb{N}) = \frac{\sum_{i=1}^{2^{\mathbb{N}}} \delta_{a,s,k,j}(i) \exp[-\beta E'_i]}{\sum_{i=1}^{2^{\mathbb{N}}} \exp[-\beta E_i]} \tag{2.5}$$

can be understood as the probability that other clusters around the specified cluster do not affect its formation. If other clusters were not present in any configuration (hypothetically), then all the lattice realizations contained only the specified cluster, and $w = 1$. This assumption, also called dilute limit, is a typical hypothesis of the ideal cluster gas approximation. Clusters are believed to be so far apart in their phase space that their trajectories never cross excluding the possibility of interference. In the opposite extreme situation, the specified cluster can never be formed, and $w = 0$. Such condition may be observed in a cold liquid when condensed fluid forms one giant cluster the size of the volume of the liquid. In this case formation of smaller clusters is absolutely prohibited. At intermediate densities w acts as a weight factor lowering the cluster formation probability in the midst of interference (interaction) with other clusters.

The concentration n of geometric clusters of size a and surface s (number of clusters per site of the lattice) can be found as a sum of probabilities p over all the possible shapes $g_{SAP}(a,s)$ that a cluster of size a and surface s can have, and over all the lattice locations divided by the total lattice size:

$$n(a,s,\beta,\mathbb{N}) = \frac{\exp[-\beta E(a,s)]}{\mathbb{N}} \sum_{j=1}^{\mathbb{N}} \sum_{k=1}^{g_{SAP}(a,s)} w(a,s,k,j,\beta,\mathbb{N}) = g(a,s,\beta,\mathbb{N}) \exp[-c\beta s], \tag{2.6}$$

where

$$g(a,s,\beta,\mathbb{N}) = \frac{1}{\mathbb{N}} \sum_{j=1}^{\mathbb{N}} \sum_{k=1}^{g_{SAP}(a,s)} w(a,s,k,j,\beta,\mathbb{N}) \tag{2.7}$$

can be interpreted as the average number of shapes for the cluster of size a and surface s, which can form on the Ising lattice at temperature $T = 1/\beta$. This number is less than the corresponding number $g_{SAP}(a,s)$ of all the possible shapes because of the presence of other clusters and the resulting interference. This interference is entirely of geometric origin and comes from the fact that the freedom of a cluster to change its shape on the lattice is limited by the temperature dependent presence of other clusters that force the cluster in consideration to “squeeze” in between them. This causes the mutual suppression of geometric-cluster production on the Ising lattice. Therefore, it may be possible to understand geometric-cluster distributions of the Ising model if it is possible to determine average cluster-shape numbers, which are not constants, like $g_{SAP}(a, s)$, but vary with temperature and the size of the lattice.

The quantity $\mathbb{N}n(a, s, \beta, \mathbb{N})$ is the partition function of a cluster of size a and surface s:

$$q(a, s, \beta, \mathbb{N}) = \mathbb{N}n(a, s, \beta, \mathbb{N}) = \exp[-\beta F(a, s, \beta, \mathbb{N})], \tag{2.8}$$

where

$$F(a, s, \beta, \mathbb{N}) = E(a, s) - TS(a, s, \beta, \mathbb{N}) \tag{2.9}$$

is the cluster free energy with

$$S(a, s, \beta, \mathbb{N}) = \ln\left[\mathbb{N}g(a, s, \beta, \mathbb{N})\right] \tag{2.10}$$

being the cluster entropy according to the Boltzmann law. Equations 2.8, 2.9, and 2.10 are included here to emphasize that the effects of cluster interaction (interference) enter the individual-cluster thermodynamics through the entropic part of the cluster free energy. These equations will be useful later when applying Stillinger’s methodology to geometric clusters.

2.1.1 Geometric Clusters as an Ideal Gas

It has been shown in the previous section that geometric clusters may not be considered as non-interacting. The combinatorial factor g entering the cluster distributions varies with temperature and lattice size as a result of cluster interference. Nevertheless, it may still be beneficial to assume the condition of dilute limit so that geometric clusters may be thought of as an ideal gas with the goal to estimate the extent of their interaction.

Application of the ideal-cluster-gas approximation renders geometric clusters free to take all the possible shapes $g_{SAP}(a,s)$ in any position j on the lattice without being restricted by the surrounding clusters. Such an assumption may be good enough for dilute systems, but becomes quite unrealistic at high densities or near the critical point. It is equivalent to taking all the values w in Equation 2.6 to be unity. The concentration of clusters in such an ideal gas becomes

$$n(a,s,\beta) \approx \frac{\exp[-\beta E(a,s)]}{\mathbb{N}} \sum_{j=1}^{\mathbb{N}} \sum_{k=1}^{g_{SAP}(a,s)} 1 = g_{SAP}(a,s) \exp[-c\beta s], \qquad (2.11)$$

which is no longer a function of $\mathbb{N}$, and is characterized by the temperature independent combinatorial factor (number of cluster shapes).

2.1.2 Geometric Clusters According to Stillinger

The analogy between geometric and Stillinger's clusters has been noted in the Introduction. It seems reasonable to apply to geometric clusters the same arguments

Stillinger used in his theory. Stillinger's clusters of size a are shown to have a two-factor formation probability $p_a[\mathbf{r}]$ in a container location $\mathbf{r}$:

$$p_a[\mathbf{r}] = p_a^0 \exp(-\beta W[a, \mathbf{r}]), \tag{2.12}$$

where $\mathbf{r}$ is an array of radius-vectors of individual particles in the cluster, p_a^0 is the location independent formation probability of a cluster in the absence of interaction, and $W[a, \mathbf{r}]$ is the free energy needed to form a cavity around a cluster in the medium of other clusters to account for the interaction. This free energy is due to the change in entropy of the whole system owing to the formation of such a cavity, which restricts the available space for other clusters and creates room for the new cluster. The Boltzmann factor of the cavity formation free energy $\exp(-\beta W[a, \mathbf{r}])$ is, in fact, a probability that the new cluster will not interact with other clusters: in ideal-gas-like systems it is unity, while in dense environments it tends to zero. The variation in shape of Stillinger's clusters is implied by radius-vectors $\mathbf{r}$, since in any location of the container, which is fixed by the condition of constant center of mass of a cluster, there are many possibilities for individual radius-vectors to satisfy this condition.

Now consider a geometric cluster of size a, surface s and shape k in the lattice location j. By analogy with Equation 2.12, the cluster formation probability can be written as

$$p(a, s, k, j, \beta, \mathbb{N}) = \exp(-c\beta s) \exp[-\beta W(a, s, k, j, \beta, \mathbb{N})], \tag{2.13}$$

where it can be noticed that

$$w(a,s,k,j,\beta,\mathbb{N}) = \exp[-\beta W(a,s,k,j,\beta,\mathbb{N})] \tag{2.14}$$

according to Equations 2.4 and 2.5. In other words, the constraining effect of other clusters on the formation probability of the cluster in consideration can be attributed to the free energy of creating a cavity on the lattice. This free energy comes as a result of reduced entropy of other clusters which is due to restricting their configurational space. Then the concentration can be written as

$$n(a,s,\beta,\mathbb{N}) = g_{SAP}(a,s)\frac{\exp[-c\beta s]}{\mathbb{N}g_{SAP}(a,s)}\sum_{j=1}^{\mathbb{N}}\sum_{k=1}^{g_{SAP}(a,s)}\exp[-\beta W(a,s,k,j,\beta,\mathbb{N})] \tag{2.15}$$

According to Stillinger, the cavity formation free energy can be calculated and consists of two contribution (*cf.* Equation 1.38):

$$\beta W(a,s,k,j,\beta,\mathbb{N})] = \beta P v(a,s) + f(a,s,k,j,\beta,\mathbb{N},\rho) \tag{2.16}$$

where P is the lattice gas pressure, $v(a,s)$ is the volume of a cavity around the cluster of size a and surface s, and f is a position and cluster dependent function of the lattice gas density ρ. Therefore, the cluster concentration becomes

$$n(a,s,\beta,\mathbb{N}) = g_{SAP}(a,s)\exp[-c\beta s]\exp[-\beta P v(a,s)]\left\langle \exp[-\beta f]\right\rangle(a,s,\beta,\mathbb{N},\rho), \tag{2.17}$$

where

$$\left\langle \exp[-\beta f]\right\rangle(a,s,\beta,\mathbb{N},\rho) = \frac{\sum_{j=1}^{\mathbb{N}}\sum_{k=1}^{g_{SAP}(a,s)}\exp[-\beta f(a,s,k,j,\beta,\mathbb{N},\rho])}{\mathbb{N}g_{SAP}(a,s)} \tag{2.18}$$

The quantity $\langle \exp[-\beta f]\rangle\,(a,s,\beta,\mathbb{N},\rho)$ can be expressed in terms of $\langle f\rangle\,(a,s,\beta,\mathbb{N},\rho)$:

$$\langle \exp[-\beta f]\rangle = \exp[-\beta\,\langle f\rangle] + \frac{1}{2}\,\frac{\partial^2}{\partial f^2}\exp[-\beta f]\bigg|_{\langle f\rangle}\sigma_f^2 + \ldots = \exp[-\beta\,\langle f\rangle](1+\beta^2\sigma_f^2+\ldots) \tag{2.19}$$

Equation 2.19 is the infinite moment expansion [1] of the average function in terms of its average argument. Only even-order moments appear [2] in the expansion. The first two moments shown here can be calculated as follows:

$$\langle f\rangle\,(a,s,\beta,\mathbb{N},\rho) = \frac{\sum\limits_{j=1}^{\mathbb{N}}\sum\limits_{k=1}^{g_{SAP}(a,s)} f(a,s,k,j,\beta,\mathbb{N},\rho)}{\mathbb{N}g_{SAP}(a,s)} \tag{2.20}$$

is the zeroth moment, and

$$\sigma_f^2(a,s,\beta,\mathbb{N},\rho) = \frac{\sum\limits_{j=1}^{\mathbb{N}}\sum\limits_{k=1}^{g_{SAP}(a,s)} [f(a,s,k,j,\beta,\mathbb{N},\rho) - \langle f\rangle\,(a,s,\beta,\mathbb{N},\rho)]^2}{\mathbb{N}g_{SAP}(a,s)} \tag{2.21}$$

is the second moment. It is important to notice, that f is averaged over positions on the lattice and shapes of the cavity. For a large enough lattice, various positions tend to become equally probable, *i.e.* the distribution of f with j is flat. Similar situation can be conjectured regarding the distribution of f with the shapes k, since the cavity volume does not appreciably change with the shape (it depends on the thickness of the surface). These arguments lead to a reasonable approximation:

$$\langle \exp[-\beta f]\rangle \approx \exp[-\beta\,\langle f\rangle], \tag{2.22}$$

---

[1] The methodology of the statistical moment expansion and its derivation are thoroughly presented in the second part of this thesis. See Section 5.2 for more information.

[2] As demonstrated in Section 5.2 of Part 2 of this thesis, the odd-order statistical moments of the expansion do not survive the averaging operation since the positive and negative deviations from the average cancel each other in the infinite limit of the number of individual deviations. Obviously, this does not occur to the even-order moments.

which yields the following cluster concentrations:

$$n(a,s,\beta,\mathbb{N}) = g_{SAP}(a,s)\exp[-c\beta s]\exp[-\beta P v(a,s)]\exp[-\beta\left\langle f\right\rangle(a,s,\beta,\mathbb{N},\rho)] \tag{2.23}$$

Geometric-cluster concentration in Equation 2.23 may not be further simplified without introducing more approximations due to extreme complexity of the quantity $\left\langle f\right\rangle(a,s,\beta,\mathbb{N},\rho)$. Each of the approximations will now be discussed in turn.

First of all, the size of the lattice $\mathbb{N}$ does not significantly affect the cluster production unless the clusters are of size comparable with $\mathbb{N}$. As $\mathbb{N}$ tends to infinity, the dependence completely disappears in the thermodynamic limit. Therefore, for large enough lattices the finite-container effects can be safely disregarded.

Secondly, the quantity $\left\langle f\right\rangle(a,s,\beta,\mathbb{N},\rho)$ can be approximated using the RFL theory of the fluid of spheres (disks in two dimensions or rods in one dimension) [Lebo 65]. In the words of Stillinger, "... if the cluster almost always had a smooth spherical surface, ... the Reiss-Frisch-Helfand-Lebowitz theory of spherical cavity formation work in real fluids would apply" [Stil 63]. If Stillinger's clusters are constrained to form spherical cavities, and attraction is neglected, Stillinger's theory should approximately reduce to RFL description. Therefore, the density dependent part of the cavity free energy can be adopted from RFL. They derived the following expressions for the quantity $\left\langle f\right\rangle$ in one, two and three dimensions [Lebo 65]:

$$1D\text{: } \beta\left\langle f\right\rangle(\rho) = -\ln(1-\rho)$$

$$\begin{aligned} 2D\text{: } \beta\left\langle f\right\rangle(R,\rho) &\approx -\ln(1-\rho)+\frac{\rho_s}{1-\rho}R \\ 3D\text{: } \beta\left\langle f\right\rangle(R,\rho) &\approx -\ln(1-\rho)+\frac{\rho_s}{1-\rho}R+\left[\frac{2\rho_c}{1-\rho}+\frac{3\rho_s^2}{(1-\rho)^2}\right]R^2, \end{aligned} \tag{2.24}$$

where $R = R(a)$ is the radius of the sphere, and

$$\begin{aligned} \rho_c &= \sum_a 2\pi R(a)n(a,\beta) \text{ in } 3D \text{ only} \\ \rho_s &= \begin{cases} \sum_a 2\pi R(a)n(a,\beta) & \text{in } 2D \\ \sum_a 4\pi R(a)^2 n(a,\beta) & \text{in } 3D \end{cases} \\ \rho &= \begin{cases} \sum_a ln(a,\beta) & \text{in } 1D \\ \sum_a 4\pi R(a)^2 n(a,\beta) & \text{in } 2D \\ \sum_a \frac{4}{3}\pi R(a)^3 n(a,\beta) & \text{in } 3D \end{cases} \end{aligned} \tag{2.25}$$

are circular, surface, and volume densities, respectively, and $n(a, \beta)$ is the concentration of spherical clusters of size a. Their interpretation depends on dimensionality. In three dimensions the volume density ρ is the density in its usual meaning as a fraction of the container volume taken up by the volume of all the spheres. In two dimensions it is a fraction of the container surface occupied by the surface of all the circles, and in one dimension it is just the fractional length of all the rods of length l on the container string. The surface density ρ_s in three dimensions is the total sphere surface per container volume with a similar definition in terms of a circumference in two dimensions. The circular density ρ_c, which appears only in three dimensions, can be interpreted as the average density of spherical cluster's linear measure (circumference if a cut through the center is made). All these densities are intricately intertwined to account for the volume, surface and curvature effects in the cavity formation.

Depending on the dimensionality of the problem, corresponding approximations for $\langle f \rangle$ can be introduced to describe geometric-cluster concentrations. In this work, however, the simplest one-dimensional form will be employed and tested with geometric clusters. No clear reason can be offered at this time to justify the choice except that of empirical validity for geometric clusters of the two-dimensional Ising model. It will be shown later in this chapter that the simulated concentrations of geometric clusters very accurately follow the one-dimensional form of $\langle f \rangle$, and no need exists to introduce more complex approximations. Some speculations, however, can be considered as to why the one-dimensional form of $\langle f \rangle$ works well to account for cluster interference. This form is a part of $\langle f \rangle$ in all dimensions of interest (one, two, and three), and represents the zeroth-order effect of placing a sphere in the container (a point sphere effect). This is the effect of having something in comparison with nothing, a sharp transition from no effect to finite effect. On the other hand, the other terms describe specific properties of the newly placed sphere (surface, curvature) and only modify the extent of the already existing effect. These modifications may not be significant. As an example, consider Fourier transformation of a function. If the function is smooth and not dramatically varying with its argument in the range of consideration, the zeroth-order Fourier coefficient is by far the most dominant and can reasonably well approximate the function with a constant. The less important higher-order coefficients only improve upon the approximation and determine the extent of the deviation from the constant.

When applied to Equation 2.23, the one-dimensional form of $\langle f \rangle$ yields an elegant pressure and density dependent approximation for cluster concentrations, that can be readily calculated analytically in one and two dimensions for which the Ising model is solved exactly. The concentrations are:

$$n(a, s, \beta) \approx g_{SAP}(a, s) \exp[-c\beta s] \exp[-\beta P v(a, s)](1 - \rho) \tag{2.26}$$

Thirdly, the issue of the geometric-cluster cavity volume needs to be addressed. On the Ising lattice the volume of a cavity $v(a, s)$, which is formed to contain the cluster of size a and surface s, consists of two contributions. The first contribution is from the size a of the cluster itself, which forms the core of the cavity volume. The second contribution is from the cluster surface of finite thickness. For a cluster to maintain its identity, there has to be a shell of sites around the core that is inaccessible to other clusters, since otherwise they would join the cluster. This shell consists of a maximum of s sites for compact or small clusters, but may contain less then s if a cluster has stringy parts with bends in the string. The bends cause the number of sites around the cluster to be less then the number of links to them, which constitute the cluster surface. In this case the shell is not exactly related to the surface. For example, two-dimensional geometric cluster of size three and surface (perimeter) eight can have two irreducible shapes (which cannot be transformed into each other by rotation): a string and an angle. The string-shaped cluster has eight nearest-neighbor sites around it, whereas the angle-shaped cluster has only seven. Nevertheless, as a good approximation, it will be assumed in this work that the shell always has s sites, since compact or small clusters appear more frequently on the lattice due to the less energy requirements. Therefore, in addition to a core sites of the cluster the cavity should contain s shell sites around the core, which represent the cluster surface of finite thickness. The shell thickness t_s should necessarily be introduced for generality yielding the following approximate form for the cavity volume:

$$v(a, s) \approx a + t_s s, \tag{2.27}$$

which is exact for compact and some small clusters. The shell thickness is equal to the lattice spacing, *i.e.* the distance between the sites of the lattice. If the cavity volume is measured in units of lattice sites, the shell thickness is unity. Such definition of the cavity volume provides for an elegant way to introduce surface deformation effects into an otherwise spherical description of the finite volume effects in Equation 2.26. Clearly, the geometric-cluster surface shell contribution to the cavity volume is a significant fraction of the total, that can be the largest for small or strongly deformed clusters recalling that s varies between about $4\sqrt{a}$ and $2a+2$ in two dimensions, and even more radically in three dimensions.

Thus the concentration of geometric clusters on the Ising lattice to be explored in this work may be approximated by the following expression:

$$n(a, s, \beta) \approx g_{SAP}(a, s) \exp[-c\beta s] \exp[-\beta P(a + st_s)](1 - \rho), \qquad (2.28)$$

in which the temperature dependence of combinatorial factors has been factored out. For simplicity Equation 2.28 will be referred to as the finite volume approximation (FVA) throughout this thesis.

2.2 Coexistence Lattice Gas Thermodynamics with Geometric Clusters

As mentioned earlier in the Introduction, thermodynamics of a system are obtainable through clusters using a cluster model. In the following, two formalisms are presented to extract thermodynamics of the lattice gas at the liquid-vapor coexistence using geometric clusters as an ideal gas and as a gas of Stillinger's clusters. In the case of Stillinger's clusters, the theory is modified to suit the requirements at coexistence, and the cluster concentrations are assumed to obey the finite volume approximation according to Equation 2.28.

2.2.1 Ideal Cluster Gas

In the framework of the ideal cluster gas approximation the lattice gas pressure and density below the critical temperature can be evaluated using Equations 1.18 as applied to geometric cluster concentrations:

$$\begin{aligned} P &\approx T\sum_{a,s} n(a,s,\beta) \\ \rho &\approx \sum_{a,s} an(a,s,\beta) \end{aligned} \tag{2.29}$$

Criticality of the lattice gas at coexistence can in principle be observed in the behavior of the heat capacity at constant volume C_V, which can be calculated from pressure using standard thermodynamic relations:

$$\begin{aligned} c_V = \frac{C_V}{V} &= \frac{1}{V}\left.\frac{\partial E}{\partial T}\right|_V \\ \frac{E}{V} &= T\left.\frac{\partial P}{\partial T}\right|_\mu - P = T^2\left.\frac{\partial}{\partial T}\left(\frac{P}{T}\right)\right|_\mu \end{aligned} \tag{2.30}$$

where E is the energy of the lattice gas, and μ is the chemical potential, V is the volume of a system, and c_V is the heat capacity per unit volume. At the critical point c_V is infinite in the thermodynamic limit, which is a characteristic signature of the second order phase transition. [3] If the lattice size is finite, the heat capacity is expected to have a peak of finite hight at the critical temperature. This peak may allow determination of the critical temperature for finite systems. The lattice gas heat capacity per one lattice site within the ideal cluster gas approximation is

$$\begin{aligned} c_V = \frac{\partial}{\partial T}T^2\frac{\partial}{\partial T}\left.\left(\frac{P}{T}\right)\right|_{\mathbb{N},\mu} &\approx 2T\sum_{a,s}\frac{d}{dT}n(a,s,\beta) + T^2\sum_{a,s}\frac{d^2}{dT^2}n(a,s,\beta) \\ &\approx c^2\beta^2\sum_{a,s} s^2 g_{SAP}(a,s)\exp[-c\beta s], \end{aligned} \tag{2.31}$$

which can be easily derived using Equations 2.29 and 2.30.

---

[3] Critical phenomena are qualified as second order phase transitions, which are particularly characterized by the infinite discontinuity in the second derivative of fluid's free energy with respect to temperature. Heat capacity contains such a derivative, as it can be seen in Equation 2.30 recalling that the free energy is proportional to the pressure.

2.2.2 Non-Ideal Cluster Gas

Stillinger's cluster theory can be used to obtain the lattice gas pressure and density from geometric clusters using Equations 1.37. If, however, cluster concentrations off coexistence are not available [4], they cannot be integrated over the chemical potential to obtain the pressure. This problem can be overcome by performing the calculation of the coexistence pressure and other thermodynamics using the energy of the system as a function of temperature. In the Ising model geometric-cluster concentrations can be used to calculate the average lattice energy exactly due to their direct relation to the energy of a single lattice realization i:

$$E_i = c\mathbb{S}_i - \frac{1}{2}\gamma J\mathbb{N}, \tag{2.32}$$

where $\mathbb{S}_i$ is the total surface between the up and down spins (the number of opposite-spin pairs) in a realization. The energy $c\mathbb{S}_i$ is above the lattice ground state energy $-1/2\gamma J\mathbb{N}$, where $c = 2J$ is the surface energy coefficient, $\mathbb{N}$ is the total number of spins on the lattice, J is the interaction constant, and γ is the number of the nearest neighbors of a spin on the lattice. Geometric clusters have a well defined surface, not shared between the clusters, which is the number of links with opposite spins

---

[4] A somewhat artificial difficulty for geometric clusters, since non-zero field MC simulations can be easily performed. This made up problem, however, is raised to solve a real problem with nuclear clusters, for which experimental distributions are assumed to pertain only to the coexistence of liquid and gas due to the exponential fall-off of the cluster's abundance with their size (number of nucleons). If the system were in the gas-only region, only monomers could be observed. In the liquid-only region, the cluster abundance would increase exponentially with the cluster size. As it is, however, the limited presence of multimers supports the assumption of coexistence. At coexistence, standard Stillinger's approach cannot be used, since the chemical potential is not an independent function of temperature.

bordering the cluster. Therefore, the total surface of a realization $\mathbb{S}_i$ is composed of a sum of surfaces of all the geometric clusters present in this realization:

$$\mathbb{S}_i = \sum_{a,s} sN_i(a,s), \tag{2.33}$$

where $N_i(a,s)$ is the number of clusters of size a and surface s in a realization i. Then the average energy per spin of the Ising lattice u_I can be calculated as follows:

$$\begin{aligned} u_I &= \frac{\sum\limits_{i=1}^{2^{\mathbb{N}}} E_i \exp(-\beta E_i)}{\mathbb{N}2^{\mathbb{N}} \sum\limits_{i=1}^{2^{\mathbb{N}}} \exp(-\beta E_i)} \\ &= c\sum_{a,s} \frac{s\sum\limits_{i=1}^{2^{\mathbb{N}}} N_i(a,s)\exp(-\beta E_i)}{\mathbb{N}2^{\mathbb{N}} \sum\limits_{i=1}^{2^{\mathbb{N}}} \exp(-\beta E_i)} - \frac{\frac{1}{2}\gamma J \sum\limits_{i=1}^{2^{\mathbb{N}}} \mathbb{N}\exp(-\beta E_i)}{\mathbb{N}2^{\mathbb{N}} \sum\limits_{i=1}^{2^{\mathbb{N}}} \exp(-\beta E_i)} \\ &= c\sum_{a,s} sn(a,s,\beta) + u^g, \end{aligned} \tag{2.34}$$

where $u^g = -1/2\gamma J$ is the Ising ground state energy per spin.

The average energy above the ground state u is related to the lattice gas pressure at coexistence through a standard thermodynamic relation:

$$u = c\sum_{a,s} sn(a,s,\beta) = T\left.\frac{\partial P}{\partial T}\right|_{\mu} - P \tag{2.35}$$

Therefore, the knowledge of the geometric-cluster concentrations as functions of temperature obtained at coexistence is sufficient to determine the pressure. The first-order differential equation with the initial condition $P(T=0)=0$ can be solved in order to get the PT coexistence line.

Using the approximate form for the cluster concentrations, the pressure and density of the lattice gas can be evaluated using SAP combinatorics. Since the concentrations are density and pressure dependent quantities, they can be written in the following way:

$$n(a,s,\beta,P,\rho) \approx g_{SAP}(a,s)\exp(-c\beta s)\exp[-\beta(a+st_s)P](1-\rho) \tag{2.36}$$

A system of equations

$$\begin{aligned} T\left.\frac{\partial P}{\partial T}\right|_{\mu} - P &\approx c\sum_{a,s} sn(a,s,\beta,P,\rho) \\ \rho &\approx \sum_{a,s} an(a,s,\beta,P,\rho) \end{aligned} \tag{2.37}$$

can be defined, that enables the lattice gas pressure and density calculation in the range of validity of Equation 2.36. For concise reference this methodology will be called differential equation technique (DET) in the rest of the thesis.

In Equations 2.37 the density can be expressed as a function of the pressure:

$$\rho \approx \frac{\sum_{a,s} an'(a,s,\beta,P)}{1+\sum_{a,s} an'(a,s,\beta,P)}, \tag{2.38}$$

where

$$n'(a,s,\beta,P) \approx g_{SAP}(a,s)\exp(-c\beta s)\exp[-\beta(a+st_s)P] \tag{2.39}$$

is the density independent part of the geometric cluster concentrations. Then an approximate first-order differential equation

$$\frac{c\sum_{a,s} sn'(a,s,\beta,P)}{1+\sum_{a,s} an'(a,s,\beta,P)} \approx T\left.\frac{\partial P}{\partial T}\right|_{\mu} - P \tag{2.40}$$

can be written to define the pressure as a function of temperature and cluster combinatorials. This differential equation is of central importance in this thesis, since within the validity of Equation 2.36 it allows the construction of a liquid-vapor phase diagram if interference effects are not neglected.

Critical properties of the lattice gas can be evaluated in a standard way calculating the heat capacity at constant volume as a function of temperature along the phase separation line

$$c_V = \left.\frac{\partial u}{\partial T}\right|_V \tag{2.41}$$

and finding its peak at the critical point. Using Equations 2.35 and 2.36, the lattice gas heat capacity can be expressed in terms of the geometric-cluster concentrations in the following way:

$$\begin{aligned} c_V \approx & \frac{c^2}{T^2}\left[\sum_{a,s} s^2 n - t_s \sum_{a,s} sn \sum_{a,s} s^2 n - 2\sum_{a,s} sn \sum_{a,s} asn \right. \\ + & \left. (\sum_{a,s} sn)^2 \sum_{a,s} a^2 n + t_s (\sum_{a,s} sn)^2 \sum_{a,s} asn \right] \end{aligned} \tag{2.42}$$

If cluster concentrations are known beyond the critical temperature, the finite volume approximation may be accurate enough to display the peak whose location can be determined with Equation 2.42 to estimate the critical temperature [5].

---

[5] At and beyond the critical temperature coexistence of phases is lost. However, it does not mean that clusters cease to exist and their concentrations cannot be found. Equation 2.36 offers a prediction to cluster distributions on a certain trajectory in the P-V-T space in the supercritical region. This trajectory necessarily passes through the critical point and is determined only by the fundamental properties of SAPs (numbers of self-avoiding polygons or polyhedra $g_{SAP}(a.s)$). Therefore Equation 2.42 is not *a priori* bound to fail in the supercritical region, but rather is open for testing to determine its range of validity.

2.3 Obtaining Geometric Cluster Concentrations

Simulated geometric-cluster concentrations are obtained from the Ising MC computer runs at different preset temperatures. In this work the two-dimensional zero-field square-lattice Ising model was simulated at temperatures between $T_{min} = 1.5$ and $T_{max} = 2.25$ ($J = 1$) below the critical temperature $T_c \approx 2.269$ using the Wolff algorithm with a computer code courteously provided by Dr. Larry Phair. The temperature points were equidistant with the gap between them $\Delta T = 0.05$.

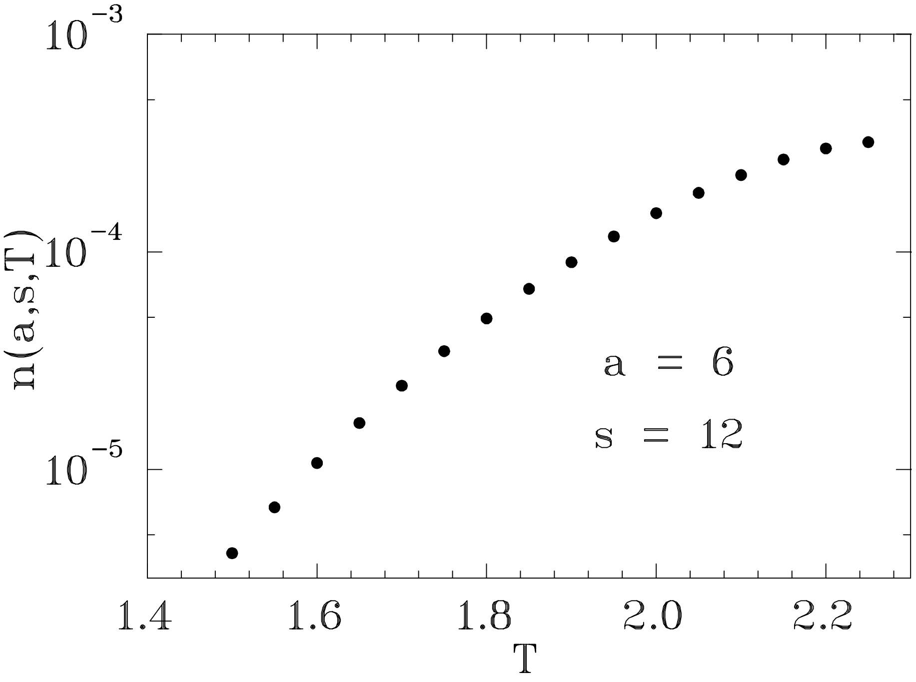

Figure 2.1: Concentration of a geometric cluster at different temperatures. The error bars are too small to be seen.

In the code, Phair employed his own cluster identification routine to tag geometric clusters on every lattice realization to distinguish them as separate clusters. Among other data, the output of the code contained listings of numbered lattice realizations, each of which provided a tagged list of spin coordinates. These listings were then used to reconstruct individual clusters on every realization, and to sort them by size and surface (perimeter). After sorting, numbers of clusters in every size and surface bin were divided by the lattice size and the number of simulated lattice realizations to get the concentrations. An example of a cluster concentration as a function of temperature is shown in Figure 2.1.

2.4 Numerical Analysis of Geometric Clusters

To test applicability of a formalism to geometric clusters, theoretical and simulated cluster concentrations, as well as system's thermodynamics, need to be independently obtained and compared.

2.4.1 Ideal Cluster Gas

Applicability of the ideal-cluster-gas approximation to geometric clusters is presented in Figure 2.2, which shows several simulated concentrations as functions of temperature as compared to equivalent concentrations calculated with Equation 2.11. Comparison of the two data sets reveals reasonable accuracy of the ideal-gas description at low temperatures far below the critical temperature $T_c \approx 2.269$. However, as the temperature of the lattice is increased, Equation 2.11 starts failing and eventu-

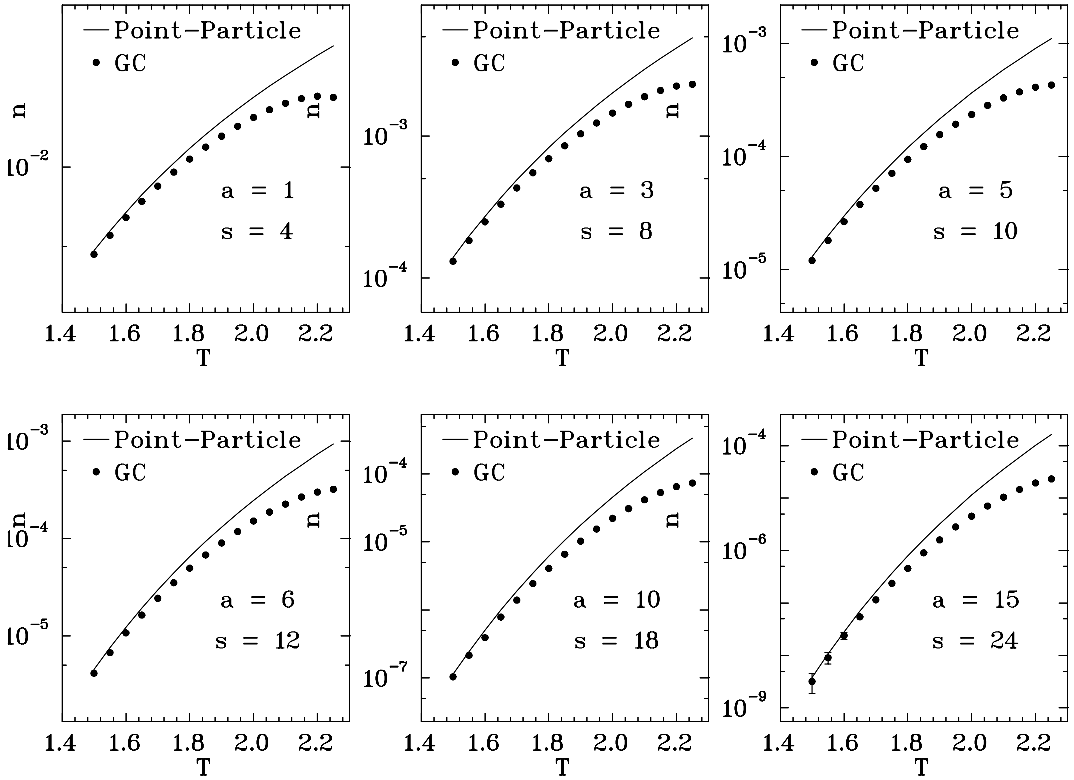

Figure 2.2: Comparison of some geometric-cluster (GC) concentrations with the corresponding theoretical predictions based on the ideal-cluster-gas approximation (Point-Particle).

ally displays large deviations from the simulated data in the vicinity of the critical point. Quantitatively the discrepancy between simulated and theoretical concentrations can be estimated in terms of the cluster-averaged relative deviation, expressed in per cent:

$$\frac{\Delta n}{n} = \frac{100}{\mathcal{N}} \sum_{a,s} \frac{|n(a,s,\beta) - n_{sim}(a,s,\beta)|}{n(a,s,\beta)}, \tag{2.43}$$

where $n_{sim}(a,s,\beta)$ indicates cluster concentrations from the simulation, and $\mathcal{N}$ is the number of cluster types of different size a and surface s used to evaluate the quantity. This statistic is specifically intended to put equal emphasis on large and little clusters alike. Though large clusters are much less numerous than monomers and little clusters, like trimers, and do not play much of a role in overall thermodynamic behavior of the lattice (or fluid in general), they acquire much importance in nuclear cluster analysis applications. As it has been shown in the introduction, only large nuclear clusters can be trusted to convey reliable thermodynamic information. Therefore, when testing properties of geometric clusters as model clusters, large clusters are of primary concern, since their properties determine applicability of analysis techniques to build the phase diagram.

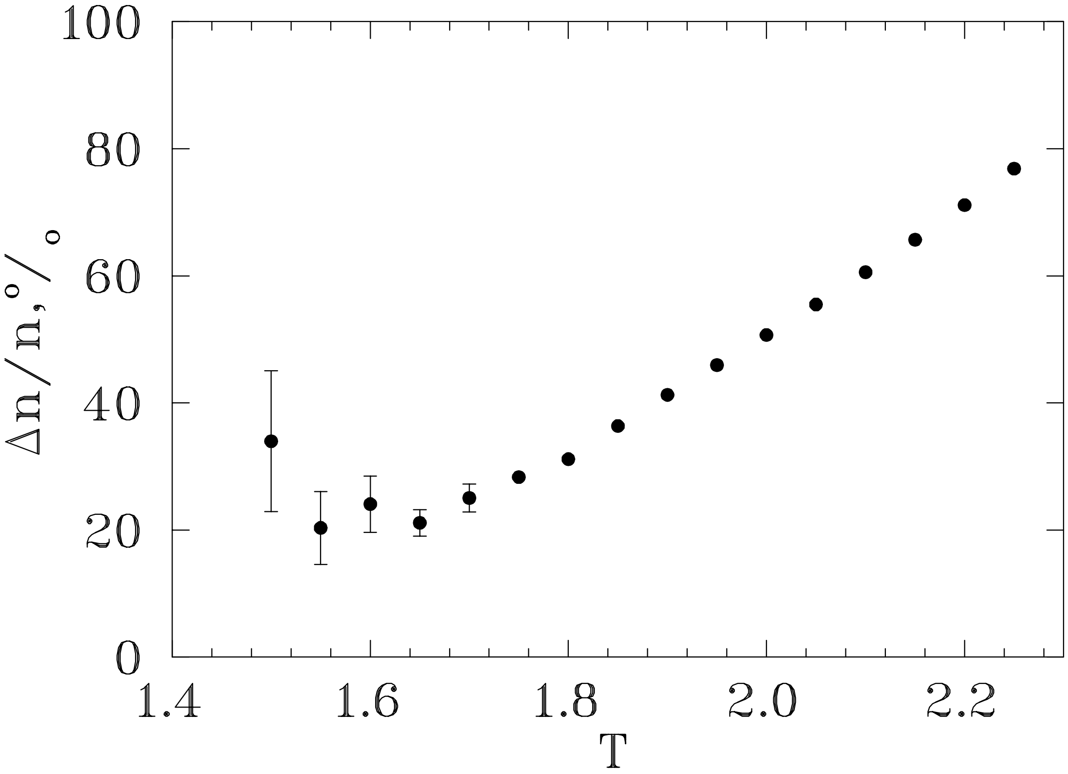

Figure 2.3: The average relative deviation of geometric-cluster concentrations from the predictions of the ideal-cluster-gas model. Clusters up to and including the size $a = 15$ were used.

Unfortunately, the statistic in Equation 2.43 is flawed at low temperatures, where cluster production is predominantly suppressed. The rare multispin clusters, that do form in a limited number of simulated lattice realizations, appear in very small numbers which deviate substantially from the expected averages. As a result, the cluster-averaged relative deviation is dominated by statistical noise, *i.e.* the deviations due to several events (or even one event) of large cluster formation. This can be seen in Figure 2.3 which demonstrates $\Delta n/n$ for a set of clusters with the size up to and including $a = 15$, $\mathcal{N} = 64$ in all. The unexpectedly large deviations in the first three temperature points of Figure 2.3 are dominated by these statistically unreliable data, and should not be paid attention to. Only the data that fall on a straight line should be taken into consideration, and correspond to sampling above the noise.

Overall, at low temperatures Figure 2.3 predicts a small cumulative effect of interference for geometric clusters. However, as the temperature rises, the deviations increase with the temperature to reach 80% around the critical point. This increasing behavior may be explained as a result of increasing pressure of gas in the two-phase mixture. As the temperature increases along the phase boundary curve as shown in Figure 1.10, the amount of liquid decreases, and the amount of gas increases at constant total container volume. The larger the pressure of the gas phase, the stronger the interaction between the gas clusters due to the excluded volume effect. Using the approximation in Equation 2.28 and keeping only the dominant exponential part containing the pressure, the cluster-averaged relative deviation can be roughly estimated as follows:

$$\frac{\Delta n}{n} \approx \frac{100}{\mathcal{N}} \sum_{a,s} 1 - \exp[-\beta P(a + st_s)] \approx \frac{100P}{\mathcal{N}T} \sum_{a,s} (a + st_s) \propto \frac{P}{T}, \tag{2.44}$$

which increases roughly as a sum of cluster concentrations according to Equations 2.29.

Another unbiased test of the approximation can be carried out by comparing the exact SAP combinatorial factors with those obtained by fitting simulated concentrations with Equation 2.11 as a function of temperature. In the fitting of every particular cluster concentration, only $g(a, s)$ is used as a variable parameter. If the fitting formula correctly reflects the properties of the clusters, it is expected to reproduce combinatorial factors of geometric clusters just as they are known from SAP counting. However, incorrect or insufficient models would yield combinatorial factors that systematically deviate from the expected exact numbers. Figure 2.4 demonstrates combinatorial factors for 64 clusters up to and including $a = 15$, obtained using the aforementioned procedure, plotted against the exactly known SAP factors. If the recovered numbers were accurate, the plot would show a one-to-one correspondence evidenced by a straight $y = x$-line. As it is, however, the deviations from the $y = x$-line are fairly large and follow a systematic trend. All the combinatorial factors, that were obtained by fitting, underestimate the exact quantities, and fall on a straight line, indicating the model's failure to reproduce the same property for all the clusters considered. The fact that the extracted combinatorial factors are smaller than those expected from SAPs indicates that the freedom of clusters to take various shapes is suppressed by the presence of other clusters, an effect that the current model cannot account for.

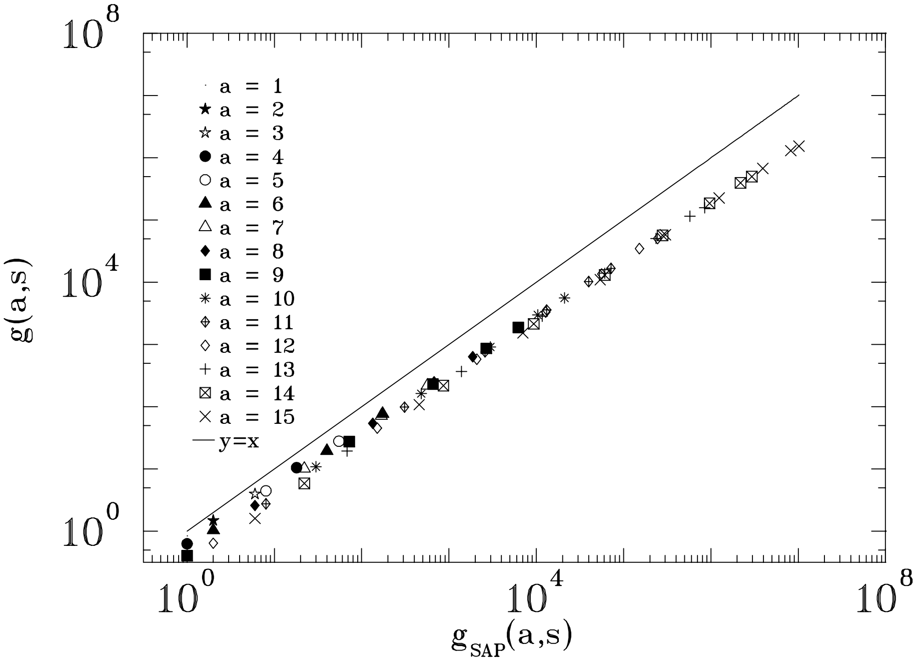

Figure 2.4: Comparison of several SAP combinatorials with the corresponding geometric cluster combinatorials extracted by fitting their concentrations with Equation 2.11.

There is an intriguing possibility of simple linear mapping the wrong combinatorial factors to the right ones. Since the deviations are systematic, and the incorrect combinatorials follow an approximately linear dependence on the true SAP numbers, this dependence can be empirically parameterized by the linear function $y = kx + b$, where k and b are some coefficients. Doing this simple trick yields

$$g_{SAP}(a,s) \approx (3.96 \pm 0.20) g_{\text{ideal}}(a,s) - (1.90 \pm 0.27), \tag{2.45}$$

where $g_{\text{ideal}}(a,s)$ are the combinatorial factors obtained from fitting simulated geometric-cluster concentrations with the ideal cluster gas approximation. This mapping empirically accounts for the effects of cluster interaction on the combinatorial factors of the Ising geometric clusters and prompts the existence of a similar mapping in nuclear systems. Although the knowledge of correct cluster combinatorics does not help finding correct thermodynamics without a proper attention to cluster interaction at every temperature, still these data are important on their own as an indicator of the extent of cluster interference.

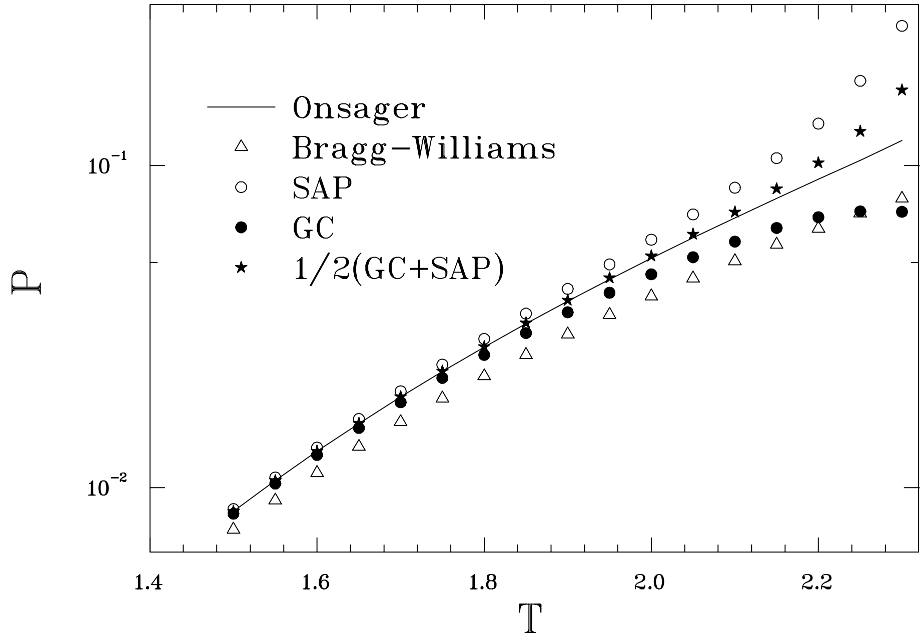

Figure 2.5: The lattice gas coexistence pressure in the limit of the ideal cluster gas calculated with geometric-cluster concentrations from simulations (solid circles), and using Equation 2.11 (open circles), as compared to the exact pressure (line). The solid stars depict the average of the two pressures. The mean-field Bragg-Williams pressure is also shown as open triangles.

Thermodynamics of the lattice gas at the phase boundary can also be used to test the accuracy of the non-interacting-cluster method. As an example, pressure can be found within the ideal-cluster-gas approximation using Equations 2.29. At the same time, the exact pressure P can be found from the Onsager solution using the equivalence relations in Table 1.12. If the ideal-cluster-gas approximation is good for geometric clusters, it should yield the lattice gas pressure just as Onsager predicts it or close to it. Otherwise the poor correspondence would be indicative of an inadequate methodology. In addition to that, the two possible independent methods to calculate the pressure using an ideal gas of clusters should produce consistent results. According to the first method, cluster concentrations from MC simulations can be summed up at specified temperatures using Equations 2.29. In the second method, Equation 2.11 can be used at the same temperatures to predict the concentrations of geometric clusters as if they were non-interacting, and then these concentrations can be accordingly summed up. Both methods are expected to produce equal results, comparable with the exact pressure. However, the expectations are not fulfilled, as the results of the calculations are shown in Figure 2.5. The pressure according to the first approach is abbreviated GC (geometric clusters), according to the second approach the pressure is called SAP, and the exact pressure is called Onsager. Predictions of the zeroth order mean-field Bragg-Williams approximation are also shown in the figure. Notice that the Bragg-Williams approximation is the worst among all shown in the figure thereby giving a credit to the ideal cluster gas approximation as of a higher order compared to the mean field. Nevertheless, it can be observed with certainty that the ideal-cluster-gas approximation still applies poorly to geometric clusters unless the temperatures are low. At high temperatures and in the vicinity of the critical temperature the deviations are of the order of 30% with the two methods yielding inconsistent results which bend off the exact pressure in opposite directions. The Bragg-Williams approximation is more or less consistent with the first method of calculating the pressure directly from the simulated cluster concentrations indicating that the non-interacting-cluster technique is more than sufficient to obtain rough estimation of mean-field thermodynamics of the system. However, at certain conditions these thermodynamics can significantly deviate from the exact values, and may not be very helpful. These deviations are the result of the cluster interaction, which needs to be accounted for in order to correctly reproduce fluid's thermodynamics from the observed cluster distributions.

An interesting result, shown in the same figure, concerns the pressure obtained by averaging GC and SAP pressures. It can be seen that this average pressure comes fairly close to the exact Onsager's calculation thus allowing for a simple recipe to estimate the true pressure and the extent of the finite volume effects in the system. This is another empirical result that combined with the empirical parameterization in Equation 2.45 may provide a simple test procedure for probing a system on account of cluster interference. Again one should have nuclear clusters in mind for the potential use of these simple tricks as preludes to the full-fledged Stillinger-like analysis methodology.

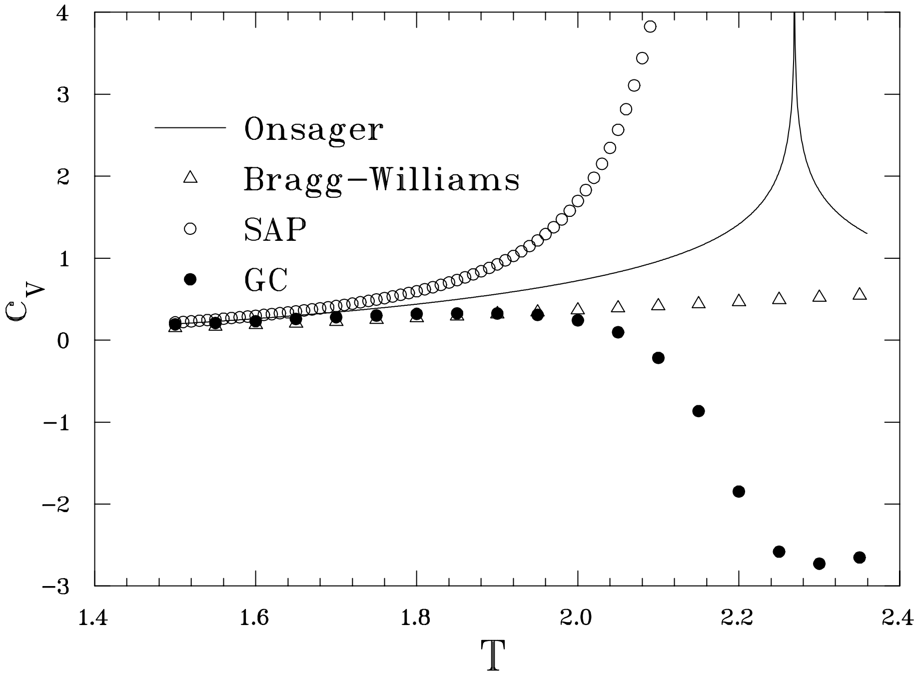

Figure 2.6: The lattice gas coexistence heat capacity in the limit of the ideal cluster gas calculated with geometric-cluster concentrations from simulations (solid circles), and using Equation 2.31 (open circles), as compared to the exact heat capacity (line). The heat capacity according to Bragg-Williams is also plotted.

Critical properties of the lattice gas cannot be obtained from geometric clusters as an ideal gas using the heat capacity. The demonstration of this fact can be seen in Figure 2.6, which offers a comparison of the exact lattice gas heat capacity along the phase boundary line with the approximate ideal-cluster-gas heat capacities calculated using Equation 2.31 in two previously discussed ways. In addition to that, the heat capacity according to Bragg-Williams mean-field approximation is also presented. To conduct this test, the temperature range of the Ising MC simulations was extended to $T_{max} = 2.35$. Not surprisingly, the figure shows no consistency of the results, and no result comes close to the exact heat capacity depicted by the solid line. The heat capacity, designated SAP and calculated using self-avoiding-polygon combinatorics, diverges quickly prompting the existence of a different critical point for the hypothetical ideal gas of geometric clusters located at about $2.06J$, which is quite far from reaching the exact critical point of the lattice gas at $T_C \approx 2.269$. Without certainty, this suggests that the critical temperature of the lattice gas is significantly influenced by cluster interference, and that without interference, as is the case in the hypothetical ideal gas of geometric clusters, the critical temperature is reduced. On the other hand, the heat capacity called GC is calculated using geometric cluster concentrations obtained directly from the MC simulations. Instead of showing a peak in the positive range, this heat capacity dips toward the negative range around the critical point and is, therefore, non-physical. In contrast, the Bragg-Williams heat capacity is relatively flat in the critical region, indicating the lack of the critical information.

2.4.2 Non-ideal Cluster Gas

Numerical tests with geometric clusters as a non-ideal gas can be carried out in the same manner as the one offered to check applicability of the ideal-cluster-gas approximation. Figure 2.7 presents a qualitative comparison of simulated geometric-cluster concentrations with the analytically assessed predictions of the finite volume approximation (FVA) in Equation 2.28. It can immediately be seen that the deviations are barely visible. A more thorough comparison is shown in Figure 2.8, in

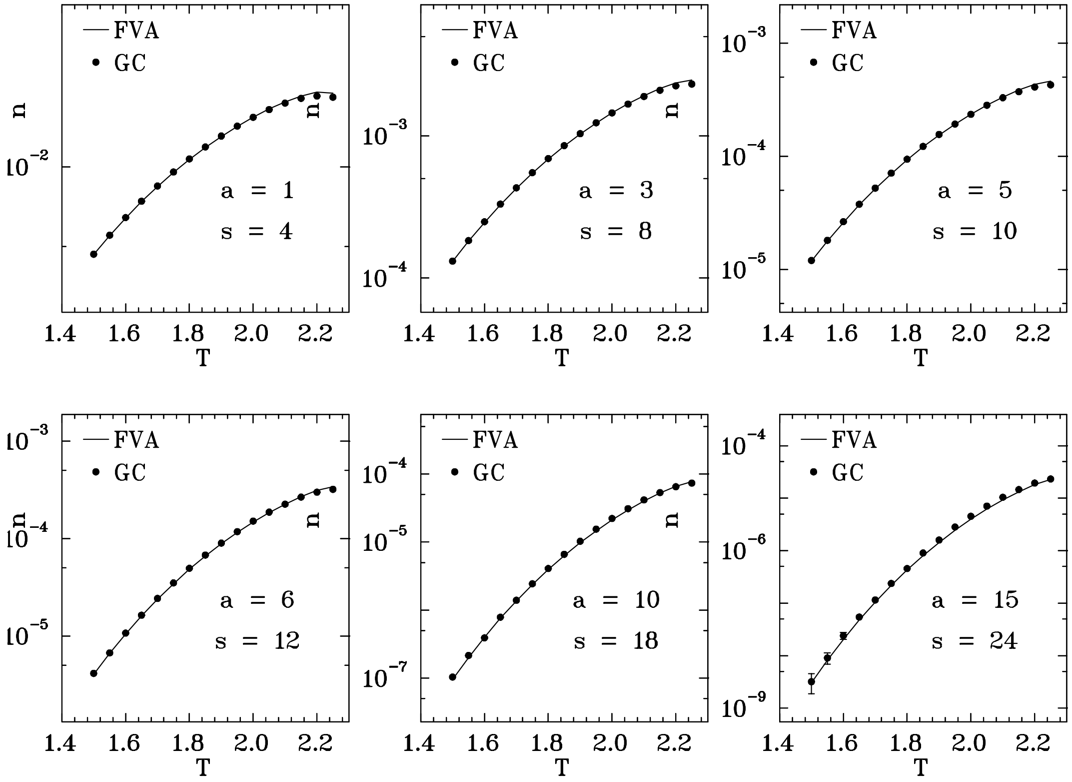

Figure 2.7: Comparison of some geometric-cluster (GC) concentrations with the corresponding theoretical predictions by Equation 2.28.

which average relative deviation, calculated with Equation 2.43, is demonstrated in per cent as a function of temperature for 64 clusters up to $a = 15$. No doubt, this figure displays a dramatic improvement over a similar plot in Figure 2.3, which refers to the ideal-cluster-gas approximation. Apart from fluctuations at low temperatures due to poor statistics of large clusters, the deviations do not exceed 7-8% and are not temperature dependent. Notice how the divergent temperature dependence is annulled using the finite volume approximation, and the deviations stay constant throughout the whole temperature region under consideration. These constant de-

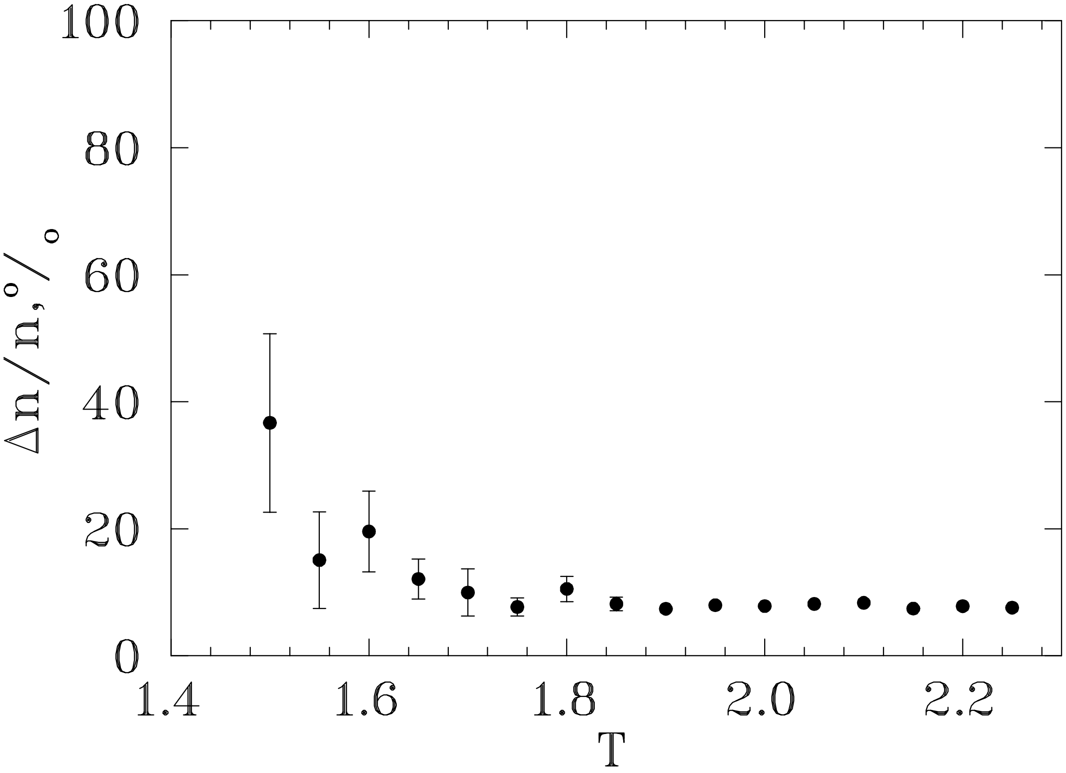

Figure 2.8: The average relative deviation of geometric-cluster concentrations from the predictions of the finite volume approximation.

viations point to systematic errors due to insufficient accuracy of FVA. It must be emphasized, however, that the extreme simplicity of FVA, which is based on the one-dimensional Reiss-Frisch-Lebowitz (RFL) approximation, makes it quite surprising to see deviations so insignificant. Clearly, the more complex two and three dimensional RFL approximations will be able to render the observed discrepancies almost non-existent.

Pleasing results also come when extracting SAP combinatorics [6] from simulated

---

[6] This technique of estimating numbers of SAP may be used as an alternative to exact counting methods in three and higher dimensions when the exact methods fail due to the limited computer power. Even with the power of modern supercomputers, SAP enumeration in two dimensions is limited by the size $a = 50$. In higher dimensions exact calculations cannot break the $a = 20$ limit.

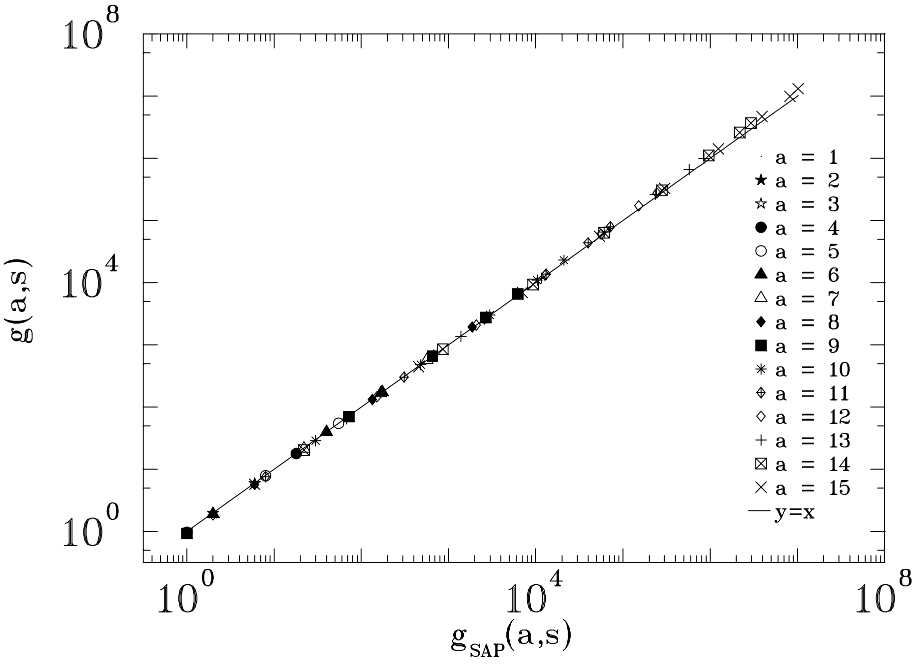

Figure 2.9: Comparison of SAP degeneracies with geometric cluster degeneracies extracted by fitting their concentrations with finite volume approximation in Equation 2.28

concentrations using Equation 2.28. Figure 2.9 shows almost one-to-one correspondence between the exact and calculated combinatorial factors spanning eight orders of magnitude, with only small deviations appearing at large values. The inconsistencies can better be seen in Figure 2.10, in which relative deviations are plotted versus exact values. In the plot it may be noticed that up to the values in the fifth order of magnitude the deviations from the exact numbers do not exceed several per cent. These combinatorials correspond to small and/or relatively compact clusters for which the surface contribution to the cavity volume and free energy is approx-

---

However, MC Ising simulations can be carried out fairly easily and quickly for very large lattices with high statistics. Using approximations to cluster concentrations, like FVA or better, reliable SAP combinatorics may be obtained with a small cost [Breu 04].

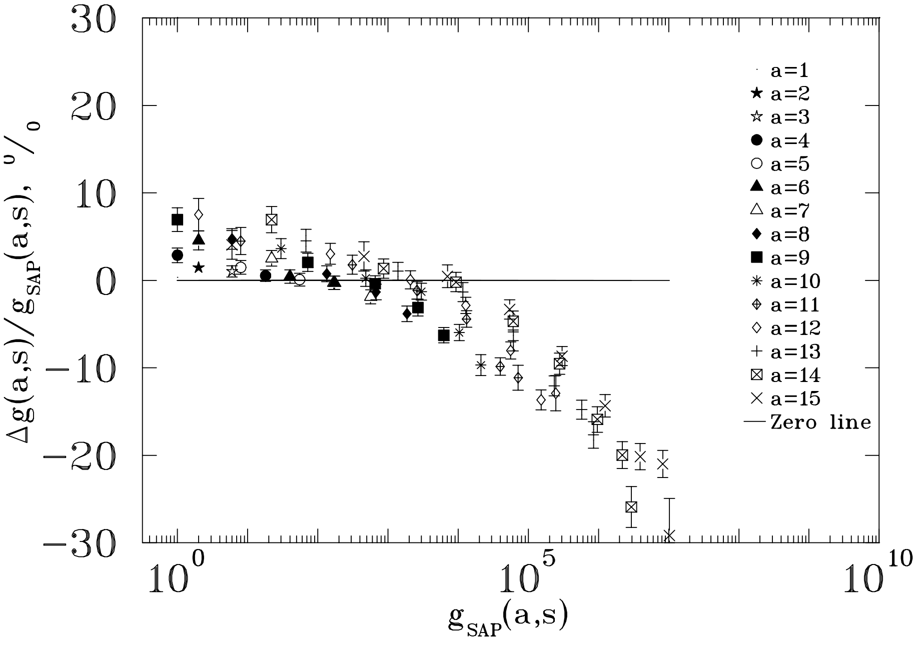

Figure 2.10: Relative deviations of geometric cluster degeneracies from exact SAP degeneracies. Finite volume approximation in Equation 2.28 has been used to fit geometric cluster concentrations obtained from MC Ising simulations.

imated accurately by FVA. On the other hand, large combinatorials correspond to stringy clusters that have extremely convoluted surfaces with many bends in the strings. The estimation of the cavity volume $v(a,s)$ is imprecise for these clusters, which also require higher order of RFL approximation used to describe the surface effects on the cavity formation free energy.

The lattice gas thermodynamics can be obtained using FVA with the differential equation technique (DET) according to Equation 2.37. The use of DET to analyze the cluster concentrations obtained directly from the simulations is bound to be accurate, since FVA is not needed, and the lattice energy is accurately calculated as shown in Equation 1.54. The error is only due to the incomplete set of lattice

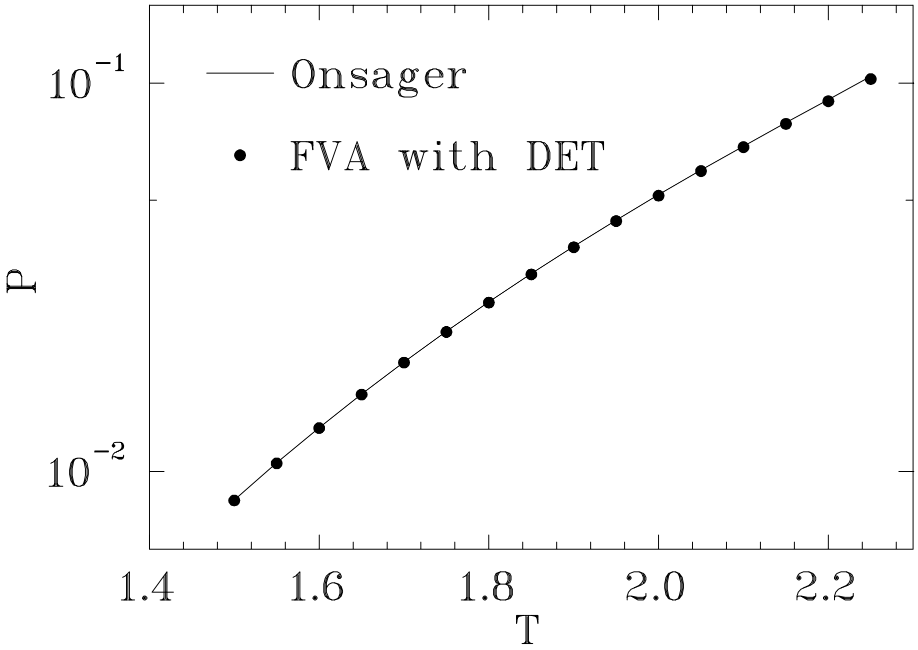

Figure 2.11: The lattice gas pressure calculated from SAP combinatorial factors assuming non-ideal cluster gas (solid circles). The line represents Onsager's pressure.

realizations and cluster sizes explored in the simulations. Therefore, it is only of interest to learn how FVA can be used to describe the lattice gas with a finite set of SAP combinatorials, since in possible real-life application of this technique to nuclear clusters the knowledge of combinatorial factors is of central importance. First-order differential Equation 2.40 can be solved numerically to find the pressure from the limited distributions $g_{SAP}(a, s)$. Matlab was employed to program the algorithm on a computer. The code is presented in Appendix A. Figure 2.11 shows the result of the calculation in two dimensions using 877 SAP combinatorials up to and including $a = 50$. The agreement with the exact pressure is remarkable with the largest deviation being 1.53% at $T = 2.25$.

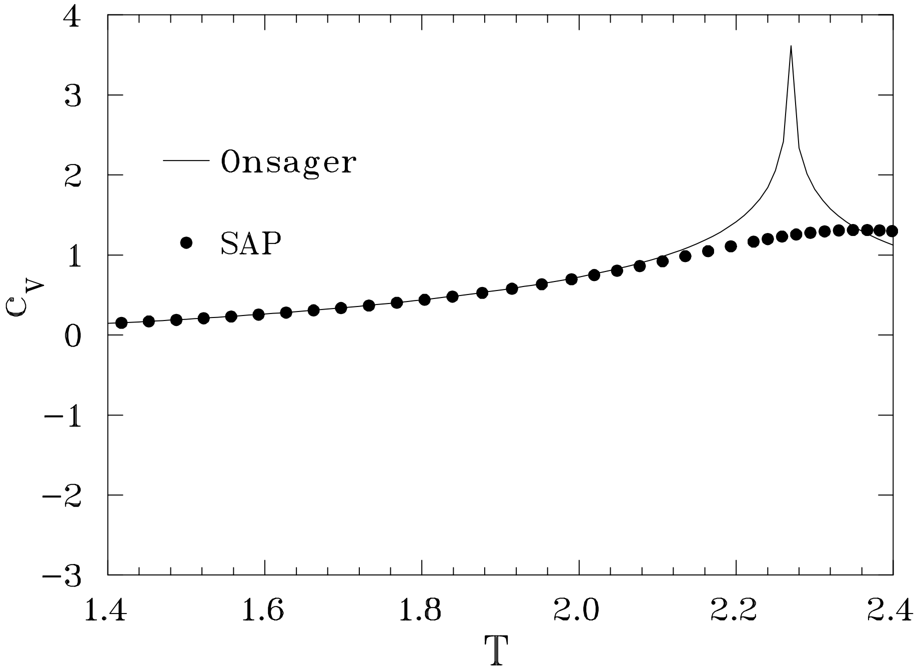

Figure 2.12: Heat capacity of the two-dimensional Ising model calculated using SAP combinatorials (solid circles) and from the Onsager solution.

The critical point can be estimated from the peak in the heat capacity using Equation 2.42. Again the 877 SAP combinatorials are used to obtain the results presented in Figure 2.12 in comparison with exact Onsager's result. The expectation of non-divergence of the heat capacity is readily confirmed in the figure. A small but clearly visible peak occurs that provides the estimation of the critical temperature at $T_c \approx 2.358$. At first glance the deviations from the exact result seem to be fairly large. Nevertheless, the methodology should be given much credit. Notwithstanding the simplicity of FVA, and truncation of SAP distributions used for the calculation, there is a large improvement in comparison with the ideal-cluster-gas calculation. In spite of weak comparison to the exactly known lattice gas heat capacity, the finite volume approximation correctly reproduces the expected properties of the fluid, while the estimation of critical temperature deviates from Onsager's only by 4%.

2.5 Conclusions

It has been demonstrated on the basis of a simple RFL approximation, that geometric clusters of the Ising model behave like Stillinger's clusters, and are capable of accurately recovering thermodynamics of the lattice gas. On the other hand, the ideal-cluster-gas approach to geometric-cluster analysis yields worse results completely failing in the vicinity of the critical temperature. Therefore, geometric clusters may be accepted as proper model clusters to test and develop nuclear cluster analysis techniques if cluster interference is duly accounted for.

The ultimate test for applicability of Stillinger's formalism to nuclear clusters lies only with the experiment. However, the observed success of geometric clusters as a non-ideal gas, especially in the vicinity of the critical point, to correctly reveal the properties of the lattice gas hints at the possibly similar properties of nuclear clusters. If these expectations are true, then the failure of the ideal-cluster-gas approximation to correctly recover the lattice gas pressure from the geometric-cluster gas casts a doubt on the previously conducted nuclear analyses, and produces a motivation to search for alternative techniques.

The first easy step in such a search is to modify previously used Fisher's model to accommodate the effects of cluster interference and to employ the differential equation technique to analyze nuclear cluster distributions. In fact, to make a connection between nuclear and lattice clusters, Fisher's model is only needed to parameterize cluster combinatorials and surfaces as functions of cluster size. Then the energy of the nuclear gas phase at the phase boundary may be estimated as a sum over surface energies of individual clusters, and the pressure may then be inferred from the energy by solving a differential equation similar to Equation 2.40. Since experimental cluster distributions are incomplete, the above technique should be coupled with a fitting procedure to determine the best estimate of the parameters, and reconstruct the missing cluster distributions. The pressure, density and all the other thermodynamic quantities can then be determined from the modified Fisher-like analytic concentrations. The next chapter considers this methodology in detail.

Chapter 3

Interacting-Cluster Approach to Nuclear Cluster Analysis

The success of Stillinger's methodology in estimating the lattice gas pressure at coexistence prompts a question: can it be successfully carried over to Fisher's droplets and eventually to nuclear clusters? Apart from incomplete nuclear cluster data, the need to use Fisher's model is dictated by the lack of experimental information about the particular surface area of a nuclear cluster at the moment of detection. Section 3.1 will deal with these issues by introducing the Modified Fisher's model, which accounts for effects of cluster interference and nicely avoids the need to use cluster surface areas. Application of the modified Fisher's model to data will be considered in Section 3.2, and Section 3.3 will present final conclusions.

3.1 The Modified Fisher's Model

A modified [1] Fisher-based analysis procedure, which includes cluster interference effects, can be obtained by substituting cluster surfaces and combinatorial factors in the Stillinger-based formalism with the corresponding Fisher's parameterizations. However, the original Fisher's parameterizations did not sufficiently account for fractality effects. Fractality is a property of some shapes to be self-similar with a change of scale. Fractals will be discussed more thoroughly after this brief introduction, but now it is important to say that fractality effects may play a significant role comparable to or even larger than that of cluster interference. And since the finite volume approximation (FVA) claims a significant improvement in accuracy over the ideal-cluster gas methodology, avoiding consideration of fractality can undermine the overall usefulness of Stillinger-based approach to cluster analysis using Fisher's model.

---

[1] Finite volume effects in Fisher's model have been considered in the past. Swaminathan and Poland [Swam 78] used the results of the three-dimensional RFL theory to combine them with Fisher's concentrations. In addition to that they developed a methodology to predict individual cluster concentrations from known Fisher's parameters. Their approach to introduce finite volume effects into Fisher's concentrations is essentially the same as the one in this work. However, their methodology to analyze a fluid is more general and complex involving a non-linear system of equations, the number of which is equal to the number of cluster types, whereas this thesis considers a particular case of phase coexistence offering a rather simple and novel technique, refined on the basis of geometric clusters. The modification of Fisher's model by Swaminathan and Poland was never used in nuclear cluster analysis.

3.1.1 Fractality Effects in Fisher's Parameterizations

Fractality [Fede 88, Schr 91] is the property of an object to repeat its unique form and structure in the form and structure of the building blocks used to create the object. In other words, the form and structure of the bricks is repeated in the form and structure of the building, which is repeated in the form and structure of the city, and so on. In the words of Mandelbrot, who introduced fractals into the modern physics [Mand 82], "a fractal is a shape made of parts similar to the whole in some way" [Fede 88].

Fractal shapes are distinguished from non-fractal ones by the fact that their dimensionality is different from the dimensionality of the space they form in. Fractality can be characterized by a fractal dimension. For non-fractals it coincides with Euclidean topological dimension of the space, whereas for fractals it is non-integer and differs from the space dimension. Fractal dimension is defined as a ratio of the logarithm of the number of building blocks that can fit into a composite object, to the logarithm of the change of scale between the scales (magnification factor) of the composite object and its building blocks. For example, the fractal dimension of a square is calculated to be two, since it can contain four squares twice as small. The fractal dimension of a cube is three. Therefore a square and a cube are not fractals. On the other hand, the fractal dimension of Sierpinski triangle, shown in Figure 3.1, is $\log 3/\log 2 \approx 1.58$, which is quite different from the topological dimension of the two-dimensional space. Sierpinski triangles are fractal objects.

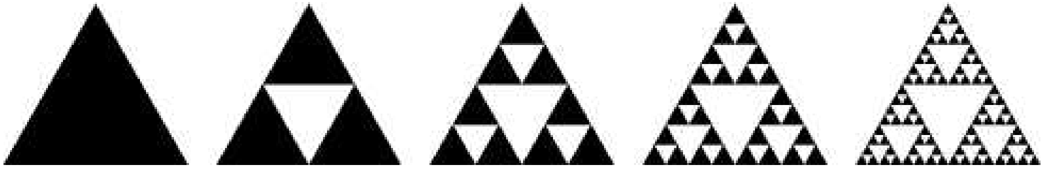

Figure 3.1: Sierpinski triangle.

Clusters also possess fractality due to irregularity of their shapes with the exception of cubes, squares, strings and some other non-fractal shapes that clusters can take on. Every one of those shapes is characterized by a unique fractal dimension, at times exceedingly different from the topological dimension. As a result, fractality in clusters strongly affects the relationship between the volume and surface of clusters. In fact, for an arbitrary cluster of a particular size the relationship is not unique, like for a cube or a sphere. Nevertheless, for a group of clusters of a particular size, a connection between the volume and average surface can be conjectured, which also gives proper attention to fractality effects. In his original work [Fish 67, Fish 69], Fisher accounted for cluster fractality introducing a formula similar to the surface-volume relationship of simple shapes, but with the exponent including an effective fractal dimension of the cluster surface instead of its topological dimension:

$$\overline{s} = \kappa a^{\sigma}, \tag{3.1}$$

where $\overline{s}$ is the average surface of a cluster of size a, σ is the ratio of an effective fractal dimension of the average cluster surface to the topological dimension of the cluster volume, and κ is a proportionality coefficient. This formula, however, is too much of an approximation. Stauffer [Stau 75, Stau 79] presented a convincing argument that the average cluster surface on the lattice splits in two parts. One part is proportional to a power of the cluster volume and the other part is proportional to the volume itself. Though Stauffer did not mention fractality as a reason for such a relation, clearly this effect must be due to fractality as the cluster surface may be extremely convoluted. In the extreme when the surface fills the whole cluster volume in the spiral-like arrangement, the surface area becomes only proportional to the volume. As an example, imagine a sheet of aluminum foil, say 1 ft^2. This fairly large sheet can be wrinkled and pressed into a small sphere. Clearly, at constant thickness of the foil, the mass (and the volume) of the sphere will be proportional to the actual surface area of the foil in the sphere (which is 1 ft^2), whereas the use of the standard surface-volume relationship of the sphere will yield grossly incorrect estimation of the foil's surface. So it is with clusters. Two-dimensional geometric clusters can be presented as a simple example to clarify the issue. The most compact non-fractal clusters are squares, whose surface (perimeter) goes exactly as the volume to the power 1/2. In the other extreme, geometric clusters can form spirals and strings, whose surface goes exactly linearly with the cluster volume because it fills up the volume (the fractal dimension of such a surface approaches the topological dimension of the volume). All other clusters take some intermediate position with respect to these two extremes and have both contributions to their average surface. Therefore, according to Stauffer, it seems more fitting to express the average cluster surface as a superposition of the two extreme (compact and convoluted) contributions:

$$\overline{s} = \kappa[a^{\sigma} + la], \tag{3.2}$$

where l is a constant.

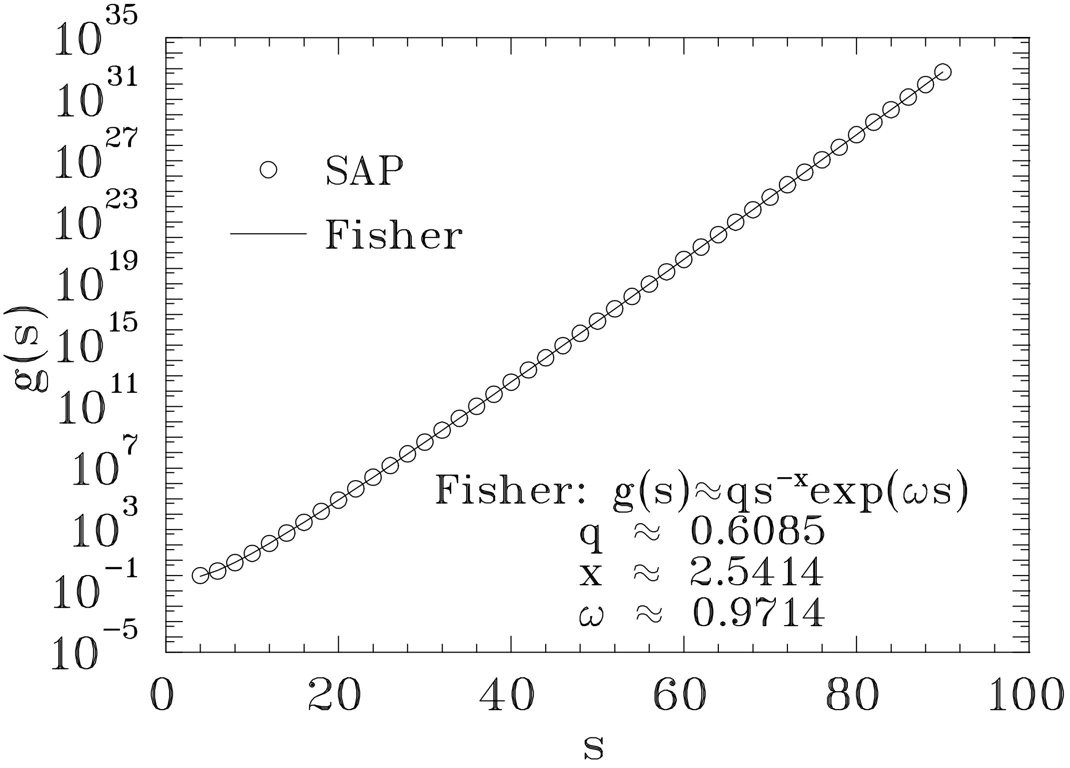

Figure 3.2: Comparison of the exact perimeter dependent SAP combinatorial factors to the fit with Fisher's asymptotic in Equation 3.3.

Different expressions for the average cluster surface as a function of the cluster size should necessarily affect Fisher's parameterization of the combinatorial factor. Fisher's original parameterization for this quantity is

$$g(\overline{s}) \approx q\overline{s}^{-x}\exp(\varpi\overline{s}), \tag{3.3}$$

where g is the cluster combinatorial factor, and q, x, and ϖ are some constants. It is based on an asymptotic empirically found [Rush 59, Fish 59] in the 1950s for numbers of polygons and random walks on the lattice and later confirmed semi-analytically [Fish 59]. This asymptotic is extremely accurate when applied to the number of self-avoiding polygons as a function of their perimeter (the analogy to the surface area in two dimensions). In Figure 3.2 the exact numbers of SAPs [Jens 03] are compared to the fit with Equation 3.3. Over the range of thirty five orders of magnitude the correspondence is blameless, and holds a promise to remain blameless for any perimeter size. Recent studies [Brak 90, Lin 91, Bous 96, Gutt 00, Jens 00, Gutt 01] confirmed the earlier work by analytically calculating the numbers of a limited class of self-avoiding polygons (convex and row-convex polygons), deriving the asymptotics and testing the results on modern computers. They demonstrated that Equation 3.3 is a good approximation to the true combinatorial factors.

Fisher further assumes the validity of Equation 3.1 and postulates that

$$g(a) \approx q_0 a^{-\tau} \exp(k a^{\sigma}), \tag{3.4}$$

where $q_0 = q\kappa^{-x}$ and $k = \varpi\kappa$. This parameterization, however, does not account for the proportionality of the average cluster surface to the volume of the cluster. Therefore, it seems reasonable to improve upon Fisher's asymptotic in Equation 3.4 by adopting Stauffer's parameterization of the average cluster surface and keeping the general form of Equation 3.3 unchanged:

$$g(a) \approx q_0 [a^{\sigma} + la]^{-x} \exp(k[a^{\sigma} + la]) \tag{3.5}$$

This form is expected to account for the fractality effects of average cluster surfaces more accurately by separately considering the non-fractal surface and volume contributions. Since Equation 3.5 implies σ to be a non-fractal surface part, the value of this quantity may be taken as a ratio of topological surface and volume dimensions. For example, in two dimensions

$$g(a) \approx q_0[a^{1/2} + la]^{-x} \exp(k[a^{1/2} + la]) \tag{3.6}$$

In the rest of this work σ will no longer be considered as a parameter, but will be fixed according to the dimensionality of the problem.

3.1.2 The Modified Fisher's Droplet Concentrations

In Chapter 2 it was demonstrated that geometric clusters of the Ising model obey Stillinger's theory. An approximation was introduced to describe cluster concentrations in the limit of RFL (Reiss, Frisch, Lebowitz) spheres in one dimension, which produced very good agreement with the results obtained from two-dimensional Monte Carlo Ising simulations. This encouraging outcome prompts a development of a similar Fisher-based methodology to analyze nuclear cluster data with its inherent limitations of incompleteness and lack of surface information. The starting point in this endeavor is the finite volume approximation adopted in Chapter 2:

$$n(a, s, \beta, P, \rho) \approx g(a, s) \exp(-c\beta s) \exp[-\beta P(a + t_s s)](1 - \rho), \tag{3.7}$$

where here $g(a, s)$ will denote combinatorial factors of nuclear clusters. In order to obtain the modified Fisher's concentrations, Equation 3.7 must be first summed up over the cluster surfaces to yield the size dependent concentrations:

$$n(a, \beta, P, \rho) \approx \exp[-\beta P a](1-\rho) \sum_{s} g(a, s) \exp(-c\beta s) \exp[-\beta P t_s s] \tag{3.8}$$

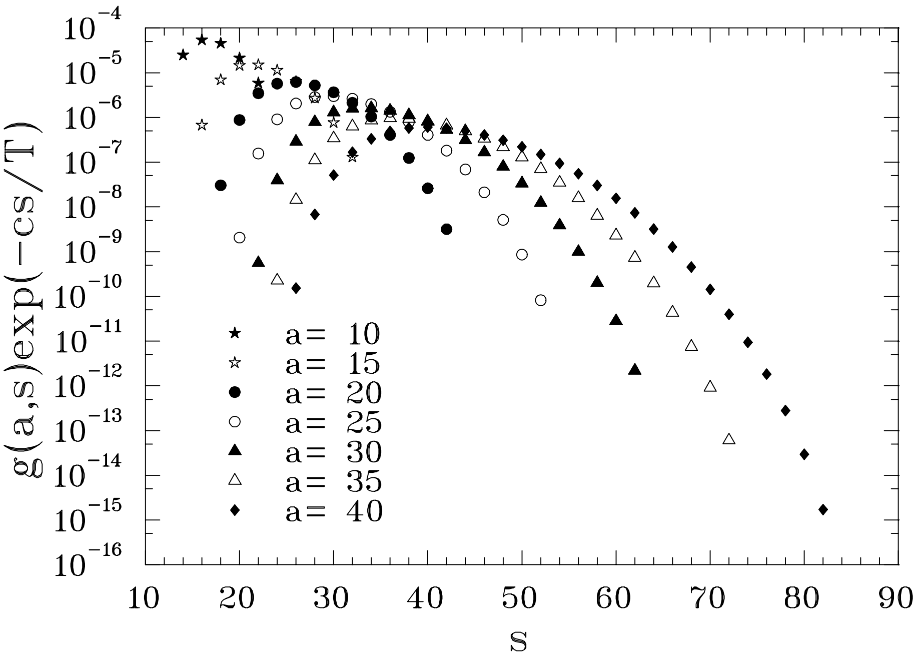

Figure 3.3: The basis for Fisher's conjecture in Equation 3.10 using the example of SAP. In this example $T = 2$. The pressure dependent part does not change the overall picture, and was omitted in this calculation.

According to Fisher's arguments, the sum in Equation 3.8 is strongly dominated by one term, and can approximately be substituted by this term, which corresponds to the most probable surface $\overline{s}[\beta]$:

$$\overline{s}[\beta] = \frac{\sum\limits_{s} s g(a, s) \exp(-c\beta s) \exp[-\beta P t_s s]}{\sum\limits_{s} g(a, s) \exp(-c\beta s) \exp[-\beta P t_s s]} \tag{3.9}$$

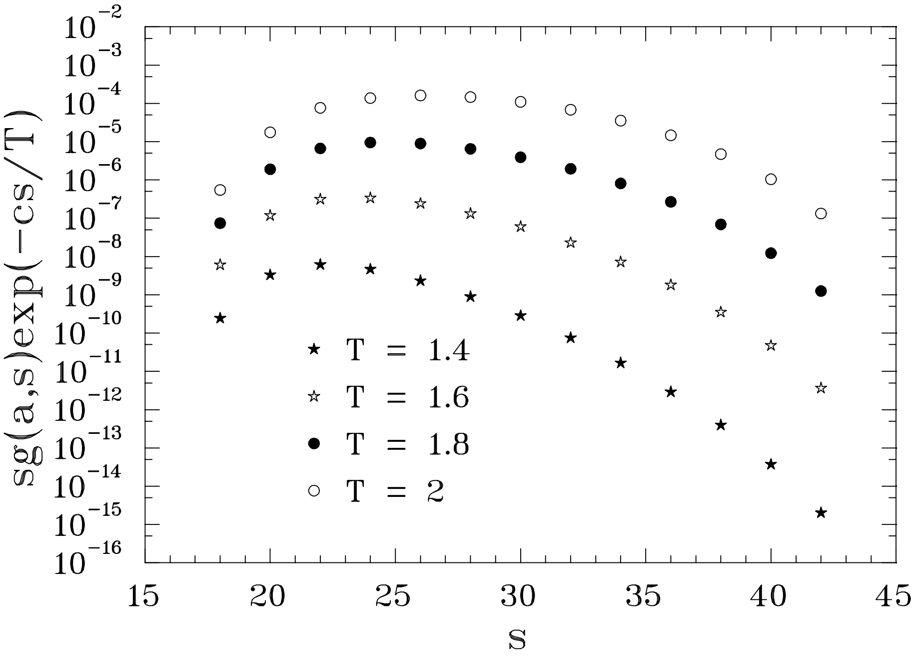

Figure 3.4: The basis for Fisher's conjecture in Equation 3.12 regarding the temperature. SAPs of size $a = 20$ are used as an example. The pressure dependent part does not change the overall picture, and was omitted in this calculation.

Therefore, the sum is

$$\sum_s g(a,s)\exp(-c\beta s)\exp[-\beta P t_s s] \approx g(\overline{s}[\beta])\exp(-c\beta\overline{s}[\beta])\exp[-\beta P t_s\overline{s}[\beta]] \quad (3.10)$$

This approximation has a good confirmation in the properties of self-avoiding polygons. Figure 3.3 depicts the summand (without the pressure dependent part, which does not alter the picture) for various SAP sizes at a fixed temperature below the critical Ising temperature as a function of SAP surfaces (perimeters). The peaks are clearly seen. Therefore, the size dependent cluster concentrations may be written as

$$n(a,\beta,P,\rho) \approx g(\overline{s}[\beta])\exp(-c\beta\overline{s}[\beta])\exp[-\beta P(a+t_s\overline{s}[\beta])](1-\rho), \quad (3.11)$$

where $g(\overline{s}[\beta])$ is the combinatorial factor of a cluster of size a at the most probable surface corresponding to an inverse temperature β. Fisher argues that this temperature dependence is not strong and is dominated by the maximum temperature in the interval of consideration. This point can be demonstrated by writing the temperature averaged most probable surface of a cluster of size a:

$$\overline{s} = \frac{\int_{\beta_1}^{\beta_2} \overline{s}[\beta] g(\overline{s}[\beta]) \exp(-c\beta\overline{s}[\beta]) \exp[-\beta P t_s \overline{s}[\beta]]}{\int_{\beta_1}^{\beta_2} g(\overline{s}[\beta]) \exp(-c\beta\overline{s}[\beta]) \exp[-\beta P t_s \overline{s}[\beta]]} \approx \overline{s}[\beta_2] \qquad (3.12)$$

The integrals in Equation 3.12 are also expected to be strongly peaked at a temperature corresponding to the maximum temperature in the range $[\beta_1 : \beta_2]$. Therefore, the most probable surface $\overline{s}$ can be assumed to be a function of the maximum temperature in the range being explored: a constant as far as the range is fixed. The confirmation to this assumption is readily furnished by SAPs. In Figure 3.4 surface area distributions for a polygon of a fixed size are shown at different temperatures. Clearly, the peaks of these distributions are separated by orders of magnitude, with the peak at the highest temperature being about fifteen times higher than the peak at a temperature different only by ten per cent. Therefore, the δ-function approximation for the integrals in Equation 3.12 seems quite fitting.

With the most probable surface $\overline{s}$ assumed to be a constant within the chosen temperature range, the modified Fisher's concentrations at coexistence can be expressed according to Equations 3.2, 3.3, and 3.5 as follows:

$$n(a, \beta, P, \rho) \approx q_0[a^\sigma + la]^{-x} \exp([k - c_0\beta - t_s\kappa\beta P][a^\sigma + la]) \exp(-\beta P a)(1-\rho), \quad (3.13)$$

where $c_0 = c\kappa$. Equation 3.13 represents the form, that may be further used in the analysis of experimental data.

3.1.3 The Coexistence Condition and the Linear Terms

Introduction of the linear terms la in the parameterization of the average cluster surface $\overline{s}$ demands a justification at the liquid-gas coexistence. The matter is that at coexistence the transfer of clusters between the phases is not characterized by the change of the volume part of the free energy (change of the chemical potential is zero), and for that reason the volume dependent terms in the exponential part of Equation 3.13 are expected to vanish. This criticism is valid, and no rigorous justification for retaining the linear terms is offered at this time. Nevertheless, some comments can be offered to alleviate the problem.

It is important to say that the coexistence condition is not enforced in the methodology described in this thesis. When cluster interaction is introduced through the free energy contribution $-\beta W$ due to the cavity formation, this contribution also changes with the chemical potential difference $\Delta\mu$ of the phases. Therefore, with interaction included, modified Fisher's concentrations can be written in the following general form:

$$n(a,\beta) \approx q_0[a^\sigma + la]^{-x} \exp(ka^\sigma - c_0\beta a^\sigma + kla - c_0\beta la)\exp(\beta\Delta\mu a)\exp(-\beta W[\Delta\mu]), \tag{3.14}$$

for which enforcing the coexistence condition $\Delta\mu = 0$ requires the explicit knowledge of the $W[\Delta\mu]$ dependence. In the formalism presented in this thesis, coexistence is implied by putting $\Delta\mu = 0$ in the ideal part of Equation 3.14 and considering the temperature-only dependence of all the quantities involved in the analysis, so that the thermodynamic quantities are evaluated with the relation

$$u = T\left(\frac{\partial P}{\partial T}\right)_{\mu} - P, \tag{3.15}$$

which is used to calculate the pressure through the average energy per particle u of the system. The $\Delta\mu$-dependence of the cavity free energy, however, is not identified, but rather it is expected to be inferred from the experimental cluster distributions.

The simple approximation for cavity formation free energy

$$-\beta W[\Delta\mu = 0] \approx -\beta P[\Delta\mu = 0] v_{cavity} + \ln(1 - \rho[\Delta\mu = 0]), \tag{3.16}$$

adopted in this work, where v_{cavity} is the volume of the cluster cavity, is general in a sense that it is not restricted to coexistence and does not easily avail itself to such a restriction without the explicit knowledge of the expressions $P(\Delta\mu)$ and $\rho(\Delta\mu)$. As a result, it is possible that the intricate unknown dependence of the cluster interaction on $\Delta\mu$ may cause linear terms la to stay in a way not yet clearly investigated.

Nevertheless, it can be shown, that in the limit of low density Equation 3.14 properly reduces to Fisher's non-interacting cluster concentrations. At low densities, the ideal gas law $Pv_1 = \rho T$ can be used to connect the pressure with the fractional volume density ρ of the clusters, where v_1 is the volume of one particle. Combined with the Taylor expansion of the logarithm (one term retained), the ideal gas condition simplifies the cluster interaction as follows:

$$\begin{aligned}\exp(-\beta P(\Delta\mu)v_{cavity} + \ln(1-\rho(\Delta\mu))) &\approx \exp\left(-\frac{v_{cavity}}{v_1}\rho(\Delta\mu) - \rho(\Delta\mu)\right) \\ &\approx 1 - \rho(\Delta\mu)\left(\frac{v_{cavity}}{v_1} + 1\right). \qquad (3.17)\end{aligned}$$

Therefore, at low densities the effect of cluster interaction is small, and in case of coexistence no linear terms survive (except for the la-terms in the combinatorial factor).

It is also important to mention, that the linear terms are expected to vanish at low temperatures at coexistence for a different reason. As it is seen from Equation 3.12, the average cluster surface area is a function of the upper temperature limit β_2, so that the constants $\kappa(\beta_2)$ and $l(\beta_2)$ are also functions of this temperature. As the temperature goes to zero ($\beta_2 \to \infty$), the clusters stop having convoluted surfaces due to the lack of energy in the system to afford a large total liquid-vapor interface. As a result, the clusters that form at low temperatures are mostly spherical (minimal surface area) or nearly so with the surface-volume relationship $\overline{s}(\beta_2) = \kappa(\beta_2)a^{\sigma}$ approaching that of a perfect sphere. In other words, the clusters stop being fractal, and the linear volume dependence of the cluster surface area disappears ($l(\beta_2) \to 0$), while $\kappa(\beta_2)$ tends to κ_∞ of a geometrical sphere. Exact functional forms for $\kappa(\beta_2)$ and $l(\beta_2)$ are extremely complex and require the knowledge of cluster combinatorics and all the interference effects in the system. A more complete analysis of cluster fractality as a function of temperature using a restricted set of SAP combinatorics can be found in the work of Elliott *et al.* [Elli 04].

3.1.4 Thermodynamics

With Equation 3.13 describing cluster concentrations, thermodynamic analysis of cluster data at coexistence can be performed using the methodology described in Chapter 2. The differential equation technique (DET) introduced in that chapter for Stillinger-like geometric clusters can be easily carried over to apply to Fisher's droplets with a minimum of Fisher-specific changes. Similar to the modification of cluster concentrations, the surface summation in Equation 2.40 has to be dropped, and the cluster surfaces must be replaced by the most probable values at fixed cluster sizes. Again SAPs are very handy and can be used to justify this approximation. In Figure 3.5 the surface area distributions of self-avoiding polygons of different sizes are multiplied by the corresponding surfaces to mimic the summand in the numerator of the Equation 2.40. The presence of peaks is clearly observed and supports the approximation of the surface sum by the largest term. Therefore, the Fisher-modified differential equation can be written as:

$$T\left.\frac{\partial P}{\partial T}\right|_{\mu} - P \approx \frac{c\sum\limits_{a} \overline{s} n'(a,\beta,P)}{1+\sum\limits_{a} a n'(a,\beta,P)}, \tag{3.18}$$

where

$$n'(a,\beta,P) \approx q_0[a^{\sigma}+la]^{-x}\exp([k-c_0\beta-t_s\kappa\beta P][a^{\sigma}+la])\exp(-\beta P a) \tag{3.19}$$

is the density independent part of the cluster concentrations. Substituting the most probable cluster surface with the appropriate dependence on the cluster size, the

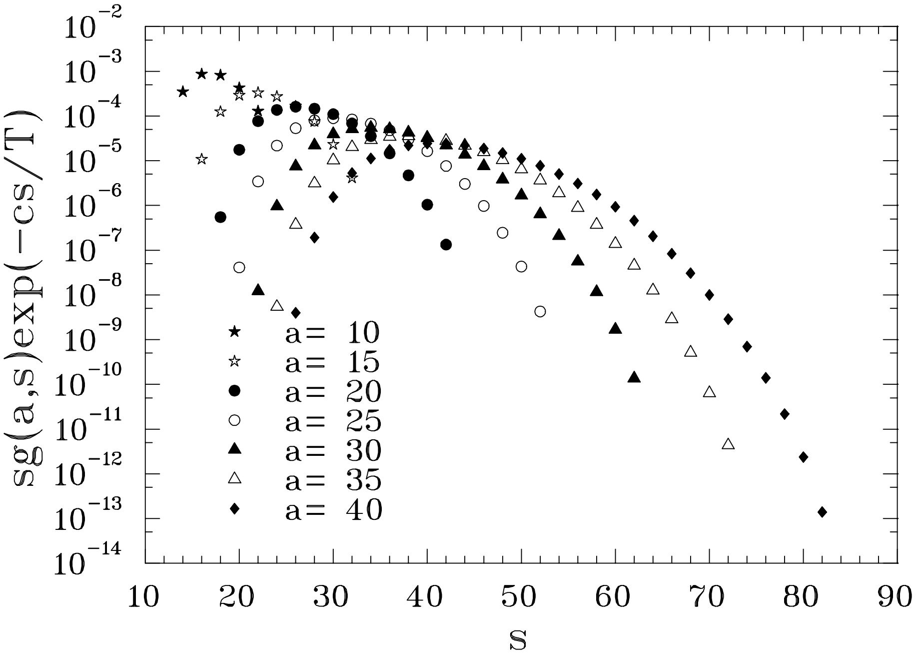

Figure 3.5: The basis for Fisher's conjecture in Equation 3.18 using the example of SAP. In this example again $T = 2$, and the pressure dependent part was not included.

coexistence pressure of the fluid can be found as a solution of the equation

$$T \left.\frac{\partial P}{\partial T}\right|_{\mu} - P \approx \frac{c_0 \sum\limits_a [a^\sigma + la] n'(a, \beta, P)}{1 + \sum\limits_a a n'(a, \beta, P)} \tag{3.20}$$

with the initial condition $P(T = 0) = 0$, if Fisher's exponents and other parameters of the model are known. Once the coexistence pressure is determined, the density of the fluid can be evaluated as

$$\rho \approx \frac{\sum\limits_a a n'(a, \beta, P)}{1 + \sum\limits_a a n'(a, \beta, P)}, \tag{3.21}$$

and other thermodynamic quantities can be calculated from the pressure in a standard way. For example, the fluid's energy is

$$u \approx c_0 \sum_a [a^\sigma + la] n(a, \beta, P, \rho), \tag{3.22}$$

and the heat capacity is

$$\begin{aligned} c_V &= \left.\frac{\partial u}{\partial T}\right|_V \approx \frac{c^2}{T^2}\left[\kappa^2\sum_a[a^\sigma+la]^2n - t_s\kappa^3\sum_a[a^\sigma+la]n\sum_a[a^\sigma+la]^2n\right. \\ &- 2\kappa^2\sum_a[a^\sigma+la]n\sum_a a[a^\sigma+la]n + \kappa^2\left(\sum_a[a^\sigma+la]n\right)^2\sum_a a^2n \\ &+ \left. t_s\kappa^3\left(\sum_a[a^\sigma+la]n\right)^2\sum_a a[a^\sigma+la]n\right] \end{aligned} \tag{3.23}$$

3.2 How the Modified Fisher's Model Can Be Used in Data Analysis

The application of the modified Fisher's model to experimental nuclear cluster distributions can be accomplished similarly to the methodology employed to analyze these clusters with the original version of the model. The main goal of the analysis is to find a set of Fisher's parameters that characterizes the available cluster distributions in the best possible way. This is accomplished through fitting the model to all the data simultaneously (global fitting) by minimizing the total χ^2. However, the use of the modified Fisher's model cannot be reduced to mere fitting due to the pressure and density dependence of cluster concentrations. Therefore, on each iteration of the χ^2-minimization procedure, the best estimates of the pressure and density must also be found. This can be done using Equations 3.20 and 3.21 for the intermediate values of Fisher's parameters. In these equations the summation has to go to infinity, though in practice summing up to the cluster size of several thousand particles should be sufficient to reach the required accuracy. Therefore, a self-consistent fitting procedure can be set up to analyze the experimental data and to determine thermodynamics of the system with a few fitting parameters: q_0, l, x, k, κ. The value of σ should be fixed according to the dimensionality of the problem, c_0 can be found independently, since $c_0 = c\kappa$, and the surface tension c is approximately known from the liquid drop model. The skin thickness t_s can also be given a reasonable estimate based on charge density profiles obtained in electron scattering experiments. Once the minimization successfully converges, the pressure and density obtained at the last iteration provide the best estimates of the nuclear thermodynamic quantities at coexistence as functions of temperature and enable the construction of the liquid-vapor phase diagram in an alternative way that takes into account cluster interference.

3.2.1 Numerical Testing with Geometric Clusters

The modified Fisher's methodology, as outlined above, is ready to be applied to nuclear cluster distributions if care is taken to filter out Coulomb and quantum effects in a standard way. However, the methodology cannot be relied upon unless it passes the test with geometric clusters of the lattice gas (Ising model). To realize the test, cluster concentrations from two-dimensional Ising simulations can be folded in the surface degree of freedom to become the functions of cluster size:

$$n(a, \beta, P, \rho) = \sum_{s} n(a, s, \beta, P, \rho), \tag{3.24}$$

thus resembling a nuclear-cluster data set. These concentrations can be fitted directly with the modified Fisher's prescription to obtain the phase diagram of the lattice gas. A Matlab procedure has been developed to implement the necessary coding. Five independent fitting parameters were used to minimize the χ^2: q_0, l, x, k, and c_0. The value of $\sigma = 1/2$ was fixed by the dimensionality of the problem. Parameter $\kappa = c_0/c$ was defined by the Ising surface tension $c = 2$. The skin thickness t_s is unity for geometric clusters on the lattice if thermodynamic quantities in question are determined per lattice site. The entire listing of the code is provided in Appendix A.

A finite set of medium-size clusters $a \in (10 : 25)$ has been chosen for fitting to mimic the restrictions on the nuclear data. The temperature range was $T \in (1.5 : 2.2)$ with a gap $\Delta T = 0.05$. The lower temperature boundary was determined by the requirement of sufficient statistics for the clusters in consideration, and the upper boundary was set to be below the critical temperature $T_c \approx 2.269$, as it is a typical situation for nuclear clusters.

The χ^2-minimization successfully converged and yielded the best set of parameters shown in the left half of Table 3.1. With these parameters, the resulting fits are displayed in Figure 3.6 for several sample concentrations. The figure displays a rather accurate fitting of the concentration, especially taking into account the fact that the

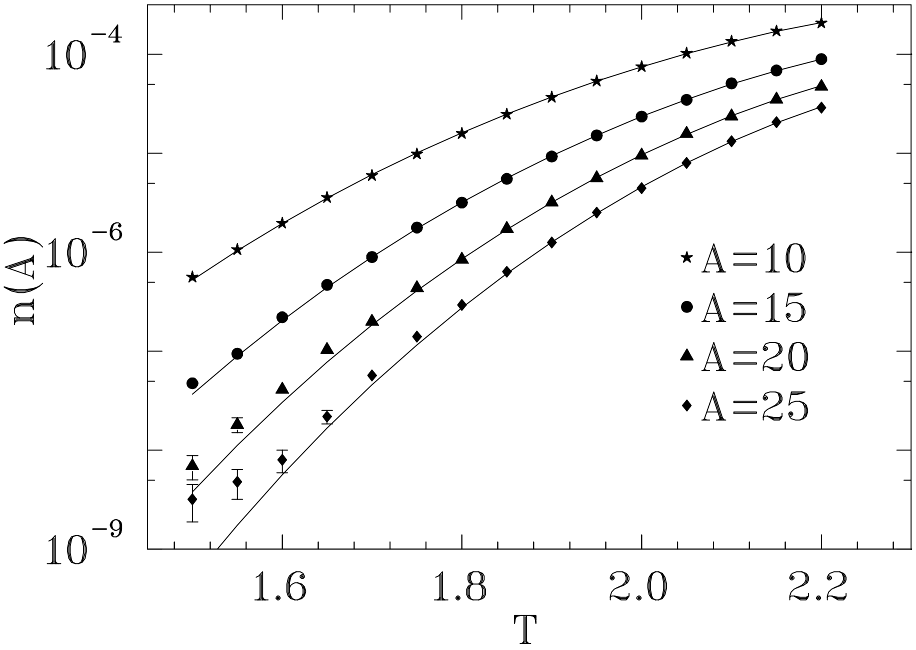

Figure 3.6: Geometric-cluster concentrations extracted from a two-dimensional Ising simulation (symbols) with fits by the modified Fisher's model (solid lines).

procedure was global. Deviations are observed at low temperatures mostly for larger clusters due to poor statistics. However, statistics are not the only cause for the deviations. It can be seen that there are systematic deviations at low temperatures that show the limitations of the many approximations involved.

The pressure of the lattice gas as a function of temperature can be obtained at the last iteration of the fitting routine solving Equation 3.20 with the best set of the fitting parameters. Figure 3.7 exhibits the result of the calculation. It is very pleasing to see that except for low temperature region the extracted pressure is almost indistinguishable from the exact coexistence pressure of the lattice gas. The error bars are about one per cent (estimated from the parameter errors), and cannot

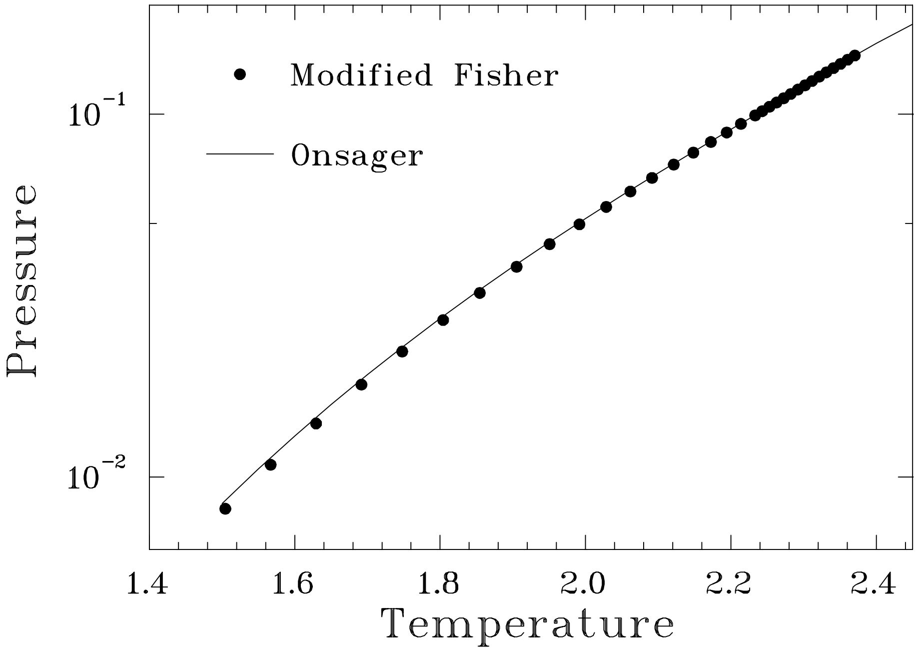

Figure 3.7: Comparison of the two-dimensional lattice gas coexistence pressure obtained from the analysis of geometric clusters (solid circles) with the exact pressure (line).

be seen on the plot. The varying length of the intervals between the temperature values is due to the automatic step control mechanism in the numerical procedure that integrates the differential equation.

The critical temperature of the lattice gas can be determined by the peak in the heat capacity, calculated using Equation 3.23. It is expected that the modified Fisher's model is valid beyond the critical temperature. Again this expectation can be justified resorting to the analogy with SAPs. In Chapter 2 it has been demonstrated that the finite volume approximation (FVA) and SAP combinatorics together provide a very accurate description of simulated geometric cluster concentrations below the critical temperature of the lattice gas (as a reminder see Equation 3.7). At the

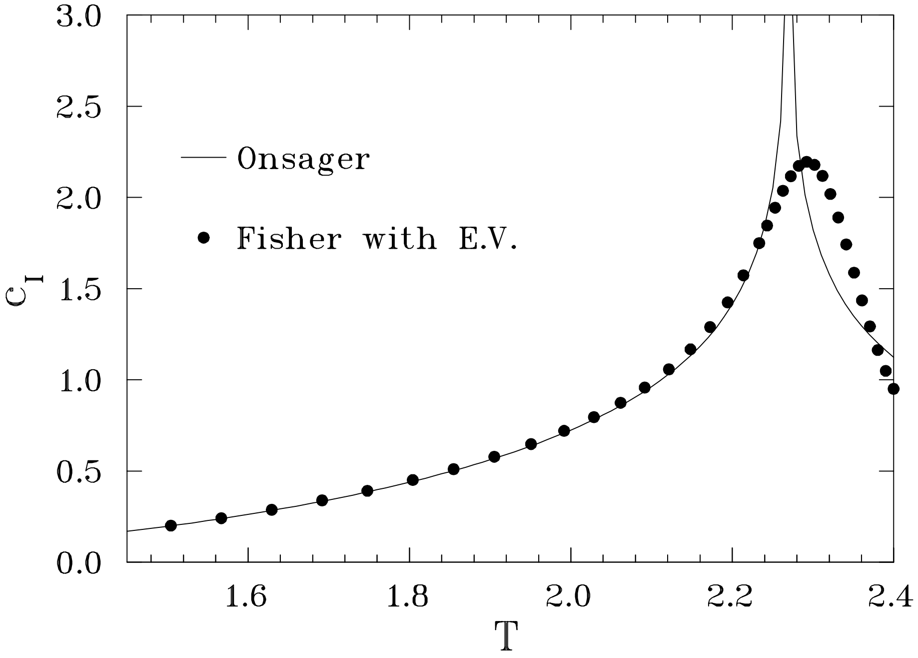

Figure 3.8: Comparison of the two-dimensional Ising heat capacity obtained from the analysis of geometric clusters (solid circles) with Onsager's exact heat capacity (line).

same time, no condition exists that would require this approximation to fail at and above the critical temperature: clusters continue to exist and interfere, the system is characterized by a particular pressure, and the combinatorics of the clusters is the same SAP combinatorics. On the opposite, the heat capacity calculated with this approximation clearly shows a meaningful peak and allows estimation of the lattice gas critical temperature with four per cent accuracy. When merging the finite volume approximation with Fisher's model, the only major change is the use of an analytic expression to describe combinatorial factors. But the combinatorial factors remain the same no matter what the temperature is. Therefore, the modified Fisher's model should not *a priori* be limited by the subcritical region and may work in the supercritical region just as well till it may somehow fail. When applied to geometric clusters the sensitivity of Fisher-based procedure can be even better than that based on SAPs due to parameter flexibility and plausibility of a more complete summation, that runs up to the cluster size of a thousand in the present calculation the results of which are shown in Figure 3.8. The figure compares the heat capacity from fitting simulated geometric cluster data with the exact heat capacity from the Onsager solution. The critical temperature is estimated at $T_c \approx 2.293 \pm 0.007$, which deviates from the true critical temperature by about one per cent.

The success of the aforementioned technique to construct the phase diagram of the two-dimensional lattice gas and accurately determine its critical temperature is encouraging, and suggests application of this methodology to experimental data.

3.2.2 A Possible Way of Testing Cluster Concentrations for Non-ideality

Unlike geometric clusters of the Ising model, it is not *a priori* known whether the nuclear cluster gas is non-ideal. It may be, however, that during the cluster formation in the nucleus just prior to the emission there is a competition between various cluster forms that are mutually exclusive. And if one form is successful in emission, it precludes other forms from leaving the nucleus thereby creating a possibility of cluster interference. For example, an analogy of the excluded volume effect can be visualized as follows. Suppose a cluster of a certain size a forms on the nuclear interface and is emitted. At the moment of emission, the fragment blocks an area of the nuclear interface equal to the fragment's cross sectional area σ_a. Multiplied by the fragments velocity v_a and the characteristic nuclear time τ_{nuc}, the cross section σ_a yields a volume V_a in the immediate vicinity of the emitting nucleus (compare to the notion of the cluster cavity) which is blocked from containing fragments (clusters) of any other size but a:

$$V_a = \sigma_a v_a \tau_{nuc} \tag{3.25}$$

Therefore, the phase space available to all other possible fragments is reduced causing the effect of fragment interference. Be it as it may, effects of cluster interference in nuclear cluster distributions can only be tested experimentally by comparing the results of traditional Fisher's analysis with the results obtained using the modified Fisher's model: both methods will produce the pressure and χ^2-values, which need to be compared to draw the conclusions. This comparison is helpful to answer the question whether it is necessary to invoke a more complex cluster analysis methodology, or the ideal-cluster-gas approximation is enough.

In the following, a comparison procedure is conjectured on the basis of geometric clusters and SAPs. Geometric clusters form a non-ideal gas that can successfully be analyzed with the modified Fisher's model. On the other hand, a hypothetical ideal gas of geometric clusters can be created using SAP combinatorics with the

Modified Fisher χ^2/D = 2.85			Original Fisher χ^2/D = 109.86		
Parameter	Value	Error	Parameter	Value	Error
q_0	0.0279	0.0003	q_0	0.0278	0.0050
l	0.1382	0.0002	l	0.0411	0.0171
x	3.5530	0.0032	x	3.7147	0.3525
k	3.6937	0.0026	k	3.3560	0.1310
c_0	7.3077	0.0065	c_0	7.4204	0.4084

Table 3.1: The best set of the fitting parameters obtained from the analysis of geometric clusters of the two-dimensional Ising model. D is the number of degrees of freedom in the fit.

Modified Fisher χ^2/D = 76.05			Original Fisher χ^2/D = 19.23		
Parameter	Value	Error	Parameter	Value	Error
q_0	0.0036	0.0006	q_0	0.0364	0.0002
l	0.0650	0.0075	l	0.0595	0.0001
x	0.4405	0.2697	x	4.0177	0.0013
k	3.7671	0.0946	k	4.3507	0.0011
c_0	8.8818	0.2355	c_0	8.7929	0.0018

Table 3.2: The best set of the fitting parameters obtained from the analysis of SAP gas clusters. D is the number of degrees of freedom in the fit.

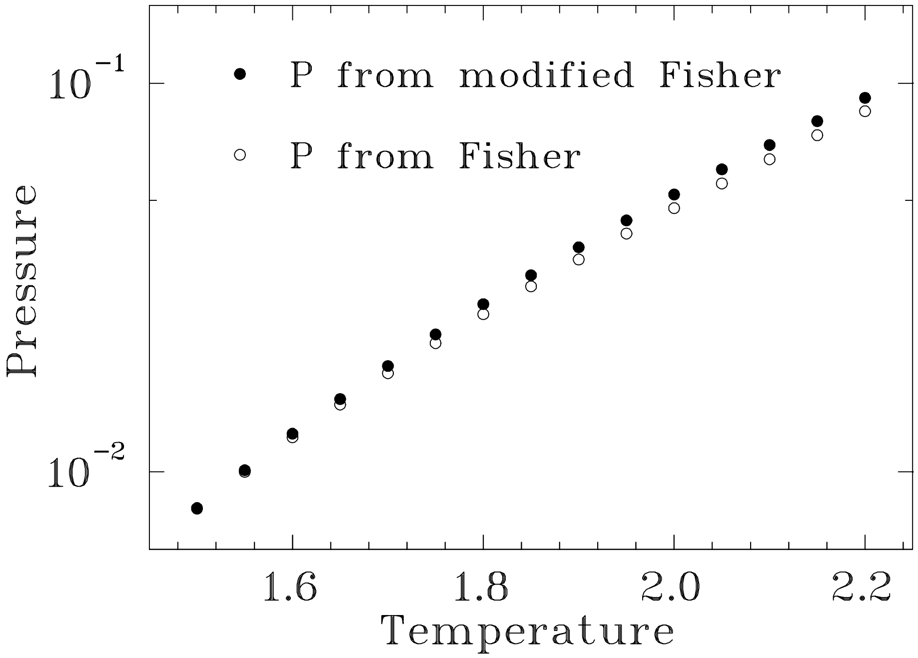

Figure 3.9: Comparison between the values of the pressure obtained by fitting geometric clusters of the two-dimensional Ising model with original and the modified Fisher's models.

corresponding concentrations calculated in the dilute limit as

$$n(a,\beta) = \sum_{s} g_{SAP}(a,s)\exp(-c\beta s), \tag{3.26}$$

where as before $g_{SAP}(a,s)$ is the total possible number of SAPs of size a and surface s. Such a gas mimics a nuclear cluster vapor that is inherently ideal in comparison with a non-ideal gas modeled by geometric clusters. Application of the two Fisher's techniques to these gases may reveal relative characteristic signatures identifying the presence and extent of the interference effects in cluster distributions.

In order to realize a fair comparison, a modification due to fractality must be introduced to original Fisher's model. In other words, the only difference between

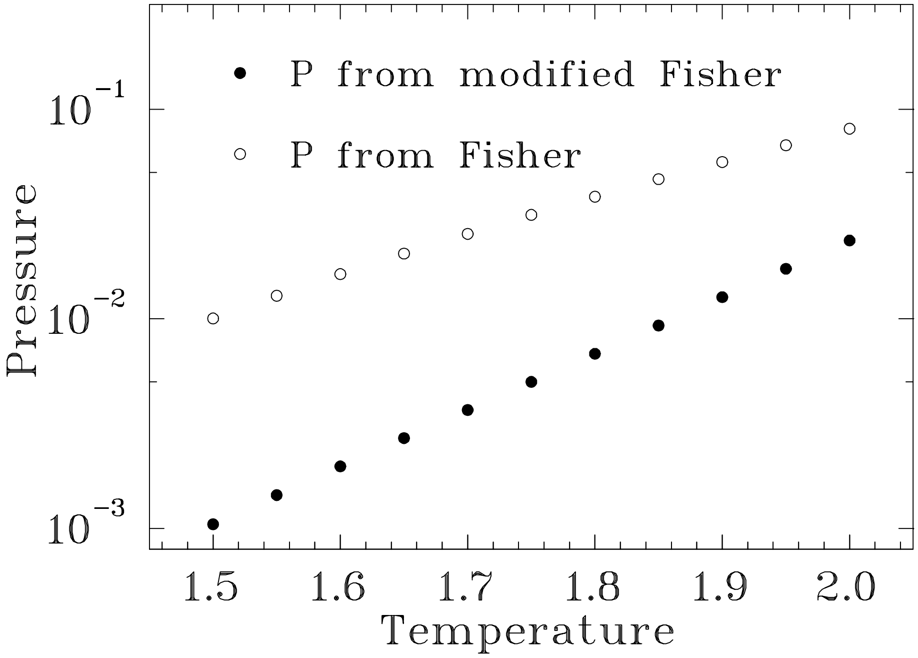

Figure 3.10: Comparison between the values of the pressure obtained by fitting SAP gas clusters with original and the modified Fisher's models.

original and the modified Fisher's models used for testing must be solely due to cluster interference. Therefore, the original Fisher's concentrations must contain parameters l, x, and k as they were defined for the modification:

$$n(a, \beta) \approx q_0[a^\sigma + la]^{-x} \exp\{[k - c_0\beta][a^\sigma + la]\} \tag{3.27}$$

The following results emerged from the calculations. In the first case the cluster gas was non-ideal represented by geometric clusters. Application of the modified Fisher's model produces a much better χ^2, while the parameters of the two models do not differ substantially, as shown in Table 3.1. The pressure obtained from the modified Fisher's model is only several per cent higher than that of the original, as Figure 3.9 depicts it.

Quite different situation occurs when the cluster gas is ideal, like the hypothetical SAP gas. Forcing modified Fisher's model to fit such distributions leads to an utter failure in comparison with original model, as demonstrated by the χ^2 and the values of the fitting parameters in Table 3.2. In addition to that, the pressure extracted from the modified Fisher's model is suppressed several times as compared to the pressure of original Fisher's model. The observation of these symptoms indicates the lack of the interference effects in cluster concentrations. Therefore, the original version of Fisher's model is expected to provides a better estimate of the phase diagram, since it does not rigidly impose functional forms due to cluster interference which the concentrations do not support. Figure 3.10 demonstrates the comparison of the pressures below the critical temperature of the SAP gas, found to be about $2J$.

3.3 Conclusions

The procedure presented in this chapter offers a general Fisher-model-based methodology to analyze nuclear cluster distributions at thermodynamic phase coexistence and construct a phase diagram. The procedure makes an assumption that nuclear clusters, as complex as they are, may still contain characteristic signatures of Stillinger's configurational clusters. If so, the methodology may approximately account for Stillinger's cluster interference and produce thermodynamic results more accurate than those obtained with the ideal-cluster-gas approximation. Geometric clusters of the Ising model, representing Stillinger's clusters on the lattice, clearly demonstrated the superiority of the new interacting-cluster-gas approach in comparison with the traditional treatment of clusters as an ideal gas.

The new analysis procedure opens an opportunity to look for cluster interaction effects (mostly due to excluded volume) in nuclear cluster production. Combining the procedures with and without cluster interaction included, it may be possible to answer the question whether the effects are there, and what their extent is. Characteristic signatures of the two possible outcomes have been demonstrated using the example of geometric clusters.

Part II

Multiple-Chance Effects in α-Particle Evaporation

Chapter 4

Introduction

4.1 Theoretical Considerations

Evaporation-like process in hot nuclei and its thermodynamic representation have been thoroughly discussed in the previous part of this thesis. Regardless of the way energy is delivered to a nuclear system, the resulting excited nucleus proceeds to deexcite by emission of fragments in a wide range of masses beginning with neutrons and protons and reaching drops half the size of the decaying system (fission). The fragments are emitted in a statistical way, the rate of emission being controlled by the average bulk binding energy of the fragment.

Equilibrium thermodynamic characterization of nuclear matter, much like that of ordinary fluids, completely eliminates any memory of events between the phases. In other words, when drops form, no information about the history of a particular drop in the liquid phase is expected to pass to the gas phase. Kinetically, the statistical emission of fragments implies their random formation on the nuclear interface.

Statistical emission of fragments from thermalized nuclear systems has been clearly confirmed experimentally to be the dominant mode of decay of hot nuclei [More 97]. Nevertheless, there has been an expectation that kinetics of the fragment emission may somehow be influenced by the quantum effects of fragment formation inside the parent nucleus prior to the emission from the nuclear interface [More 97b]. This preformation may be especially noticeable for such a tightly bound fragment as the α-particle. If α-particles are indeed present in the nucleus before emission, their presence may manifest itself in a certain way in the evaporation process.

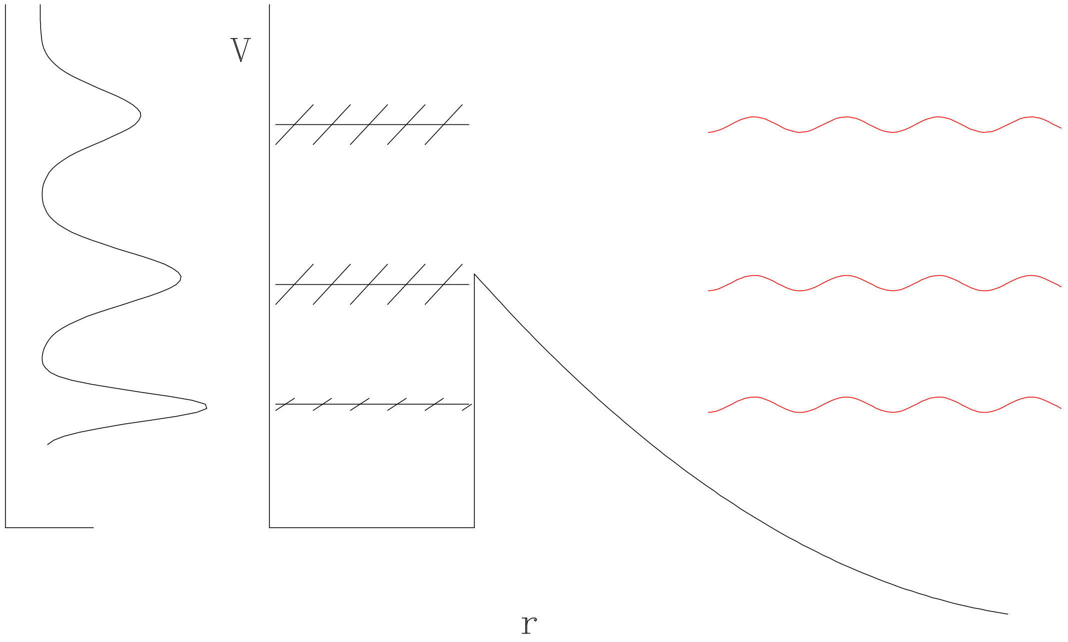

Figure 4.1: Schematic representation of the states of a fragment in a nuclear potential well.

The logic is as follows. Suppose that a fragment preexists in a nucleus before it is emitted. As the fragment readies itself to leave the nucleus, it senses the well-like nuclear potential and acquires the quantum states, which possess a certain width due to their coupling with the continuum and the many-body degrees of freedom of the nucleus. This point is illustrated in Figure 4.1. The states of the fragment inside the well are the shell-model-like states, while the states above the well are the optical-model resonances which may appear if a compound nucleus is formed. Therefore, when the kinetic energy spectrum of such a fragment is accumulated, the statistical-emission-only background of the spectrum may be modulated by a strength function, which arises due to the quantum states of the fragment in the potential well of the parent nucleus. These quantum effects may introduce a bias in the emission spectrum of fragments, since some energies are preferred over the others.

Experimental observation of the modulations may be made possible if accurate theoretical description of the statistical background is achieved. Then the experimental high-statistics spectrum (discussed later) can be compared to a theoretical form to reveal the modulations.

The statistical background of the kinetic energy evaporation spectrum can in principle be estimated using detailed balance of the initial (before emission) a and final (after emission) b states of a nuclear system according to Fermi's Golden Rule:

$$\rho_a \Gamma_{a \to b} = \rho_b \Gamma_{b \to a}, \tag{4.1}$$

where $\Gamma_{a \to b}$ and $\Gamma_{b \to a}$ are the direct and the inverse decay widths, and ρ_a, ρ_b are the corresponding nuclear level densities. The inverse width can be expressed in terms of the "inverse" cross section σ_{inv}:

$$\Gamma_{b\to a} = \hbar\frac{\sigma_{inv}v}{V}, \tag{4.2}$$

where v is the velocity of the fragment, and V is the normalization space volume.

Equations 4.1 and 4.2 can be combined to yield the differential decay width with respect to the fragment's kinetic energy ϵ in the direct reaction:

$$\Gamma(\epsilon)d\epsilon \propto \sigma_{inv}\epsilon\rho(E - B - \epsilon)d\epsilon, \tag{4.3}$$

where E is the initial energy of the hot nucleus, and B is the fragment's binding energy. Expanding the logarithm of the level density to the first order in the fragment's kinetic energy, an approximate expression for the kinetic energy spectrum of a fragment can be obtained:

$$\Gamma(\epsilon)d\epsilon \propto \sigma_{inv}\epsilon \exp\left(-\frac{\epsilon}{T}\right) d\epsilon, \tag{4.4}$$

where T is the temperature of the hot parent nucleus. Equation 4.4 is the theoretical basis for conventional models to understand the statistical part of the fragment's kinetic energy spectrum obtained in the evaporation of excited nuclei. Additional models and empirical formulae are used to describe the inverse cross section σ_{inv} to yield an analytic expression for the kinetic energy spectrum. As a result generality is forfeited. In addition to that, conventional models do not incorporate thermal shape fluctuations of the emitting nucleus, which leads to poor performance of these models when analyzing experimental data.

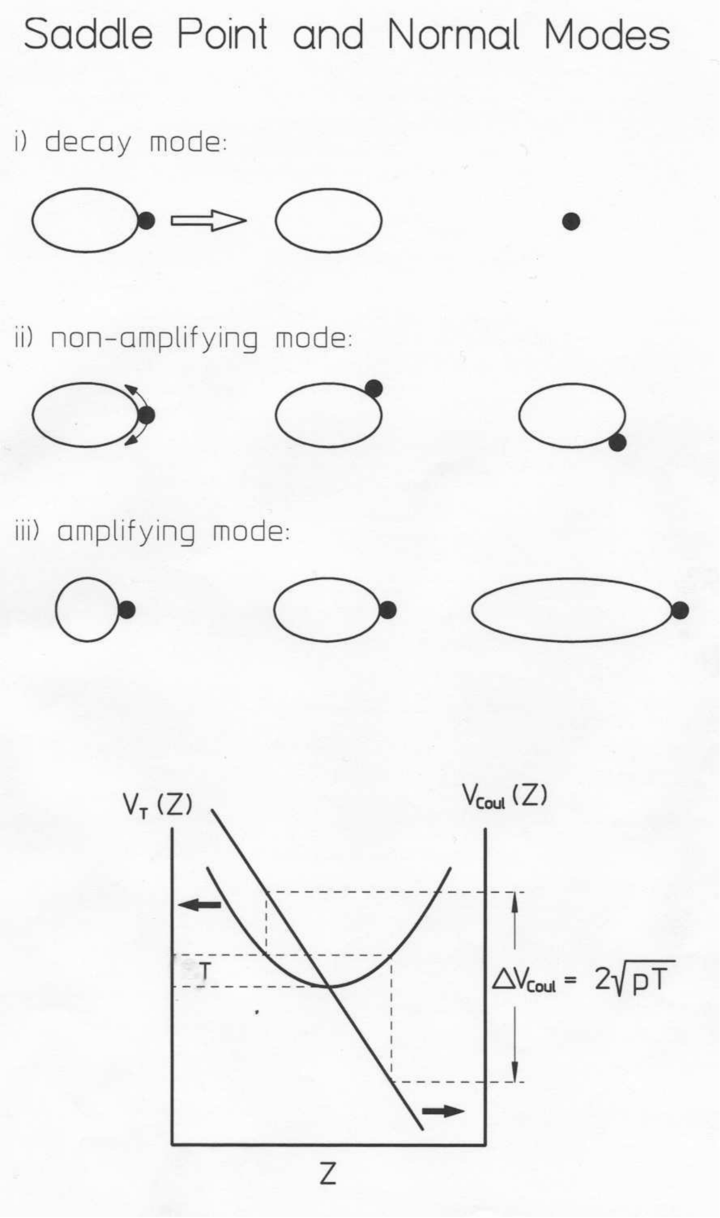

Figure 4.2: Top: Normal modes at the saddle point. Bottom: Total potential energy V_T and Coulomb energy V_{Coul} as a function of the deformation coordinate Z.

An alternative general approach is due to Moretto [More 75, More 87] whose unconventional fragment emission theory is based on the saddle point approximation with additional consideration of nuclear deformation. The theory takes into account only statistical degrees of freedom at the saddle of the transition state and assumes no knowledge of the entrance channel and preexisting structures in the nucleus. In addition to the usual saddle degrees of freedom the theory also includes shape polarizations of the emitting nucleus.

When a decaying nucleus reaches the scission point (decay mode) there are additional degrees of freedom or modes that the system can take. As shown in the top panel of Figure 4.2, Moretto classified the modes as amplifying and non-amplifying. The mode is amplifying if the relative contribution from Coulomb and surface energy to the system's potential energy changes widely with deformation. The deformation of the residual nucleus can be described with a deformation coordinate Z, which is defined as a change in distance between the centers of the fragment and the residual nucleus relative to the undeformed distance, the fragment being in contact with the nucleus. Increasing of Z leads to the prolate deformation of the nucleus in the direction of emission and thereby to lowering the Coulomb barrier. On the opposite, decreasing Z results in oblate deformation and elevated Coulomb barrier. Therefore, a fragment crossing over the saddle point acquires a kinetic energy at infinity smaller or greater than the Coulomb barrier associated with a spherical configuration. Such an emission is not classified as subbarrier emission in the sense of quantum barrier penetration, but rather it is a purely classical effect.

Thermal fluctuations along the deformation coordinate Z lead to large fluctuations in the Coulomb interaction energy, as shown in the bottom panel of Figure 4.2. While the total potential energy V_T has a minimum at some prolate deformation, the fragment-nucleus Coulomb interaction V_{Coul} is a monotonically decreasing function of the deformation coordinate. Therefore, the total potential and the Coulomb interaction energies can be expanded in series of Z in the vicinity of the saddle point. Retaining only the first terms of the expansion, the expressions are

$$\begin{aligned} V_T &= V_T^0 + kZ^2 \\ V_{Coul} &= V_{Coul}^0 - cZ \end{aligned} \tag{4.5}$$

If the shape of the emitting nucleus is allowed to fluctuate involving an energy of the order of the temperature T, the corresponding fluctuations of the Coulomb energy are

$$\Delta V_{Coul} = 2\sqrt{\frac{c^2}{k}T} = 2\sqrt{pT}, \tag{4.6}$$

where the parameter p is called the amplification parameter, which characterizes the relative properties of the total and Coulomb potentials with respect to deformation in the amplifying mode. The parameter p itself is not expected to depend on the deformation, at least in the second order, but rather indicates the amplitude of the Coulomb barrier fluctuations as a function of the amplitude of the total energy fluctuations. The fluctuations of the Coulomb barrier strongly affect the width of the kinetic energy spectrum.

When the potential energy varies almost exclusively from the Coulomb energy, the mode is non-amplifying, since the deformation-dependent Coulomb energy change is relatively small in the absence of the surface energy change. For instance, the oscillation of a fragment about the tip of a prolate emitting nucleus can be considered a non-amplifying mode. As the fragment rolls away from the tip, the Coulomb energy increases due to the decreasing distance between the centers of the fragment and the nucleus, while the surface energy of the system changes only in higher order terms of the deformation coordinate series and can be considered approximately constant. Non-amplifying modes are not expected to affect the width of the kinetic energy spectrum as much as the amplifying mode and will not be considered in this thesis.

Moretto derived several analytic expressions for the kinetic energy spectrum of a fragment $P(\epsilon)$ taking into account various combinations of amplifying and non-amplifying modes. The simplest and the most successful approach included only the amplifying mode and yielded the following result:

$$P(\epsilon) \propto \exp\left(-\frac{x}{T}\right) \operatorname{erfc}\left(\frac{p-2x}{2\sqrt{pT}}\right), \tag{4.7}$$

where $x = \epsilon - V^0_{Coul}$. More complex expression was used by Kexing Jing, whose work will be mentioned in more detail later. Overall, these analytic results bypassed the problem of modeling the inverse cross section in conventional statistical models and provided a way to directly analyze experimental spectra for any traces of residual quantum effects in nuclear fragment evaporation.

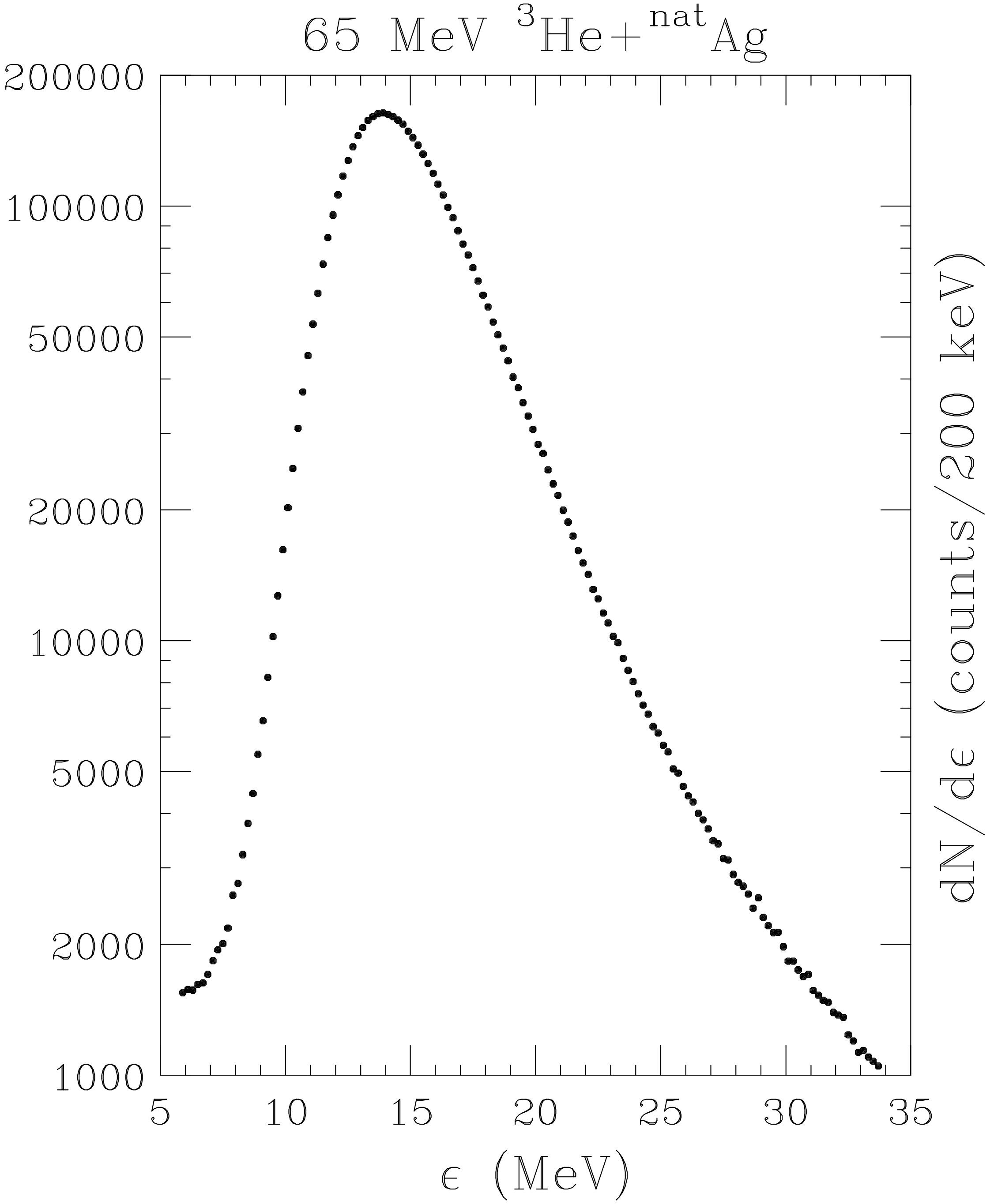

Figure 4.3: The center-of-mass energy spectrum of α-particles emitted from the ^{3}He+^{nat}Ag reaction at 65-MeV beam energy.

4.2 Experimental Evaporation Spectra

Experimental fragment-evaporation spectra are usually obtained by bombarding various target nuclei with light charged particles. The most abundant fragments that evaporate from the resulting compound nucleus are α-particles. Due to high probability of emission, α-particles can be detected in very large numbers, and high-statistics kinetic energy spectra can be accumulated. The experimental spectra used in this thesis were obtained at the 88-Inch Cyclotron of the Lawrence Berkeley National Laboratory by Kexing Jing [Jing 99] who used two position-sensitive ΔE-E quad telescopes to detect the particles emitted in the reactions. Jing used ^{3}He beam of energies 55, 65, 75, 85, 95, 110, 125, 140 MeV to bombard the targets made of ^{197}Au, ^{181}Ta, $^{\mathrm{nat}}$Ag, $^{\mathrm{nat}}$Cu, ^{27}Al and ^{12}C. A typical spectrum is shown in Figure 4.3.

The data sets used for analysis in this thesis include only the spectra from the ^{3}He+$^{\mathrm{nat}}$Ag reaction at 55, 65, 75, 95, 110, and 125 MeV beam energies. Since the goal of the study is to look for fine effects in the spectra, the maximum errors are set at 1%, thereby cutting the edges of the spectra at about 10000 counts. Doing so produces distributions consisting of 61 energy points with the bin size of 200 keV covering the range of kinetic energies between 10 and 23 MeV.

4.3 Apparent Evidence of Preexisting Particle Structures in α-Evaporation

In his attempt to investigate quantum effects in evaporation spectra, Jing used Moretto's transition state formalism with the inclusion of one decay mode, one amplifying mode, and the barrier penetration [Jing 99]. The resulting formula for the evaporation spectra $P(\epsilon)$ was the following:

$$\begin{aligned} P(\epsilon) \quad \propto \quad & e^{-x/T}\Big\{ \operatorname{erf}\Big((2V^0_{\text{Coul}}+p)/2\sqrt{pT}\Big) - \operatorname{erf}\Big((p-2x)/2\sqrt{pT}\Big) \\ & +\frac{1}{2}e^{-(p-2x)^2/4pT}\Big[e^{(p-2x-\gamma pT)^2/4pT}\Big(1+\operatorname{erf}\Big((p-2x-\gamma pT)/2\sqrt{pT}\Big)\Big) \\ & -e^{(p-2x+\gamma pT)^2/4pT}\Big(\operatorname{erf}\Big((2V^0_{\text{Coul}}+p+\gamma pT)/2\sqrt{pT}\Big) \\ & \qquad\qquad - \operatorname{erf}\Big((p-2x+\gamma pT)/2\sqrt{pT}\Big)\Big)\Big]\Big\}, \end{aligned} \tag{4.8}$$

where again $x = \epsilon - V^0_{\text{Coul}}$ and ϵ is the kinetic energy of evaporated particle; V^0_{Coul} is the Coulomb barrier; T is the temperature of the residual nucleus; p is the amplification parameter, and γ is a parameter representing the barrier penetrability.

In the case where the temperature T is low and the Coulomb barrier V^0_{Coul} is large (for α particles, for example), $\operatorname{erf}\Big((2V^0_{\text{Coul}}+p)/2\sqrt{pT}\Big) = 1$, and $\operatorname{erf}\Big((2V^0_{\text{Coul}}+p+\gamma pT)/2\sqrt{pT}\Big) = 1$. Taking advantage of this fact, Equation 4.8 can be rewritten as:

$$\begin{aligned} P(\epsilon) \quad \propto \quad & e^{-x/T}\Big\{ \operatorname{erfc}\Big((p-2x)/2\sqrt{pT}\Big) \\ & +\frac{1}{2}e^{-(p-2x)^2/4pT}\Big[e^{(p-2x-\gamma pT)^2/4pT}\operatorname{erfc}\Big(-(p-2x-\gamma pT)/2\sqrt{pT}\Big) \\ & -e^{(p-2x+\gamma pT)^2/4pT}\operatorname{erfc}\Big((p-2x+\gamma pT)/2\sqrt{pT}\Big)\Big]\Big\}. \end{aligned} \tag{4.9}$$

It should be noticed that Equations 4.8 and 4.9 do not contain polynomials in ϵ of 2^{nd} order or higher, and the (complementary) error functions and the exponentials are all smooth functions. Therefore, the observation of spectrum modulations should not come from spurious polynomial oscillations.

Jing used the smooth function of Equation 4.9 to fit the alpha spectra and to search the residuals for modulations. The extremely accurate fits he obtained indicated the success of Moretto's theory in accounting for the bulk properties of the spectra. In addition to that the fit residuals revealed the existence of the oscillations that were ascribed to the preexistence of α-particles in the potential well of the parent nucleus. Shown in the lower panel of Figure 4.4 are the measured alpha spectra and the fit for the $^{3}\mathrm{He} + {}^{\mathrm{nat}}\mathrm{Ag}$ reaction at various beam energies. The quality of the fit is remarkable. The exceedingly good quality of the fit indicates that, on the one hand, the bulk of the evaporation spectrum is indeed statistical, and that, on the other hand, the shape fluctuations at the saddle point indeed play a very important role. The percent differences between the experimental data and the fits are shown in the upper panel of the figure. The residuals of the fits are of the order of 1% throughout the energy range, which shows the goodness of the fitting function. The residuals clearly show a statistically significant modulation with an amplitude of about 1.5%. The important feature to notice is the lack of dependence of the modulations on bombarding energy. However, the shape of the modulations is strongly dependent on the type of the compound nucleus formed in the reaction, as indicated in Figure

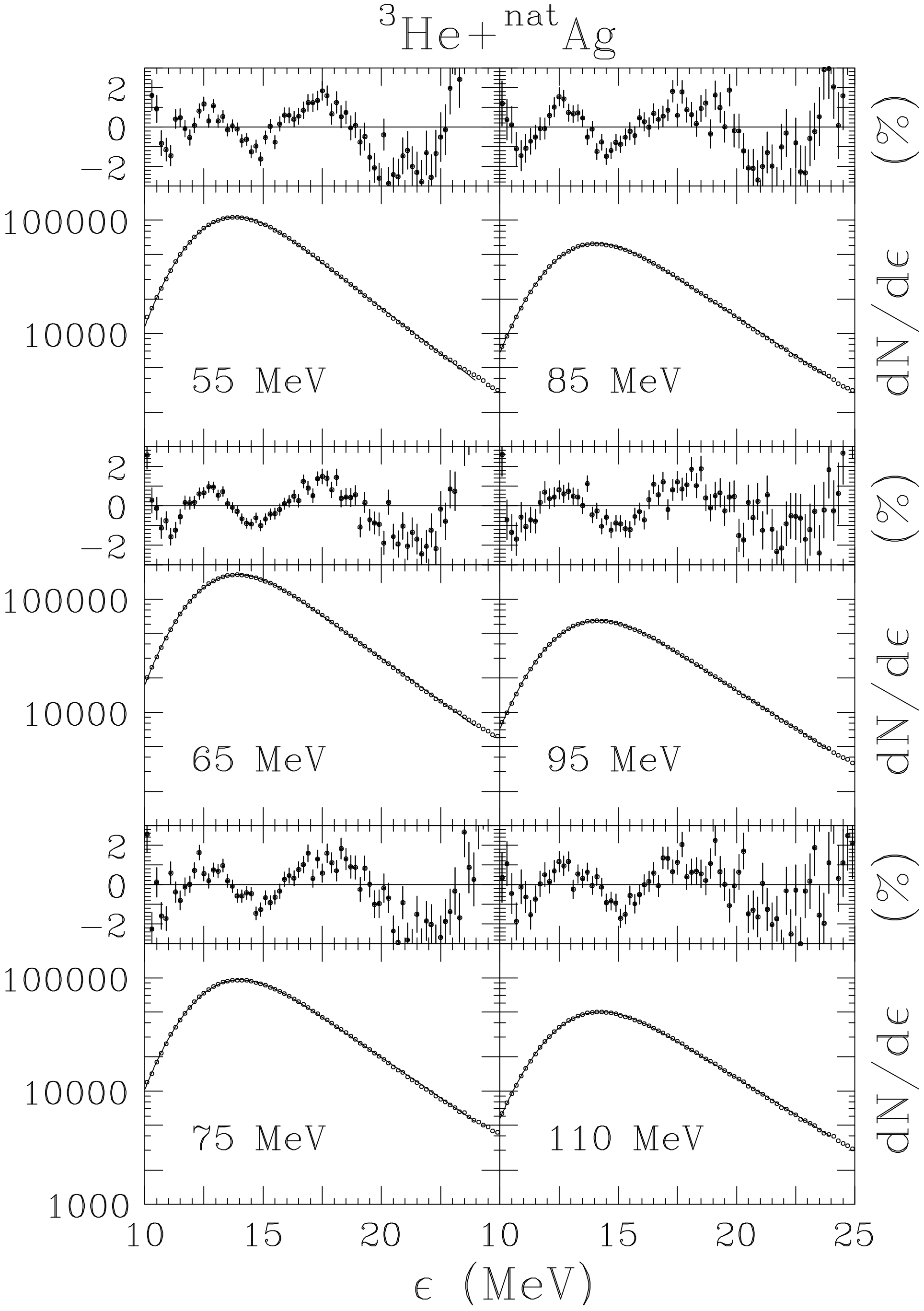

Figure 4.4: Lower panels: The experimentally measured α spectra ($\circ$) from ^{3}He + ^{nat}Ag reactions at 55, 65, 75, 85, 95, 110 MeV beam energies, and the corresponding fits (—) with Equation 4.9. Upper panels: The percent difference between the experimental data and the fits with Equation 4.9 are shown in the lower panels. The error bars represent the statistical errors of the experimental data.

4.5 for the reaction ^{3}He + ^{197}Ag.

The discovery of the oscillations raised several important questions:

- Are the modulations physical, as those expected for residual quantum effects?
- Could the modulations be introduced by departures from linearity of ADCs, amplification electronics, detectors, etc.?
- Could the oscillations be the result of the fitting problem associated with the rigidity in the fitting function?

In answering these questions Jing demonstrated that the instrumental effects could not have been possible, since the same modulations were observed in several independent detector-electronics chains. In addition to that the the same modulations have been confirmed in different follow-up experiments using different detectors, ADCs, and different chains of amplification electronics. However, answering the question about physicality of the effect has not been clearly provided in his thesis. The main problem of distinguishing between artificial fitting function rigidity effects and observation of a true phenomena was very difficult. It may be possible that there is a slight mismatch between a smooth fitting function and a true statistical evaporation spectrum which is also smooth that produces the oscillations. Jing used several advanced methods (orthogonal polynomial analysis and Strutinski smoothing) to separate the oscillations from the background and identify their uniqueness. Unfortunately, in conclusion he wrote that "the search for evidence for the existence of

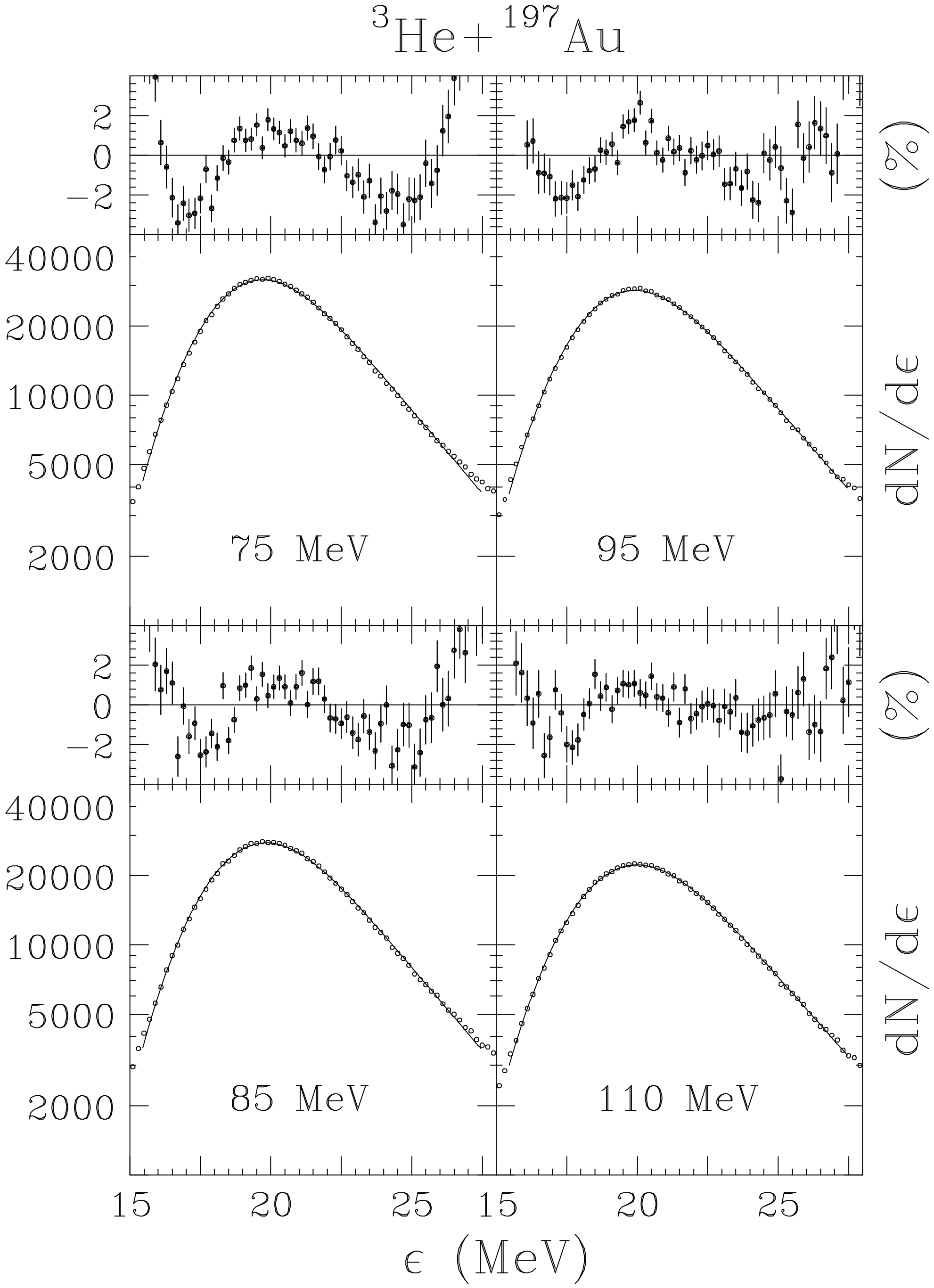

Figure 4.5: Lower panels: The experimentally measured α spectra (∘) from ^{3}He + ^{197}Au reactions at 75, 85, 95, 110 MeV beam energies, and the corresponding fits (—) with Equation 4.9. Upper panels: The percent difference between the experimental data and the fits with Equation 4.9 are shown in the lower panels. The error bars represent the statistical errors of the experimental data.

complex particles as independent particles inside a nucleus is still an ongoing effort … The spectral shape used in the fitting is shown to represent alpha spectra to an excellent precision, although this is not sufficient to convince that the modulations, which appear in the residuals of the fits, are physical … It seems still a long way to reach definite conclusion regarding the physical reality of the observed modulations, thus the existence of complex particles as independent particles inside a nucleus".

Chapter 5

The New Look at the Oscillations: Myth or Reality?

The challenge presented by the duality of the oscillations: their possible origin in the discrepancies between the otherwise smooth functional forms of experimental and theoretical spectra, or in true quantum phenomena, seemed unsurmountable. Nevertheless, the problem remained attractive and promising to yield the evidence of quantum properties surviving thermalization of hot nuclear liquid. Many more weeks went into the analysis of the puzzle until one day an unexpectedly simple and ordinary answer put an end to the lofty expectations.

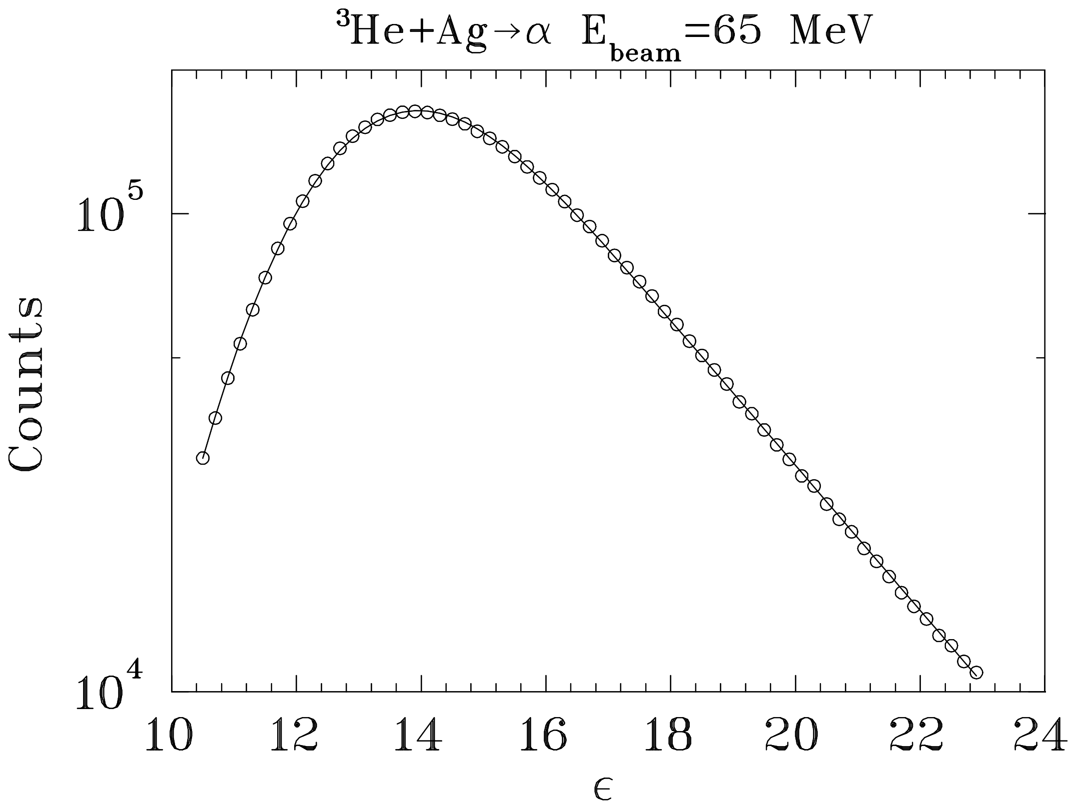

Figure 5.1: The quality of fitting experimental data with Equation 5.1. The circles represent the data, and the solid line is the fit.

5.1 Mundane Solution to an Intriguing Puzzle

The best results for the description of experimental α-spectra are acclaimed by Moretto [More 75, Jing 99], who developed a single-chance emission theory and derived several analytic expressions for the kinetic energy spectrum of a fragment. Although Jing employed a complex version of Moretto's theory (one amplifying mode, one non-amplifying mode and quantum barrier penetration) to fit the spectra and discover the oscillations [Jing 99], the simplest version of the theory, which includes only one amplifying mode, produces very good data fitting results as well, although

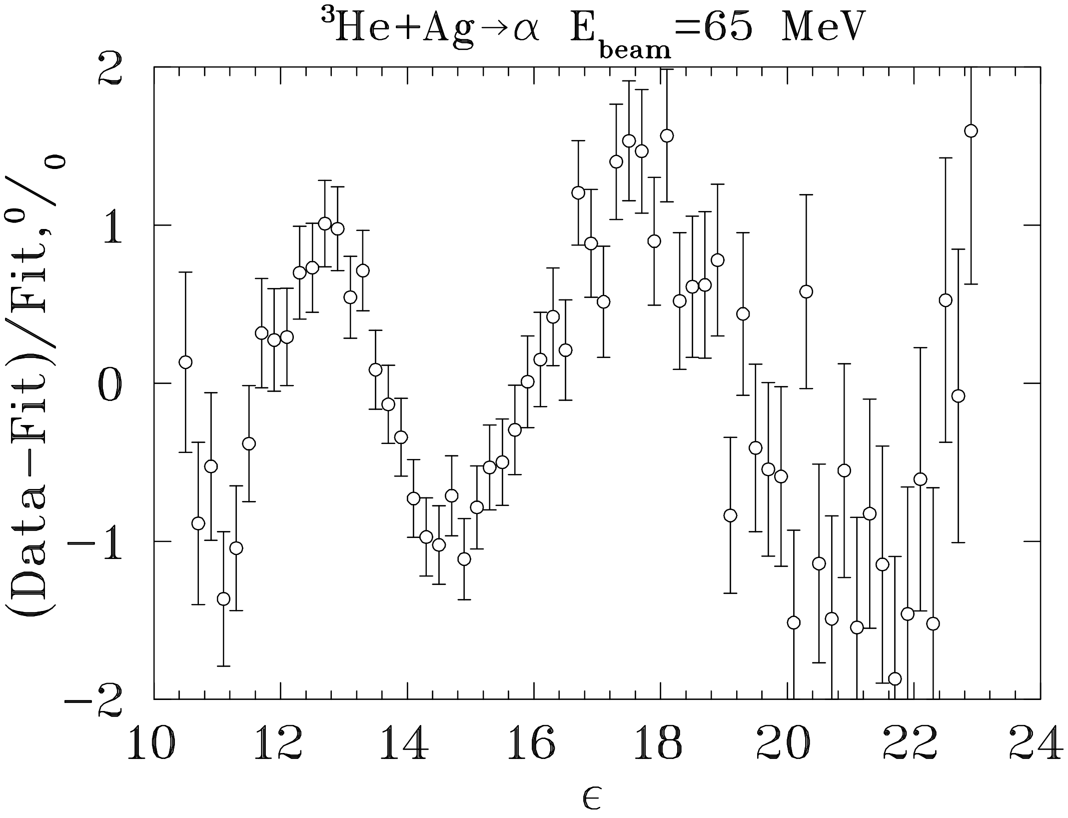

Figure 5.2: An example of oscillations observed in fitting data with Equation 5.1.

at a cost of fewer fitting parameters. According to the theory, the evaporation spectrum can be represented by the simple formula:

$$P(\epsilon) = A \exp\left(-\frac{\epsilon - B}{T}\right) \operatorname{erfc}\left(\frac{p - 2(\epsilon - B)}{2\sqrt{pT}}\right), \tag{5.1}$$

where A is a proportionality constant, ϵ is the kinetic energy of detected fragments, B is the Coulomb barrier at equilibrium deformation, p is the amplification parameter, and T is the temperature of the parent nucleus. The quality of fitting the data by Equation 5.1 is shown in Figure 5.1, which manifests only small deviations. Sure enough, the residuals display the familiar oscillations, analogous to those observed by Jing. Figure 5.2 shows the oscillations. The oscillations are about 1.5% above the background and clearly stand out beyond the statistical noise.

In this thesis, an old and simple explanation will be offered to account for the oscillations in the α-spectra. Being straightforward and unattractive, this approach was hoped to be the last to come true. The pervasive idea of residual quantum effects surviving beyond the thermal emission too much captivated the minds of researchers, as it surely did the author's until an unexpectedly simple trick unlocked the true reality of the puzzle.

Experimental evaporation spectra cannot be expected to be first-chance only. If, for example, α-emission is considered, the α-particle can be emitted from a hot nucleus after the emission of a nucleon. At temperatures when evaporation takes place, emission of a proton or a neutron is the dominant channel of deexcitation, and individual emissions do not remove a large fraction of the excess energy from the nucleus causing multiple-chance α-emission to remain quite probable. As a result, experimental spectra, which are not acquired on the event-by-event basis, but rather consist of all the particles emitted from the target, end up being comprised of α-particles emitted from different parent nuclei.

A very simple calculation can be used to demonstrate this point. Consider the example of the 65 MeV ^{3}He + $^{\mathrm{nat}}$Ag reaction, which produces ^{112}In [1] at the temperature about 2.5 MeV. If the α-particle is emitted second chance after a neutron,

---

[1] Natural silver consists of 51.84 atom % of isotope ^{107}Ag and 48.16 atom % of isotope ^{109}Ag. Production of ^{112}In is considered here only as an example, since ^{110}In is produced in abundance as well.

the probability of such an event relative to the first-chance emission is not far from unity, since neutron emission is by far the most probable process in comparison with the other modes of decay and removes an insignificant part of the nuclear excitation of the order of $2T$. The proton emission is suppressed in comparison to the neutron emission roughly by $p_p \approx \exp(-B_{Coul}/T)$, where B_{Coul} is the proton's Coulomb barrier, and T is the temperature. For ^{112}In B_{Coul} is of order 5 MeV, which gives $p_p \approx$13%. In other words, the second-chance post-proton α-emission is only about 8 times less probable than the post-neutron emission.

The third-chance and higher modes of α-evaporation may already be significantly suppressed due to cooling of the emitting nucleus. However, the multiple-chance emission chains are numerous, and their number increases with the order of the emission mode. For example, the third-chance α-emission can be realized in four ways of nucleon emission sequences preceding the emission of the α-particle, whereas the forth-chance event is nine-fold degenerate.

So far, there has not been a mention of the emission of light charged particles other than protons that can proceed evaporation of α-particles. For example, emission of deuterons and tritons is a probable process competing with the proton emission. These channels of deexcitation, although being less probable than nucleon emission, add to the variety of possible emission modes preceding α-evaporation and enrich the total multiple-chance component in α-spectra.

Almost equal abundance of two isotopes in natural silver can also add to the variety of independent emitters that contribute to the experimental spectrum. Both ^{110}In and ^{112}In α-emitters are first-chance whose properties are not the same.

Overall, the conclusion can be drawn that the kinetic energy α-evaporation spectra may not be considered first-chance single-parent only, but, rather contrary, mixed isotopic content of the target and the presence of the multiple-chance component can have a significant effect on the shape of the spectrum, the multiple-chance component being largely dominated by the second-chance mode. Therefore, since α-particles are emitted from different nuclei, the Coulomb barriers are slightly different for every parent nucleus (due to shrinkage and loss of charge when nucleons and other particles are emitted), and so are the temperatures since the multiple-chance emission occurs from cooled nuclei. The variation in deformation between various parent nuclei is not expected to be large, and for simplicity it will be disregarded in the present analysis. Mathematically, these ideas can be written in the following form:

$$P_{tot}(\epsilon) = \sum_i w_i P_i(B_i, T_i, \epsilon), \tag{5.2}$$

where $P_{tot}(\epsilon)$ is the observed total spectrum of all types of α-particles, i is the counter of emitting parent nuclei, and w_i, B_i, T_i are the weight, Coulomb barrier, and temperature of a particular mode of α-emission. Therefore, no single Coulomb barrier and temperature can be ascribed to an experimental spectrum. Rather these quantities possess a distribution folded into the spectrum according to Equation 5.2.

The aforementioned conclusion did not come as a well thought out result, but was found unexpectedly in the course of data analysis. It was suggested that if

E_b, MeV	B_1, MeV	B_2, MeV	T_1, MeV	T_2, MeV	p, MeV	Rel. Prob., w_2/w_1
55	12.77±0.15	12.36±0.03	2.71±0.04	1.28±0.09	2.49±0.18	0.83±0.32
65	12.74±0.09	12.38±0.02	2.88±0.03	1.31±0.08	2.29±0.12	0.60±0.32
75	12.95±0.15	12.41±0.03	3.06±0.05	1.41±0.09	2.48±0.15	0.94±0.24
95	13.02±0.19	12.44±0.04	3.34±0.09	1.61±0.13	2.37±0.16	0.89±0.31
110	12.92±0.17	12.49±0.05	3.34±0.07	1.48±0.18	2.36±0.20	0.58±0.43
125	13.35±0.18	12.65±0.03	3.57±0.07	1.68±0.08	2.73±0.15	1.27±0.43

Table 5.1: Fitting parameters obtained from the two-spectra decomposition analysis of the α-spectra from the reaction ^{3}He+$^{\mathrm{nat}}$Ag at various beam energies E_b.

the multiple-chance hypothesis were to be right, the observed α-spectra could be presented using Moretto's formula in the following way according to Equation 5.2:

$$P_{tot}(\epsilon) = \sum_i w_i \exp\left(-\frac{\epsilon - B_i}{T_i}\right) \operatorname{erfc}\left(\frac{p - 2(\epsilon - B_i)}{2\sqrt{pT_i}}\right) \tag{5.3}$$

Empirically, at least two average contributions must show up in fitting the data as a superposition of two single-chance spectra, whose weights, temperatures and barriers must differ. The contributions are average since they represent many possible components much in the way like two-point Gaussian quadrature represents an entire integral. Thus, it can be written that

$$\begin{aligned} P(\epsilon) &\approx w_1 \exp\left(-\frac{\epsilon - B_1}{T_1}\right) \operatorname{erfc}\left(\frac{p - 2(\epsilon - B_1)}{2\sqrt{pT_1}}\right) \\ &+ w_2 \exp\left(-\frac{\epsilon - B_2}{T_2}\right) \operatorname{erfc}\left(\frac{p - 2(\epsilon - B_2)}{2\sqrt{pT_2}}\right), \end{aligned} \tag{5.4}$$

where the indexes 1 and 2 refer to the two contributions.

The technique of two-spectra decomposition turned out to be very successful in analysis of experimental data. When fitting the data with the two spectra decomposition method, seven variables have been used as parameters of the fit: w_1, w_2, B_1,

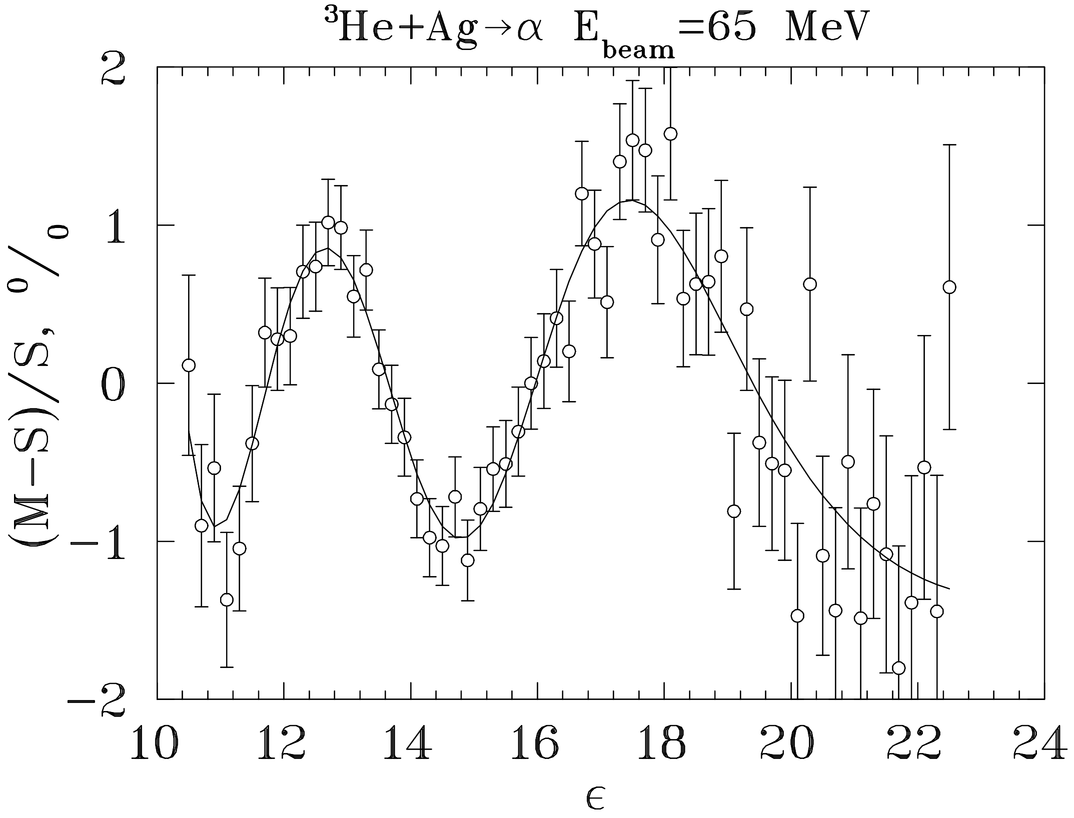

Figure 5.3: Fitting the data with the two spectra decomposition technique is shown to account for the oscillations. The circles represent the relative residuals of the single-chance fit, while the solid line stands for the relative difference between the multiple-chance and single-chance theoretical formulae.

B_2, T_1, T_2, and p. As an example of the fitting, the data set from the experiment at 65 MeV beam energy is shown in Figure 5.3. In the figure, the letter M stands for the multiple-chance spectra both experimental and theoretical (Equation 5.4), while the letter S denotes the single-chance theoretical spectrum of Equation 5.1 according to Moretto. The two spectra decomposition fit yielded the χ^2 per degree of freedom at about 0.96 as compared to about 5.23 when fitting the same spectrum with the first-chance formula in Equation 5.1. More examples of fitting the data at different

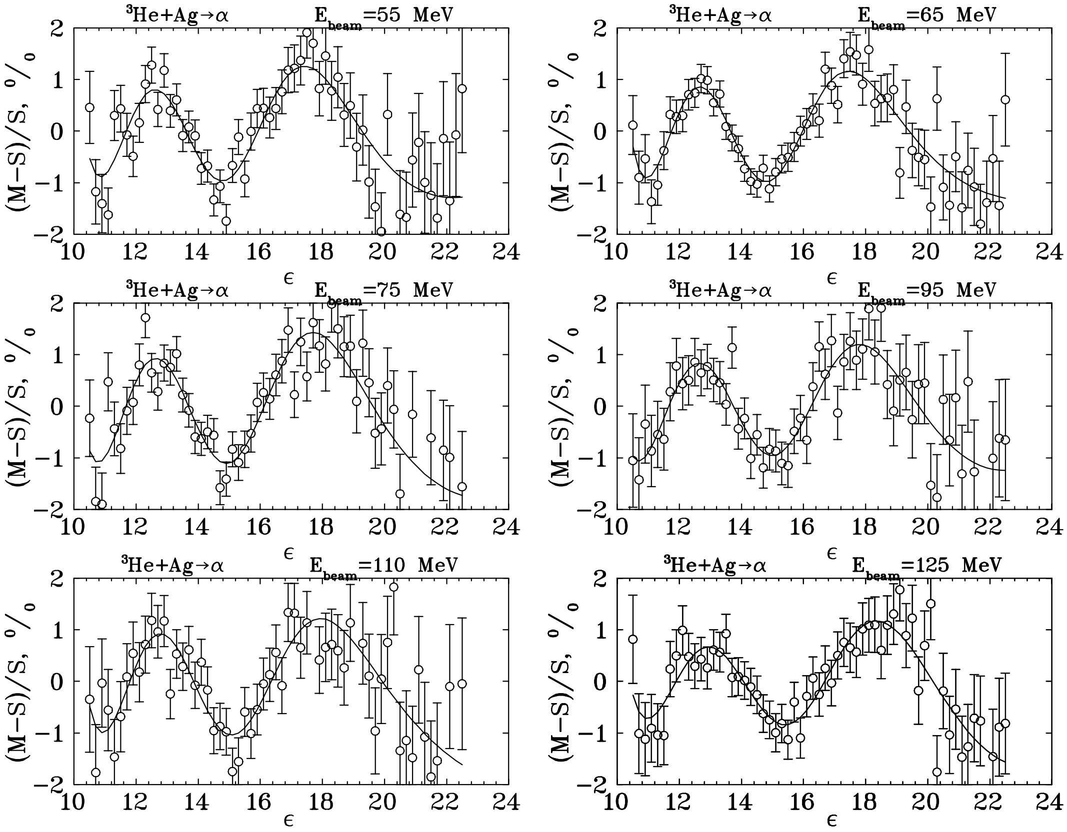

Figure 5.4: Examples of fitting the data with the two spectra decomposition technique at various excitation energies. The oscillations are seen to be completely accounted for. The circles represent the relative residuals of the single-chance fit, while the solid lines stand for the relative difference between the multiple-chance and single-chance theoretical formulae.

beam energies are presented in Figure 5.4. The χ^2-values are all about unity.

The success of the two-spectra decomposition fitting is quite reassuring, and leads to a reasonable preliminary conclusion that the oscillations in the α-emission spectra are created artificially due to fitting the single chance theory to the multiple-chance spectrum. In spite of the visual appeal and simplicity, fitting alone, however, is not sufficient to prove the point. Rigorous model considerations may be necessary to further develop the topic. Nevertheless, analysis of the fitting parameters may strengthen the case.

Table 5.1 offers a list of the fitting parameters extracted from fitting data at different beam energies. Parameters with the subscript 1 can be attributed to the high temperature mostly first-chance spectrum of α-particles, whereas subscript 2 collectively refers to the multiple-chance group dominated by the second-chance emission. Meaningful tendencies can be found in the behavior of the parameters as the excitation energy is increased. First of all, attention should be paid to the temperatures of the spectra, which progressively increase with excitation, as it undoubtedly should be. With the Q-value of the reaction being 14.2 MeV, temperatures T_1 can reasonably well be fitted with a Fermi gas formula for the excitation energy E^*:

$$E^* = \frac{112}{k} T^2 + const \tag{5.5}$$

to obtain the level density coefficient parameter $k \approx 8.5$. An additional constant is used to approximately account for the unknown temperature dependence of the level density parameter.

Temperatures T_2 are generally twice as low in comparison with temperatures T_1, indicating a large loss of energy between the first- and second-chance α-particles. This result is not clear, and may not be physical at all in terms of absolute values. There may be an interplay between the parameters of the fit causing the temperature T_2 to be forced low. At this point no conclusive answer can be presented. However, the very fact that T_2 is lower than T_1 already indicates the right trend.

The Coulomb barriers B_1 of the predominantly first-chance emission display a slight growth with temperature which is possibly caused by increasing the relative abundance of the second-chance component. Since the barriers B_1 are not purely first-chance, the increasing fraction of post-neutron second-chance α-emission may alter these barriers due to decreased radius of ^{111}In in comparison with ^{112}In. In this case the barrier should change in reverse proportion to the radius.

The effect of increasing the second-chance component may also be marginally inferred from the dependence of the amplification parameter p on the temperature. Remembering that p is defined as a ratio of the square of the Coulomb barrier amplitude and the total energy amplitude, the slight growth of this parameter hints at growing the Coulomb barrier amplitude.

A similar increase can be seen for the barriers B_2 evidently caused by the same reason. More important, however, is the difference between B_1 and B_2, which is indicative of the processes preceding the α-emission. It can be seen that the barriers B_2 are consistently lower in comparison with the barriers B_1. If the multiple-chance component in α-spectra were only due to neutron emission, the barriers B_1 and B_2 would compare in the opposite way: the sole neutron emission leads to reducing the size of the emitting nucleus without changing its charge. As it is, however, the smaller barriers B_2 suggest a significant fraction of light charged particles contributing to the multiple-chance nature of α-evaporation.

Not much can be said about the relative contribution w_2/w_1 of the two spectra due to the large uncertainty. The errors are of the order of 50 and more per cent. Nevertheless, with the exception of 125 MeV reaction, the trend is according to the expected pattern of the multiple-chance component being smaller then the first-chance component. As the temperature is increased, the data are also consistent with the anticipated increase of the multiple-chance emission compared to the first-chance.

Altogether, it should be emphasized that the technique of two-spectra decomposition is only meant to demonstrate the possible cause of oscillations qualitatively, and no accurate description of physical parameters should be anticipated. The actual structure of evaporation spectra is expected to be very complex with scores of multiple-chance contributions whose probabilities can vary widely. Nevertheless the simple assumption of the two average spectra does well in doing away with the oscillations and demonstrating the correct trends in extracted physical parameters that together reinforce the belief that the multiple-chance nature of fragment evaporation is indeed the reason for the observed oscillations and not a residual quantum effect.

In order to further confirm the suggested explanation for the oscillations, multiple-chance modification of Moretto's theory needs to be introduced and tested on experimental data. One way to implement this task is through the statistical moment expansion of the spectrum to account for the distribution of temperatures and Coulomb barriers.

5.2 Moment Expansion of Evaporation Spectra

The idea to use the statistical moment expansion of evaporation spectra was recently offered by Moretto in response to the success of the two-spectra decomposition technique [Breu 00]. The moment expansion method can be introduced in the following way. It is always possible to expand the temperature and Coulomb barrier dependent spectrum function $P(\epsilon, B, T)$ in Taylor series about the average values or the zeroth moments $\overline{B}$ and $\overline{T}$ of these quantities. Up to the second order the expansion is

$$\begin{aligned} P(\epsilon, B, T) &= P(\epsilon, \overline{B}, \overline{T}) \\ &+ \left.\frac{\partial P}{\partial B}\right|_{\overline{B},\overline{T}} (B - \overline{B}) + \frac{1}{2}\left.\frac{\partial^2 P}{\partial B^2}\right|_{\overline{B},\overline{T}} (B - \overline{B})^2 \\ &+ \left.\frac{\partial P}{\partial T}\right|_{\overline{B},\overline{T}} (T - \overline{T}) + \frac{1}{2}\left.\frac{\partial^2 P}{\partial T^2}\right|_{\overline{B},\overline{T}} (T - \overline{T})^2 \\ &+ \left.\frac{\partial^2 P}{\partial B \partial T}\right|_{\overline{B},\overline{T}} (B - \overline{B})(T - \overline{T}) + \ldots \end{aligned} \tag{5.6}$$

In integral form, the observed spectrum can be written as

$$\overline{P}(\epsilon) = \int\limits_B \int\limits_T w(B, T) P(\epsilon, B, T) dB dT, \tag{5.7}$$

where $w(B,T)$ is the normalized probability distribution function in coordinates of temperature and the Coulomb barrier. Therefore

$$\overline{P}(\epsilon,B,T) = P(\epsilon,\overline{B},\overline{T}) + \frac{1}{2}\left.\frac{\partial^2 P}{\partial B^2}\right|_{\overline{B},\overline{T}} \sigma_B^2 + \frac{1}{2}\left.\frac{\partial^2 P}{\partial T^2}\right|_{\overline{B},\overline{T}} \sigma_T^2 + \left.\frac{\partial^2 P}{\partial B \partial T}\right|_{\overline{B},\overline{T}} \mathrm{Cov}(B,T) + \ldots \tag{5.8}$$

where

$$\begin{aligned} \sigma_B^2 &= \int\limits_B \int\limits_T w(B,T)(B-\overline{B})^2 dBdT \\ \sigma_T^2 &= \int\limits_B \int\limits_T w(B,T)(T-\overline{T})^2 dBdT \\ \mathrm{Cov}(B,T) &= \int\limits_B \int\limits_T w(B,T)(B-\overline{B})(T-\overline{T}) dBdT \end{aligned} \tag{5.9}$$

are second moments or variances. The first moments in Equation 5.8 are zeros since by assumption they do not survive the averaging operation.

Equation 5.8 elegantly introduces the multiple-chance effects into evaporation spectra as due to a distribution of temperatures and Coulomb barriers. However, the application of Equation 5.8 to data is hindered without using an analytic form for $P(\epsilon,\overline{B},\overline{T})$ and for the second derivatives. The problem can be overcome considering the properties of the expansion. It is easy to see that when there is no distribution of temperatures and barriers, second moments in Equation 5.8 become zero, and all what is left is $P(\epsilon,\overline{B},\overline{T})$. On the other hand, zero second moments mean that evaporation is purely single-chance, which is exactly when Moretto's formula in Equation

5.1 is valid. Therefore, it is an obvious step to assume that

$$P(\epsilon, \overline{B}, \overline{T}) = A \exp\left(-\frac{\epsilon - \overline{B}}{\overline{T}}\right) \operatorname{erfc}\left(\frac{p - 2(\epsilon - \overline{B})}{2\sqrt{p\overline{T}}}\right), \tag{5.10}$$

which is also confirmed by the good quality of fits this formula provides for α-spectra (except for the oscillations).

While $P(\epsilon, \overline{B}, \overline{T})$ describes the average background of the spectra as if it were single-chance, the second derivatives in Equation 5.8 refer to the effects of various multiple-chance components. Formally, they are the derivatives of the unknown functional form of the multiple-chance spectrum. However, to a very good approximation, Moretto's formula in Equation 5.1 can still be used to determine these derivatives, since the functional form it provides is sufficient to describe experimental spectrum up to 1.5% (oscillations). Altogether, the following analytic expression can be derived as an extension of Moretto's theory to include multiple-chance evaporation:

$$\begin{aligned}
\overline{P}(\epsilon, B, T) &= A \exp\left(-\frac{\epsilon - \overline{B}}{\overline{T}}\right) \operatorname{erfc}\left(\frac{p - 2(\epsilon - \overline{B})}{2\sqrt{p\overline{T}}}\right) \\
& \left[1 + \frac{\sigma_B^2}{2\overline{T}^2} + \frac{\sigma_B^2(\epsilon - \overline{B})}{2\overline{T}^3}\left(\frac{\epsilon - \overline{B}}{\overline{T}} - 2\right) + \frac{\operatorname{Cov}(B,T)}{\overline{T}^2}\left(\frac{\epsilon - \overline{B}}{\overline{T}} - 1\right)\right] \\
&+ \frac{A}{\sqrt{\pi}(pT)^{3/2}} \exp\left(-\frac{\epsilon - \overline{B}}{\overline{T}}\right) \exp\left(-\left(\frac{p - 2(\epsilon - \overline{B})}{2\sqrt{p\overline{T}}}\right)^2\right) \\
& \left[-\sigma_B^2(p - 2(\epsilon - \overline{B})) + \frac{\sigma_T^2}{16\overline{T}^2}((p - 2(\epsilon - \overline{B}))^2 - 6p\overline{T})(p - 2(\epsilon - \overline{B}))\right. \\
&+ \left.\frac{p\overline{T} - (\epsilon - \overline{B})p - 2(\epsilon - \overline{B})^2}{T}\operatorname{Cov}(B,T)\right]
\end{aligned} \tag{5.11}$$

Equation 5.11 can be used directly to fit experimental data. It has seven unknown fitting parameters: A, $\overline{B}$, $\overline{T}$, p, σ_B, σ_T, and $\operatorname{Cov}(B,T)$. The results of the fitting are shown in Figure 5.5, in which, as before, M stands for multiple-chance spectra both experimental and theoretical, whereas S is single-chance spectrum according to Moretto's theory. The parameters obtained from the fitting are summarized in Table 5.2. The χ^2's per degree of freedom of the fits are all of order unity.

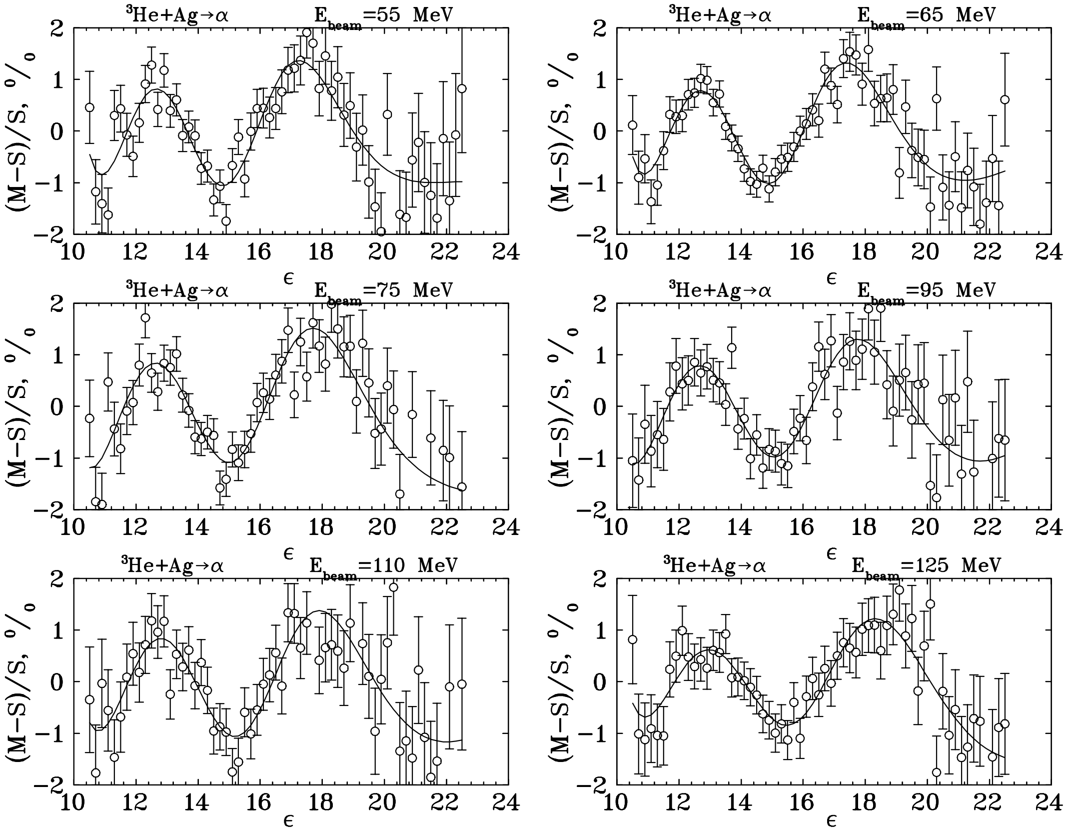

Figure 5.5: Examples of fitting the data with the moment expansion methodology at various excitation energies. The oscillations are completely described. The circles represent the relative residuals of the single-chance fit to the data, while the solid lines stand for the relative difference between the multiple-chance and single-chance fits.

The parameters reveal a steady and consistent change with the excitation energy of the reaction, the errors being small. This change can find a reasonable explanation on the basis of the multiple-chance emission picture. As the excitation energy is

E_b, MeV	$\overline{B}$, MeV	$\overline{T}$, MeV	p, MeV	σ_B, MeV	σ_T, MeV	Cov(B,T), MeV^2
55	12.62±0.02	2.01±0.04	2.28±0.07	0.59±0.07	0.71±0.03	0.15±0.02
65	12.68±0.01	2.16±0.03	2.25±0.06	0.58±0.06	0.75±0.02	0.18±0.01
75	12.71±0.02	2.26±0.04	2.39±0.10	0.46±0.12	0.77±0.03	0.25±0.02
95	12.77±0.02	2.51±0.06	2.25±0.10	0.55±0.10	0.83±0.03	0.27±0.02
110	12.85±0.03	2.52±0.07	2.29±0.11	0.66±0.11	0.89±0.04	0.27±0.03
125	12.94±0.02	2.59±0.05	2.56±0.12	0.46±0.13	0.89±0.02	0.30±0.02

Table 5.2: Fitting parameters obtained from the moment expansion analysis of the α-spectra from the reaction ^{3}He+$^{\mathrm{nat}}$Ag at various beam energies E_b.

increased, the average temperature of the emitting system progressively grows, while the spread of the temperature distribution, tracked by the standard deviation σ_T, also increases. The spread is fairly large in comparison with the absolute value of the average temperature and hints at the significant fraction of low temperature emission. The growth of the spread with the temperature can be explained by the appearance of new modes of emission as the temperature is increased.

The growth of the average temperature $\overline{T}$ causes the growth of the average Coulomb barrier $\overline{B}$, which can reasonably be understood as due to increasing role of the second-chance post-neutron emission. The standard deviation σ_B stays about the same and indicates a significant spread of the barriers of various α-emitting nuclei. The spread does not seem to change appreciably, since the upper limit of the barrier distribution function does not change with temperature, whereas the shape of the distribution may change and affect the average.

In the current analysis, the amplification parameter p is assumed to be a constant, independent on the identity of the emitting nucleus. Although in general it is not true, insignificant variations in mass between various emitters suggest that the amplification parameter should not be expected to change widely. Fitting experimental spectra well confirms this expectation. The oscillations can be accounted for with the assumption of constant p. In addition to that, within the range of errors the data in Table 5.2 indicate a constant value of p with respect to changing temperature. This observation demonstrates that the growing number of possible α-emitters have about the same amplification parameter. On the other hand, a slight growth of p may still be conjectured due to increasing presence of multiple-chance post-neutron emission. Marginally, the data may also be interpreted to support this assumption. Even if it is true, overall the data supports the expectation that the amplification parameter is very narrowly distributed with the mass of α-emitters.

A very important parameter is the covariance $\mathrm{Cov}(B, T)$, which indicates the correlation between the Coulomb barrier and temperature distributions as functions of the mass of the emitting nucleus. As seen from the fitting parameter table, the covariance of these two distributions is positive at every investigated excitation. This fact vividly indicates the decrease of Coulomb barriers with the mass of α-emitters as the temperature goes down depending on the order of the multiple-chance emission event. In other words, as a nucleus cools emitting various light particles, its Coulomb barrier toward α-emission on the average is reduced. This fact is contrary to the expectation of neutron-only pre-α emission and supports the idea of a significant fraction of light charged particles participating in forming pre-α emission chains.

In closing this discussion, it must be emphasized that the extension of Moretto's theory presented here fully accounts for every slightest detail of the observed experimental α-spectra and produces the values of theoretical parameters that can well be explained within the scope of the theory. Although alternative explanations for the oscillations cannot be ruled out completely yet, the experimental evidence is strong in favor of the explanation offered in this thesis.

5.3 Conclusions

The puzzle of kinetic energy oscillations in evaporation α-spectra, which was introduced through the use of single-chance Moretto's theory and long considered as a manifestation of residual quantum effects, has been offered a simple and thorough explanation: the oscillations are the artificial result of fitting a single-chance theory to multiple-chance experimental data. This conclusion was initially reached with the data analysis technique of two spectra decomposition, which assumed the experimental spectrum to consist of at least two independent contributions of α-particles emitted from different parent nuclei. These nuclei can be the result of pre-α emission of particles from the initial compound nucleus, and they can be the result of the isotopic content of the target. The technique successfully accounted for the oscillations in experimental spectra and produced meaningful fitting parameters in compliance with the assumed physical phenomenon. However, the technique had weaknesses and in itself was insufficient to strengthen the newly offered explanation of the oscillations.

Moretto worked out an extension of his single-chance emission theory to allow for multiple-chance properties of the emitting system. Due to a variety of α-emitters contributing to the observed spectrum, the otherwise constant physical parameters like Coulomb barrier and temperature acquire a distribution, whose attributes expressed in statistical moments like variance and covariance, can be added to the formalism by way of statistical moment expansion. Restricting the expansion up to and including the second moments, analytic expressions were obtained to fit experimental spectra. Fitting produced excellent results with the physical parameters exhibiting meaningful values according to the newly offered explanation of the effect.

Unfortunately, no absolute final answer can strictly be given at the time since all the conclusions were based on fitting with many parameters involved. Although experimental evidence is very pressing toward validity of the suggested explanation for the oscillations, no rigorous conclusion can be made without setting a detailed model calculation to accurately account for all the possible modes of α-emission at all temperatures of interest. Then comparisons can be made between the experiment and the calculation, and the aforementioned techniques can act as mediators in the analysis. Unfortunately, this calculation is extremely involved and was not attempted in this thesis.

Bibliography

[Band 39] W. Band, J. Chem. Phys. **7**, 324 (1939); J. Chem. Phys. **7**, 927 (1939).

[Bijl 38] A. Bijl, Doctoral Dissertation, Leiden, presented April 29, 1938

[Bous 96] M. Bousquet-Melou, Discrete Math. **154** (1996) 1-25.

[Brak 90] R. Brak, A. J. Guttmann, J. Phys. A: Math. Gen. **23** (1990) 4581-4588.

[Breu 00] D. Breus *et al.*, LBNL NSD Annual Report (2000).

[Breu 04] D. Breus *et al.*, LBNL NSD Annual Report (2004).

[Brus 67] S. G. Brush, Rev. Mod. Phys. **39**, 883 (1967).

[Elli 02] J. B. Elliott *et al.*, Phys. Rev. Lett. **88**, 042701 (2002).

[Elli 03] J. B. Elliott *et al.*, Phys. Rev. C **67**, 024609 (2003).

[Elli 04] J. B. Elliott *et al.*, LBNL NSD Annual Report (2004).

[Elli 05] J. B. Elliott, L. G. Moretto, L. Phair, Phys. Rev. C **71**, 024607 (2005).

[Fede 88] J. Feder, Fractals, Plenum Press, New York, (1988).

[Fish 59] M. E. Fisher, M. F. Sykes, Phys. Rev. **114**, 45 (1959).

[Fish 67] M. E. Fisher, Physics (N.Y.) **3**, 255 (1967).

[Fish 69] M. E. Fisher, Rep. Prog. Phys. **30**, 615 (1969).

[Flam 03] A. Flammenkamp. On-line Encyclopedia of Integer Sequences.

[Fren 39] J. Frenkel, J. Chem. Phys. **7**, 200 (1939); J. Chem. Phys. **7**, 538 (1939).

[Gill 77] H. P. Gillis *et al.*, J. Chem. Phys. **66**, 214 (1977).

[Gugg 45] E. A. Guggenheim, J. Chem. Phys. **13**, 253 (1945).

[Gugg 93] E. A. Guggenheim, Thermodynamics (North-Holland, Amsterdam, 1993), 4th ed.

[Gutt 00] A. J. Guttmann, I. Jensen, L. H. Wong, I. G. Enting, J. Phys. A: Math. Gen. **33** (2000) 1735-1764.

[Gutt 01] A. J. Guttmann, I. Jensen, A. L. Owczarek, J. Phys. A: Math. Gen. **34** (2001) 3721-3733.

[Helf 61] E. Helfand, H. L. Frisch, J. L. Lebowitz, J. Chem. Phys. **34**, 1037 (1961).

[Huan 87] K. Huang, Statistical Mechanics, John Wiley & Sons, New York, (1987).

[Isin 25] E. Ising, Z. Phys. **31**, 253 (1925).

[Jens 00] I. Jensen, J. Phys. A: Math. Gen. **33** (2000) 3533-3543.

[Jens 03] I. Jensen. Private communications.

[Jing 99] K. X. Jing, Ph.D. thesis, Univ. of California at Berkeley, 1999.

[Kauf 49] B. Kaufman, Phys. Rev. **76**, 1232 (1949).

[Land 00] D. P. Landau, K. Binder, Monte Carlo Simulations in Statistical Physics, Cambridge University Press, Cambridge, (2000).

[LBA 73] J. K. Lee, J. A. Barker, F. F. Abraham, J. Chem. Phys. **58**, 3166 (1973).

[Lebo 65] J. L. Lebowitz, E. Helfand, E. Praestgaard, J. Chem. Phys. **43**, 774 (1965).

[Lin 91] K. Y. Lin, J. Phys. A: Math. Gen. **24** (1991) 2411-2417.

[Mand 82] B. B. Mandelbrot, The Fractal Geometry of Nature, W. H. Freeman, New York, (1982).

[Maye 40] J. E. Mayer, M. G. Mayer, Statistical Mechanics, John Wiley & Sons, New York (1940), chaps. 13 and 14.

[More 75] L. G. Moretto, Nucl. Phys. **A247**, (1975) 211.

[More 87] L. G. Moretto and D. R. Bowman, Lawrence Berkeley Laboratory, Report LBL-23228 (1987).

[More 97] L. G. Moretto, R. Ghetti, L. Phair, K. Tso, G. J. Wozniak, Phys. Rep. **287** (1997) 249-336.

[More 97b] L. G. Moretto, K. X. Jing, L. Phair, G. J. Wozniak, J. Phys. G: Nucl. Part. Phys. **23**, 1323 (1997).

[More 02] L. G. Moretto, J. B. Elliott, L. Phair, G. J. Wozniak, Phys. Rev. C **65** 024316 (2002).

[More 03] L. G. Moretto, J. B. Elliott, L. Phair, Phys. Rev. C **68** 061602(R) (2003).

[More 04] L. G. Moretto, J. B. Elliott, L. Phair, in progress, LBNL-51306.

[More 05] L. G. Moretto *et al.*, submitted to Phys. Rev. Lett., LBNL-54448.

[Newe 53] G. F. Newell, E. W. Montroll, Rev. Mod. Phys. **25**, 353 (1953).

[Onsa 44] L. Onsager, Phys. Rev. **65**, 117 (1944).

[Path 86] R. K. Pathria, Statistical Mechanics, Pergamon Press, Oxford, (1986).

[Reis 68] H. Reiss, J. L. Katz, E. R. Cohen, J. Chem. Phys. **48**, 5553 (1968).

[Reis 70] H. Reiss, J. Stat. Phys. **2**, 83 (1970).

[RFL 59] H. Reiss, H. L. Frisch, J. L. Lebowitz, J. Chem. Phys. **31**, 369 (1959).

[RFHL 60] H. Reiss, H. L. Frisch, E. Helfand, J. L. Lebowitz, J. Chem. Phys. **32**, 119 (1960).

[Rush 59] G. S. Rushbrooke, J. Eve, J. Chem. Phys. **31**, 1333 (1959).

[Sato 03] N. Sator, Phys. Rep. **376** (2003) 1-39.

[Schr 91] M. R. Schroeder, Fractals, Chaos, Power Laws: Minutes from an Infinite Paradise, W. H. Freeman, (1991).

[Stau 75] D. Staufer, J. Phys. C: Solid State Phys. **8**, (1975) L 172.

[Stau 79] D. Staufer, Phys. Rep. **54** (1979) 1-74.

[Stil 63] F. H. Stillinger, J. Chem. Phys. **38**, 1486 (1963).

[Stil 67] F. H. Stillinger, J. Chem. Phys. **47**, 2513 (1967).

[Swam 78] P. K. Swaminathan, D. Poland, J. Chem. Phys. **69**, 3660 (1978).

[Tolm 38] R. C. Tolman, The Principles of Statistical Mechanics, Oxford Un. Press, London (1938), Sec. 141.

[Yang 52] C. N. Yang, Phys. Rev. **85**, 808 (1952).

[YLee 52] C. N. Yang, T. D. Lee, Phys. Rev. **87**, 404 (1952).

Appendix A

Analysis Codes

To realize the calculations described in Chapters 2 and 3, the following Matlab codes were involved. Section A.1, presents a simple program to calculate the lattice gas pressure with SAP combinatorics according to the methodology of Chapter 2. Section A.2 details the application of the modified Fisher's model to geometric clusters in order to obtain the lattice gas pressure and find characteristic signatures of cluster interaction.

A.1 The Lattice Gas Pressure from SAP

```
%%%%%%%%%%%%%%%%%%%%%%%%%%%%%%%%%%%%%%%%%%%%%%%%%%%
%%%%%%%%%%%% Load Initial Data %%%%%%%%%%%%%%%%%%%%
%%%%%%%%%%%%%%%%%%%%%%%%%%%%%%%%%%%%%%%%%%%%%%%%%%%

clear;
% SAP distributions by size and area.
load SAP.dat
% Onsager's pressure vs. temperature for comparison.
```

```
load PTO.dat
% Onsager's heat capacity vs. temperature for comparison.
load CVO.dat

% Onsager's pressure and temperature in separate vectors.
T=PTO(:,1); P=PTO(:,2);
% Heat capacity and temperature in separate vectors.
TCV=CVO(:,1); CV=CVO(:,2);
% SAP size, surface and number in separate vectors
A=SAP(1:877,1); S=SAP(1:877,2); g=SAP(1:877,3);

%%%%%%%%%%%%%%%%%%%%%%%%%%%%%%%%%%%%%%%%%%%%%%%%%%%
%%%%%%%%%%%% Solve Differential Equation %%%%%%%%%%
%%%%%%%%%%%%%%%%%%%%%%%%%%%%%%%%%%%%%%%%%%%%%%%%%%%

% Set ODE options
options = odeset('RelTol',1e-8,'AbsTol',1e-8);
% Solve the differential equation f (see below) to obtain an
% approximation to the lattice gas pressure PSOL vs. temperature
% TSOL.
[TSOL,PSOL]=ode45(@f,[1e-50 3],0,options,A,P,g);

%%%%%%%%%%%%%%%%%%%%%%%%%%%%%%%%%%%%%%%%%%%%%%%%%%%
%%%%%%%%%%%% Additional Calculations %%%%%%%%%%%%%%
%%%%%%%%%%%%%%%%%%%%%%%%%%%%%%%%%%%%%%%%%%%%%%%%%%%

% Calculate an approximation to the lattice gas heat capacity CVSOL.
CVSOL = cv(TSOL,PSOL,A,P,g);
% Find the critical temperature TC and pressure PC.
minoptions = optimset('TolX',1e-10);
TC = fminbnd(@cvfunc,2,3,minoptions,TSOL,PSOL,A,P,g);
PC = interp1(TSOL,PSOL,TC,'spline');

%%%%%%%%%%%%%%%%%%%%%%%%%%%%%%%%%%%%%%%%%%%%%%%%%%%
%%%%%%%%%%%% Plotting %%%%%%%%%%%%%%%%%%%%%%%%%%%%%%
%%%%%%%%%%%%%%%%%%%%%%%%%%%%%%%%%%%%%%%%%%%%%%%%%%%

% Interpolating TSOL and PSOL to match vectors T and P.
PSOL=interp1(TSOL,PSOL,T,'spline');
% Plotting.
plot(TSOL,PSOL,'*',T,P,'-');
```

```
%%%%%%%%%%%%%%%%%%%%%%%%%%%%%%%%%%%%%%%%%%%%%%%%%%%
%%%%%%%%%%%% Functions %%%%%%%%%%%%%%%%%%%%%%%%%%%%
%%%%%%%%%%%%%%%%%%%%%%%%%%%%%%%%%%%%%%%%%%%%%%%%%%%

% Differential equation
function dydt = f(t,y,A,P,g)
c = 2;
sp = c.*sum(P.*g.*exp(-c.*P./t-(A+P).*y./t));
sa = sum(A.*g.*exp(-c.*P./t-(A+P).*y./t));
dydt = (sp./(1+sa)+y)./t;

% Heat capacity
function CV = cvfunc(t,tv,yv,A,P,g)

y = interp1(tv,yv,t,'spline');
c = 2;
sp  = sum(P   .*g.*exp(-c.*P./t-(A+P).*y./t));
sa  = sum(A   .*g.*exp(-c.*P./t-(A+P).*y./t));
sp2 = sum(P.^2.*g.*exp(-c.*P./t-(A+P).*y./t));
sa2 = sum(A.^2.*g.*exp(-c.*P./t-(A+P).*y./t));
sap = sum(A.*P.*g.*exp(-c.*P./t-(A+P).*y./t));
sa = 1+sa;
hc  = -c^2/t^2*(sp2/sa-sp*sp2/sa^2-2*sp*sap/sa^2
                +sp^2*sa2/sa^3+sp^2*sap/sa^3);

% Heat capacity as an array.
function CV = cv(t,y,A,P,g)

c = 2;
for j = [1:length(t)]
  sp  = sum(P   .*g.*exp(-c.*P./t(j)-(A+P).*y(j)./t(j)));
  sa  = sum(A   .*g.*exp(-c.*P./t(j)-(A+P).*y(j)./t(j)));
  sp2 = sum(P.^2.*g.*exp(-c.*P./t(j)-(A+P).*y(j)./t(j)));
  sa2 = sum(A.^2.*g.*exp(-c.*P./t(j)-(A+P).*y(j)./t(j)));
  sap = sum(A.*P.*g.*exp(-c.*P./t(j)-(A+P).*y(j)./t(j)));
  sa = 1+sa;
  hc(j)  = c^2/t(j)^2*(sp2/sa-sp*sp2/sa^2-2*sp*sap/sa^2+
                       sp^2*sa2/sa^3+sp^2*sap/sa^3);
end
```

A.2 Modified Fisher's Code

```
%************************************
%****** Data input ******************
%************************************

clear;

% Declaration of global arrays.
global data;
global errors;
global PTO;

% Load data and error arrays. These are two-dimensional
% arrays with geometric cluster concentrations and statistical
% errors to the concentrations vs. temperature and cluster size.
load data;
load errors;
% Load Onsager's pressure and heat capacity vs. temperature.
load PTO.dat
load CVO.dat
% Rearrange Onsager's data into vectors.
T   = PTO(:,1); P   = PTO(:,2);
TCV = CVO(:,1); CV  = CVO(:,2);
% Set the range of cluster sums.
A=[1:1000];
% Set the cluster size fitting range.
Afit=[10:25]';

%******************************************
%*** Original Fisher's Model Minimization **
%******************************************

% Initial values of Fisher's parameters.
q_0 = 0.032;
l   = 0.1;
x   = 3;
k   = 3;
sig = 1/2;
c_0 = 8;

parmf0(1) = q_0;
```

```
parmf0(2) = l;
parmf0(3) = x;
parmf0(4) = k;
parmf0(5) = c_0;

% Fitting
fitoptions = optimset('TolFun',1e-6,'TolX',1e-6,'MaxIter',
               100000, 'MaxFunEvals',100000,'LargeScale','off');
[parmf,chisqf,exitflag,output,grad,hessian] = fminunc(@ffit0,
                                          parmf0,fitoptions,Afit,T);

parmf = abs(parmf);

q_0 = parmf(1);
l   = parmf(2);
x   = parmf(3);
k   = parmf(4);
c_0 = parmf(5);

% Calculating the lattice gas pressure with the original
% Fisher's model POF.
for j = [1:length(T)]
  POF(j) = T(j)*sum(nf(A,T(j),q_0,l,x,k,sig,c_0));
end

%******************************************
%******* Parameter errors *****************
%******************************************

dparmf=sqrt(diag(inv(hessian)));
fitparsf=[parmf',dparmf];

%**********************************************
%******** Modified Fisher's Model Minimization *
%**********************************************

% Initial parameter values
q_0 = 0.032;
l   = 0.1;
x   = 3.6;
k   = 3.7;
c_0 = 7.3377;
```

```
parm0(1) = q_0;
parm0(2) = l;
parm0(3) = x;
parm0(4) = k;
parm0(5) = c_0;

% Fitting
odeoptions = odeset('RelTol',1e-9,'AbsTol',1e-9);
fitoptions = optimset('TolFun',5e-1,'TolX',5e-1,'MaxIter',
                100000,'MaxFunEvals',100000,'LargeScale','off');
parm = fminsearch(@ffit,parm0,fitoptions,odeoptions,T,A,Afit);
fitoptions = optimset('TolFun',1e-6,'TolX',1e-6,'MaxIter',100000,
                      'MaxFunEvals',100000,'LargeScale','off');
[parm,chisq,exitflag,output,grad,hessian] = fminunc(@ffit,parm,
                                fitoptions,odeoptions,T,A,Afit);

q_0 = parm(1);
l   = parm(2);
x   = parm(3);
k   = parm(4);
c_0 = parm(5);
sig = l / 2;
kap = c_0 / 2;

%******************************************
%******* Parameter errors *****************
%******************************************

dparm=sqrt(diag(inv(hessian)));
fitpars=[parm',dparm];

%****************************************
%********* Thermodynamics ***************
%****************************************

% An approximation to the lattice gas pressure as a
% solution to the differential equation fdiff with the
% best set of Fisher's parameters.
[TSOL,PSOL] = ode113(@fdiff,[1e-10 3],0,odeoptions,A,
                     q_0,c_0,x,sig,k,kap,l);
% Heat capacity.
```

```
CVSOL       = cv (A,TSOL,PSOL,q_0,c_0,x,sig,k,kap,l)';

%*****************************************
%********* Density ***********************
%*****************************************

RSOL     = rho (A,TSOL,PSOL,q_0,c_0,x,sig,k,kap,l)';

%*****************************************
%********* Sample Cluster Distributions **
%*****************************************

n10d = data(10,1:length(T));
n15d = data(15,1:length(T));
n20d = data(20,1:length(T));
n25d = data(25,1:length(T));

e10d = errors(10,1:length(T));
e15d = errors(15,1:length(T));
e20d = errors(20,1:length(T));
e25d = errors(25,1:length(T));

n10  = n(10,tv,pv,rv,q_0,c_0,x,sig,k,kap,l);
n15  = n(15,tv,pv,rv,q_0,c_0,x,sig,k,kap,l);
n20  = n(20,tv,pv,rv,q_0,c_0,x,sig,k,kap,l);
n25  = n(25,tv,pv,rv,q_0,c_0,x,sig,k,kap,l);

%*****************************************
%********* Critical Point ****************
%*****************************************

minoptions=optimset('TolX',1e-9);
TC     = fminbnd(@cvfunc,2.1,2.4,minoptions,TSOL,PSOL,
                 A,q_0,c_0,x,sig,k,kap,l);
PC     = interp1(TSOL,PSOL,TC,'spline');

%*****************************************
%********* Critical Point Error **********
%*****************************************

f1     = fminbnd(@cvfunc,2,3,minoptions,t,p,A,q_0+
                 0.0001*q_0,c_0,x,sig,k,kap,l);
```

```
f2     = fminbnd(@cvfunc,2,3,minoptions,t,p,A,q_0-
                 0.0001*q_0,c_0,x,sig,k,kap,l);
dtcdq0 = (f1-f2) / 0.0002 / q_0;
f1     = fminbnd(@cvfunc,2,3,minoptions,t,p,A,q_0,
                 c_0,x,sig,k,kap,l+0.0001*l);
f2     = fminbnd(@cvfunc,2,3,minoptions,t,p,A,q_0,
                 c_0,x,sig,k,kap,l-0.0001*l);
dtcdl  = (f1-f2) / 0.0002 / l;
f1     = fminbnd(@cvfunc,2,3,minoptions,t,p,A,q_0,
                 c_0,x+0.0001*x,sig,k,kap,l);
f2     = fminbnd(@cvfunc,2,3,minoptions,t,p,A,q_0,
                 c_0,x-0.0001*x,sig,k,kap,l);
dtcdx  = (f1-f2) / 0.0002 / x;
f1     = fminbnd(@cvfunc,2,3,minoptions,t,p,A,q_0,
                 c_0,x,sig,k+0.0001*k,kap,l);
f2     = fminbnd(@cvfunc,2,3,minoptions,t,p,A,q_0,
                 c_0,x,sig,k-0.0001*k,kap,l);
dtcdk  = (f1-f2) / 0.0002 / k;
f1     = fminbnd(@cvfunc,2,3,minoptions,t,p,A,q_0,
                 c_0+0.0001*c_0,x,sig,k,kap,l);
f2     = fminbnd(@cvfunc,2,3,minoptions,t,p,A,q_0,
                 c_0-0.0001*c_0,x,sig,k,kap,l);
dtcdc0 = (f1-f2) / 0.0002 / c_0;
DTC    = sqrt(dtcdq0^2*dparm(1)^2+dtcdl^2*dparm(2)^2+
              dtcdx^2*dparm(3)^2+dtcdk^2*dparm(4)^2+
      dtcdc0^2*dparm(5)^2);

%******************************************
%****** Plotting ************************
%******************************************

plot(TSOL,PSOL,TSOL,POF,'*',T,P,'-');

%******************************************
%****** Functions ***********************
%******************************************

% Heat capacity as an array.
function CV = cv(A,t,p,q_0,c_0,x,sig,k,kap,l)

c = c_0 / kap;
Asig = A.^sig + l.*A;
```

```
for j = [1:length(t)]
  sp  = kap   *sum(Asig   .*np(A,t(j),p(j),q_0,c_0,x,sig,k,kap,l));
  sp2 = kap^2.*sum(Asig.^2.*np(A,t(j),p(j),q_0,c_0,x,sig,k,kap,l));
  sa2 =        sum(A.^2   .*np(A,t(j),p(j),q_0,c_0,x,sig,k,kap,l));
  sap = kap   *sum(A.*Asig.*np(A,t(j),p(j),q_0,c_0,x,sig,k,kap,l));
  sa  =        sum(A      .*np(A,t(j),p(j),q_0,c_0,x,sig,k,kap,l));
  u   = c*sp/(1+sa);
  hc(j)  = (c.^2.*sp2-c.*u.*(sp2+2.*sap)+
            u.^2.*(sa2+sap))./t(j).^2./(1+sa);
end

% Heat capacity
function CV = cvfunc(t,tv,pv,A,q_0,c_0,x,sig,k,kap,l)

c    = c_0 / kap;
p    = interp1(tv,pv,t,'spline');
Asig = A.^sig + l.*A;
sp   = kap*  sum(Asig   .*np(A,t,p,q_0,c_0,x,sig,k,kap,l));
sp2  = kap^2*sum(Asig.^2.*np(A,t,p,q_0,c_0,x,sig,k,kap,l));
sa2  =       sum(A.^2   .*np(A,t,p,q_0,c_0,x,sig,k,kap,l));
sap  = kap*  sum(A.*Asig.*np(A,t,p,q_0,c_0,x,sig,k,kap,l));
sa   =       sum(A      .*np(A,t,p,q_0,c_0,x,sig,k,kap,l));
u    = c*sp/(1+sa);
hc   = -(c^2*sp2-c*u*(sp2+2*sap)+u^2*(sa2+sap))/t^2/(1+sa);

% Differential equation
function dydt = fdiff(t,y,A,q_0,c_0,x,sig,k,kap,l)

Asig = A.^sig + l.*A;
s1 = c_0.*sum(Asig.*np(A,t,y,q_0,c_0,x,sig,k,kap,l));
s2 =      sum(A   .*np(A,t,y,q_0,c_0,x,sig,k,kap,l));
dydt = (s1./(1+s2)+y)./t;

% Fitting function for the modified Fisher's model.
function [chisq,t,p]=ffit(parm,odeoptions,tv,A,Afit);

global data;
global errors;
global att;

parm = abs(parm);
```

```
q_0 = parm(1);
l   = parm(2);
x   = parm(3);
k   = parm(4);
c_0 = parm(5);
kap = c_0 / 2;
sig = 1 / 2;

[t,p]=ode113(@fdiff,[1e-30 3],0,odeoptions,A,q_0,
             c_0,x,sig,k,kap,l);
pv    = interp1(t,p,tv,'spline');
rv    = rho(A,tv,pv,q_0,c_0,x,sig,k,kap,l);

chisq=0;
for j=[1:length(tv)]
  nc = n(Afit,tv(j),pv(j),rv(j),q_0,c_0,x,sig,k,kap,l);
  ss = sum((data(Afit,j)-nc).^2./errors(Afit,j).^2);
  chisq = chisq + ss;
end

chisq = chisq / (length(Afit)*length(tv)-length(parm));

disp([parm,chisq])

% Fitting function for the original Fisher's model.
function chisq = ffit0(parm,Afit,tv);

global data;
global errors;

parm = abs(parm);

q_0 = parm(1);
l   = parm(2);
x   = parm(3);
k   = parm(4);
c_0 = parm(5);
sig = 1/2;


chisq=0;
```

```
for j=[1:length(tv)]
  ss = sum((data(Afit,j)-nf(Afit,tv(j),q_0,
           l,x,k,sig,c_0)).^2./errors(Afit,j).^2);
  chisq = chisq + ss;
end

chisq=(chisq)/(length(Afit)*length(tv)-length(parm));

disp([parm,chisq])

% Modified Fisher's cluster concentration
function conc = n(a,t,p,r,q_0,c_0,x,sig,k,kap,l);

conc = np(a,t,p,q_0,c_0,x,sig,k,kap,l).*(1-r);

% Modified Fisher's pressure-only dependent
% cluster concentration
function conc = np(a,t,p,q_0,c_0,x,sig,k,kap,l);

asig = a.^sig + l.*a;
conc = q_0.*asig.^(-x).*exp(k.*asig -
                  (c_0.*asig + (a+kap.*asig).*p)./t);

% Original Fisher's cluster concentration
function conc = nf(a,t,q_0,l,x,k,sig,c_0);

asig = a.^sig + l.*a;
conc = q_0.*asig.^(-x).*exp(k.*asig - c_0.*asig./t);

% Density.
function r = rho(A,t,p,q_0,c_0,x,sig,k,kap,l)

for j=[1:length(t)]
  s = sum(A.*np(A,t(j),p(j),q_0,c_0,x,sig,k,kap,l));
  r(j) = s./(1 + s);
end
```